INVESTIGATION OF THE EFFECT OF INTRA-MOLECULAR INTERACTIONS ON THE GAS-PHASE CONFORMATION OF PEPTIDES AS PROBED BY ION MOBILITY-MASS SPECTROMETRY, GAS-PHASE HYDROGEN/DEUTERIUM EXCHANGE, AND MOLECULAR MECHANICS

A Dissertation

by

HOLLY ANN SAWYER

Submitted to the Office of Graduate Studies of
Texas A&M University
in partial fulfillment of the requirements for the degree of

DOCTOR OF PHILOSOPHY

December 2004

Major Subject: Chemistry

INVESTIGATION OF THE EFFECT OF INTRA-MOLECULAR INTERACTIONS ON THE GAS-PHASE CONFORMATION OF PEPTIDES AS PROBED BY ION MOBILITY-MASS SPECTROMETRY, GAS-PHASE HYDROGEN/DEUTERIUM EXCHANGE, AND MOLECULAR MECHANICS

A Dissertation

by

HOLLY ANN SAWYER

Submitted to Texas A&M University
in partial fulfillment of the requirements
for the degree of

DOCTOR OF PHILOSOPHY

Approved as to style and content by:

David H. Russell (Chair of Committee)	Simon W. North (Member)
Gyula Vigh (Member)	David P. Giedroc (Member)
Emile A. Schweikert (Head of Department)	

December 2004

Major Subject: Chemistry

ABSTRACT

Investigation of the Effect of Intra-molecular Interactions on the Gas-Phase Conformation of Peptides as Probed by Ion Mobility-Mass Spectrometry, Gas-Phase Hydrogen/Deuterium Exchange, and Molecular Mechanics. (December 2004)

Holly Ann Sawyer, B.S., Harding University

Chair of Advisory Committee: Dr. David H. Russell

Ion mobility-mass spectrometry (IM-MS), gas-phase hydrogen/deuterium (H/D) exchange ion molecule reactions and molecular modeling provide complimentary information and are used here for the characterization of peptide ion structure, including fine structure detail (*i.e.*, cation-π interactions, β-turns, and charge solvation interactions). IM-MS experiments performed on tyrosine containing tripeptides show that the collision cross-sections of sodiated, potassiated and doubly sodiated species of gly-gly-tyr are smaller than that of the protonated species, while the cesiated and doubly cesiated species are larger. Conversely, all of the alkali-adducted species of try-gly-gly have collision cross-sections that are larger than that of the protonated species. The protonated and alkali metal ion adducted (Na^+, K^+ and Cs^+) species of bradykinin and bradykinin fragments 1-5, 1-6, 1-7, 1-8, 2-7, 5-9 and 2-9 were also studied using IM-MS and the alkali metal ion adducts of these species were found to have cross-sections very close to those of the protonated species. Additionally, multiple peak features observed in the ATDs of protonated bradykinin fragments 1-5, 1-6 and 1-7 are conserved upon

alkali metal ion adduction. It was observed from gas-phase H/D ion molecule reactions that alkali adducted species exchange slower and to a lesser extent than protonated species in the tyrosine- and arginine-containing peptides. Experimental and computational results are discussed in terms of peptide ion structure, specifically the intra-molecular interactions present how those interactions change upon alkali salt adduction, as well as with the sequence of the peptide.

Additionally, IM-MS data suggests the presence of a compact conformation of bradykinin fragment 1-5 (RPPGF) when starting from organic solvent conditions. As water is added stepwise to methanolic solutions, a more extended conformation is populated. When the starting solution is composed of ≈90% water, two distinct mobility profiles are observed as well as a shoulder, indicating the presence of three gas-phase conformations for RPPGF. Gas-phase H/D exchange of $[M+H]^+$ ions prepared from aqueous solvents show a bi-exponential decay, whereas samples prepared from organic solvents show a single exponential decay. The effect of solvent on gas-phase peptide ion structure, *i.e.*, solution-phase memory effects, is discussed and gas-phase structures are compared to know solution-phase structures.

DEDICATION

This dissertation is dedicated to my parents, C.W. Sawyer and Janet M. Sawyer, and my sister, Sonya M. Sawyer for their love and support during my graduate career.

ACKNOWLEDGMENTS

I would like to thank my advisor, Dr. David H. Russell, for the opportunity to pursue research under his guidance. I would also like to thank all the current and former Russell group members who were sources of guidance and support. I would especially like to thank Joe Marini for his guidance during the development of the H/D exchange experiments and Dr. Earle Stone for performing the IM-SID-MS experiments on the bradykinin fragment 1-5 system. I am grateful to Brandon Ruotolo, Dr. Kent Gillig, and Dr. John McLean for their helpful conversations. Additionally, I would like to thank Jessica Lucas for her great listening ability and friendship.

I would like to acknowledge Dr. Lisa M. Pérez, manager of the Laboratory for Molecular Simulations, for her immense knowledge and never-ending guidance, help and support during the development and implementation of the processes described in Chapter III, the generation and proposal of structures through molecular mechanics.

On a personal note, I would like to thank my family and friends for providing much-needed support during my graduate career. Special thanks go out to my parents, C.W. and Janet Sawyer, my sister, Sonya Sawyer, and close friends April Palmer and Stacy Means. I especially would like to thank Shannon Burns for her friendship and for our lunch dates that helped to keep me sane and on-track.

TABLE OF CONTENTS

CHAPTER Page

LIST OF FIGURES

FIGURE Page

FIGURE Page

FIGURE Page

FIGURE Page

FIGURE Page

FIGURE Page

FIGURE Page

LIST OF TABLES

CHAPTER I

INTRODUCTION

With the sequencing of the human genome and the ever-increasing library of genomes becoming available, the prospects for drug discovery and advancement in disease diagnosis and treatment are becoming vast. However, an accurate and complete sequence of a genome cannot precisely convey or predict what proteins are expressed, where they are located or how much of each protein is expressed.[1] Neither can a genomic sequence contain information regarding post-translational modifications, protein interactions or protein structure.[2] Direct characterization of proteins is needed in order to fully understand the structure, thereby giving insight into protein-protein interactions, expression, and function.

Most near native protein structure studies are conducted in the solution phase using techniques such as Nuclear Magnetic Resonance (NMR) and Circular Dichroism (CD) or in the solid-phase using X-ray Crystallography. While considerable improvement in these methodologies has been made, a compromise between resolution and throughput still exits. For example, while both NMR and X-ray Crystallography offer atomic resolution on secondary, tertiary and quaternary protein structure, considerable amounts of time are required for analysis. CD analysis requires approximately 2 hours but information is limited to the general secondary structure of the protein (*i.e.*, α-helices, β-sheet, and β-turns). Gas-phase structural studies involving mass spectrometry-based techniques may offer a high-throughput alternative to the pre-

---

This dissertation follows the style and format of *Analytical Chemistry*.

existing protein structure characterization methodologies.

With the development of matrix-assisted laser desorption ionization (MALDI) and electrospray ionization (ESI), the use of mass spectrometry (MS) to study biological molecules, such as peptides and proteins, was greatly increased. Great headway has been made in the use of mass spectrometry to elucidate the primary structure of proteins.[3] Secondary and tertiary structure have been studied by MS, through the use of hydrogen/deuterium exchange[4], post-source decay[5], as well as dissociation kinetics[6] and fragmentation processes such as surface-induced dissociation (SID)[7], collision-induced dissociation (CID)[8], and metastable ion dissociation[9]. Additionally, MS is becoming increasingly important in the characterization of post-translational modifications[10, 11] and protein-protein interactions.[12, 13] Emerging techniques, such as ion mobility-mass spectrometry (IM-MS), are making the analysis of three-dimensional protein and peptide structure by gas-phase techniques available.

While mass spectrometry is a high throughput technology, an intrinsic drawback to the use of this technique to protein structure characterization is that all measurements are made in the gas phase. The relevance of gas-phase peptide and protein ion structure to that of solution-phase structures has yet to be fully realized. While some experiments have shown that there may be some memory of the solution-phase structure in the gas phase for select protein/peptide systems[14-16], it is still questionable whether gas-phase structure is indicative of near native structure for the vast majority of protein systems. Regardless of the relevance of gas-phase structure to solution-phase structure, studies of gas-phase structure are integral to understanding the effect of intrinsic properties of

peptide ions in the absence of solvent (*i.e.*, intra-molecular interactions and charge solvation).

The functional secondary/tertiary structure of proteins/peptides depends on a delicate balance of multiple forces. Paramount among the forces that dictate the structure of all functional bio-molecules are those imparted by the solvent. While the interaction of solvent with proteins is known to dramatically influence the stability of native conformation, it is often difficult to determine the precise effect of solvent on protein structure. Comparisons of gas-phase structure to solution-phase structure may aid in clarification of the effect of solvent on the structure. Furthermore, experiments have been developed where selective solvation (in terms of the number of solvent molecules) of gas-phase peptide/protein ions is performed and the effect on the gas-phase structure can be determined.[17-19] For example, Jockush *et al.* used blackbody infrared radiative dissociation to investigate the effect of water and metal ion coordination to valine on its gas-phase structure, specifically on zwitterionic formation.[17, 18] Kohtani *et al.* used gas-phase ion equilibrium measurements to study the propensity for different structures (*i.e.*, globular vs. α-helical peptides) to bind water molecules.[19]

Additionally, it is difficult to determine the contribution of intra-molecular interactions, such as hydrogen bonding, hydrophobic forces, van der Waals and cation-π interactions, to protein/peptide structure due to the presence of the dominant protein/peptide-solvent interaction. However, with gas-phase techniques it is possible to specifically measure binding energies[20] and proton affinities.[21, 22] For example, Crowe

et al. determined the binding preferences of a series of crown ethers to various peptides by looking at the energies required for collisionally activated dissociation of the noncovalent complexes.[20] Cassady and coworkers used deprotonation reactions of the analyte of interest with a base to determine the gas-phase basicities of proline containing peptides[22] as well as of bradykinin and its des-arginine derivatives.[21]

IM-MS has previously been used to probe peptide and protein ion structure. Hudgins *et al.* used IM-MS to demonstrate the presence of multiple conformations of the +5 charge state of BPTI as well as how the conformers of the +7 and +8 charge states of cytochrome c changed as a function of solvent conditions.[23] Gill *et al.* experimentally determined the doubly charged species of LHRH, substance P and bombesin have smaller collision cross-sections than their singly charged counterparts.[24] Furthermore, Counterman *et al.* used IM-MS to demonstrate that aggregates of peptides, multiply charged multimers, tend to have spherical conformations.[25]

Gas-phase Hydrogen/Deuterium (H/D) exchange is widely used to investigate protein and peptide ion conformations.[14, 26, 27] Green *et al.* demonstrated the use of gas-phase H/D exchange as a probe of intramolecular interactions within complexes involving a protonated peptides and a sugar moiety.[28] The authors observed a decrease in the rate of H/D exchange despite an increase in labile hydrogens due to complexation of the sugar onto the peptide. Winger *et al.* used H/D exchange to probe conformational differences between disulfide intact and disulfide reduced proteins and observed that the disulfide intact, or native, form had a higher reactivity with D_2O than did the reduced form.[29] Heck and coworkers probed noncovalent complexes of vancomycin-group

antibiotics with cell wall precursor peptides using gas-phase H/D exchange in order to determine the effect of formation of the complex on the original drug structure.[30] The authors observed more exchange in the complexed species than in the free species and concluded that the greater extent of exchange was due to structural changes to a more folded conformer upon complexation.

The utility of combining computational chemistry with mass spectrometry experiments to generate possible structures that correlate with experimental data has been demonstrated. Bowers and coworkers have used IM-MS and molecular mechanics to generate possible structures for bradykinin[31], as well as substance P and bombesin.[24] Alpha-helices in the gas phase have been extensively studied by Jarrold and coworkers with the aid of computational studies.[19, 32, 33]

It is clear that mass-spectrometry-based techniques can be used to elucidate information pertaining not only to gas-phase ion structure but also to solution-phase structure. Furthermore, it is evident that IM-MS, gas-phase H/D exchange and molecular modeling provide complimentary information for the characterization of protein/peptide ion structure. This research uses IM-MS, gas-phase H/D exchange ion molecule reactions, and molecular modeling in addition to circular dichroism and charge state distribution analysis to probe gas-phase peptide ion structure. Data on gas-phase peptide ion structure will be discussed in terms of the intra-molecular interactions present how those interactions change upon alkali salt adduction (i.e., Na^+, K^+ and Cs^+), as well as with the sequence of the peptide. Additionally, the effect of solvent on gas-

phase peptide ion structure, *i.e.*, solution-phase memory effects, will be discussed and gas-phase structures will compared to known solution-phase structures.

CHAPTER II

EXPERIMENTAL

Most near native protein structure studies are conducted in the solution phase using techniques such as Nuclear Magnetic Resonance (NMR) and Circular Dichroism (CD). Such studies are extremely important and relevant as native protein structure and activity occurs in the solution phase. However, studies of gas-phase structure are integral to understanding the effect of intrinsic properties of protein/peptide ions in the absence of solvent (i.e., intra-molecular interactions and charge solvation). Methods such as ion mobility-mass spectrometry (IM-MS), gas-phase hydrogen/deuterium (H/D) exchange, charge state distribution analysis and molecular modeling (MM) can be used in a complimentary fashion to obtain detailed information on the gas-phase conformation of biomolecules. This chapter will detail the gas-phase experimental methods used to investigate the gas-phase conformation of peptides. Solution-phase techniques used to correlate gas-phase conformations to those found in the solution phase will also be discussed.

Ion Mobility-Mass Spectrometry

Ion mobility-mass spectrometry couples drift-time and mass-to-charge (m/z) measurements to yield information about gas-phase structure. Ion mobility-mass spectrometry separation occurs in a drift cell containing a buffer gas across which an electric potential is applied. Ions are pulsed into the drift cell and, depending on their charge, begin to migrate through the buffer gas at a certain velocity. As the ions' charge increases so does the ion's velocity through the drift region. During migration, the ions

will collide with buffer gas molecules, impeding their progress. The larger the ion, the more collisions it will undergo with the buffer gas. Therefore the velocity of the ion through the drift region is dependent on both the ion's charge and collisional cross-section. Due to this dependence, separation of conformers can occur if the differences in their cross-sections are significant (±2.5%).[34] As the ions travel through the drift tube they are constantly tumbling; therefore, the collision cross-sections obtained from experimental data are assumed to be an average of all of the ion's possible orientations in space. By recording the time that it takes the ion to traverse the drift cell, the drift velocity (v_d), the ion's mobility (K) and collision cross-section (Ω) can be calculated. The drift velocity is the average velocity of the ions; it is a balance between the accelerations due to the electric field and the decelerations due to collisions with the buffer gas.[35] Assuming that the number density of the ions is low enough to ignore Coulomb repulsion and that the electric field potential falls within the low-field limit (thermal equilibrium exists between the ions and the buffer gas), the mobility of an ion through a certain buffer gas is simply that ion's velocity divided by the electric potential applied across the cell:

$$K = \frac{v_d}{E} = \frac{L}{t_d E},^{35}$$

where t_d is the drift time, L is the drift length and E is the electric potential. By approximating the ion and buffer gas as hard spheres, the ion's collision cross-section can be calculated from the mobility (K), temperature (T), pressure (P), number density (N^*), masses of both the ion (m_I) and the buffer gas (m_b), and the ion's charge (z):

$$\Omega = \frac{(18\pi)^{\frac{1}{2}}}{16}\frac{ze}{(k_B T)^{\frac{1}{2}}}\left[\frac{1}{m_I}+\frac{1}{m_B}\right]^{\frac{1}{2}}\frac{1}{K}\frac{760}{P}\frac{T}{273.15}\frac{1}{N^*},$$ [36]

where e is ionic charge and k_B is Boltzmann's constant. For a homologous ion series of the same charge, the relationship between mass and cross-section is near linear; as the mass of the ion increases so does the collision cross-section.[37] Therefore, a plot of drift-time versus m/z for such a series should also be near linear.[37] Deviations from the trend line indicate that the mass and collision cross-section are no longer increasing linearly with each other, suggesting that changes in conformation are occurring.

Ion mobility measurements were made using a matrix-assisted laser desorption-ionization (MALDI)-ion mobility reflectron-time-of-flight (TOF) mass spectrometer described previously (Figure 1).[38] The MALDI ion source is equipped with either a high-repetition rate (200-500 Hz), tripled (355nm) ND:YAG laser (JDS Uniphase, San Jose, CA) or a cartridge-type N_2 laser (337 nm, Thermo Laser Science). Threshold laser powers (attenuated with a neutral density filter) were used to collect the arrival time distributions (ATD) for bradykinin and its fragments. The drift cell is a 30.5 cm periodic focusing drift cell operated at ≈1 torr He at room temperature. IM field strengths ranging from 20 to 30 volts/cm·torr were used to acquire arrival time distributions (ATDs). Both the laser power and the E/p ratio were observed to have an effect on the resolution of the ATDs (data not shown). High laser powers resulted in a broadening of the ATD for all species and at high E/p ratios the resolution between the multiple conformations observed in the ATD of BK1-5, BK1-6 and BK1-7 $[M+H]^+$ ions

disappeared. We interpret this to signify that at high laser powers and E/p ratios the ion population sampled by IM-MS is no longer thermal; the ions have internal energy, allowing interconversion between conformers to occur. The mass spectrometer is a 2-stage reflectron TOF mass spectrometer with a path length of ≈1 m.

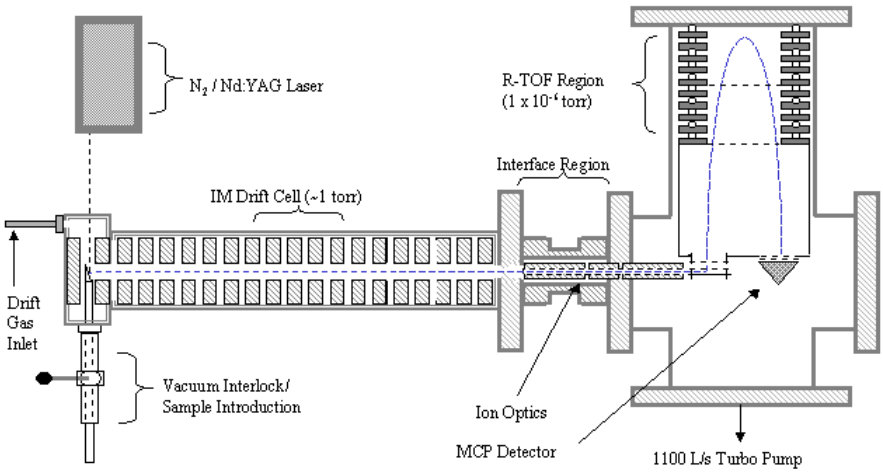

Figure 1. Schematic drawing of the home-built ion mobility-mass spectrometer.

The measured drift time of an ion is a combination of time spent in the drift tube as well as in the ion optic region. Therefore, the drift time must be corrected for the amount of time spent in the lens region in order for accurate cross-section measurements to be made. The amount of time (T) spent in the lens region by the ion can be calculated:

$$T = 72.2M^{\frac{1}{2}} \times \left(\frac{0.21}{V^{\frac{1}{2}}} \right)$$ [39],

where *M* is the mass of the ion, 0.21 is the length of the lens region, and *V* is the lens voltage.

Due to contamination of the helium buffer gas, direct measurement of the collision cross-sections could not be made. The collision cross-sections reported herein were obtained using an internal calibration method.[40] Briefly, a peptide with a known cross-section is used as a standard (bradykinin, 245 $Å^2$)[31] and the difference between the drift times of the standard and the ion of interest is measured multiple times and is used to calculate the Ω of the ion of interest relative to the standard. In a previous work two species were used as standards (C_{60} and bradykinin) and it was found that both species shift according to the amount of contamination *i.e.,* the hard sphere approximation still applies with buffer gas contamination.[40]

The ATDs presented herein are acquired by selecting a narrow mass range from the two-dimensional (mass spectrum and mobility spectrum) data and looking at it in one-dimension (mobility spectrum). The ATDs were also deconvoluted using a gaussian curve-fit equation with Origin graphing software (OriginLab Corporation). Both a single and multiple gaussian curves were used in the equations to determine the best fit of the ATDs. Because the fit will continue to improve by increasing the number of gaussian curves used, the best fit would be the number of gaussian curves, N, that most improved the fit over N-1 gaussian curves and resulted in little to no improvement in the fit of N+1 gaussian curves. For example, although the ATD of BK1-5 $[M+H]^+$ ions generated from MALDI samples prepared in 100% methanol is dominated by a single peak (Chapter VI), the fit of a single gaussian curve (Figure 2A) to the ATD is poor (R^2

= 0.965, Chi^2 = 18.7), with residuals between the fit and the data ranging from +8 to –8 (Figure 2B). The fit of the data is dramatically improved (R^2 = 0.997, Chi^2 = 1.89) when 2 gaussian curves are used (Figure 2C), where the residuals between the fit and the data are reduced to ±4 (Figure 2D). The fit of the data is marginally improved (R^2 = 0.999, Chi^2 = 0.77) when 3 gaussian curves are used (Figure 2E), where the residuals between the fit and the data are further reduced to ranging from +2 to –2 (Figure 2F). Additionally, when choosing the best fit one should consider that the number of parameters of the fit cannot exceed the number of data points being fitted. For example, the ATD of BK1-5 $[M+H]^+$ ions contains 13 data points and each gaussian curve contains 3 parameters. Consequently, four gaussian curves would be the maximum number of fits that may be applied to the ATD of BK1-5 $[M+H]^+$ ions. Considering the above mentioned criteria it can be concluded that the ATD of BK1-5 $[M+H]^+$ ions generated from MALDI samples prepared in 100% methanol is best described by 2 gaussian curves.

Structure indicative information can be obtained from fragmentation spectra of proteins/peptides. Ion mobility-surface-induced dissociation mass spectrometry (IM-SID-MS) is a technique that offers information on the structure through cross-section measurements as well as with fragmentation information. In an IM-SID-MS experiment, ions are formed by MALDI and are separated on the basis of their collision-cross sections in an ion mobility cell. Time-slices of ions are selectively collided onto a surface, inducing fragmentation. Due to the ion mobility based separation of ions prior to dissociation, fragments and their parent ions have the same ion mobility arrival times,

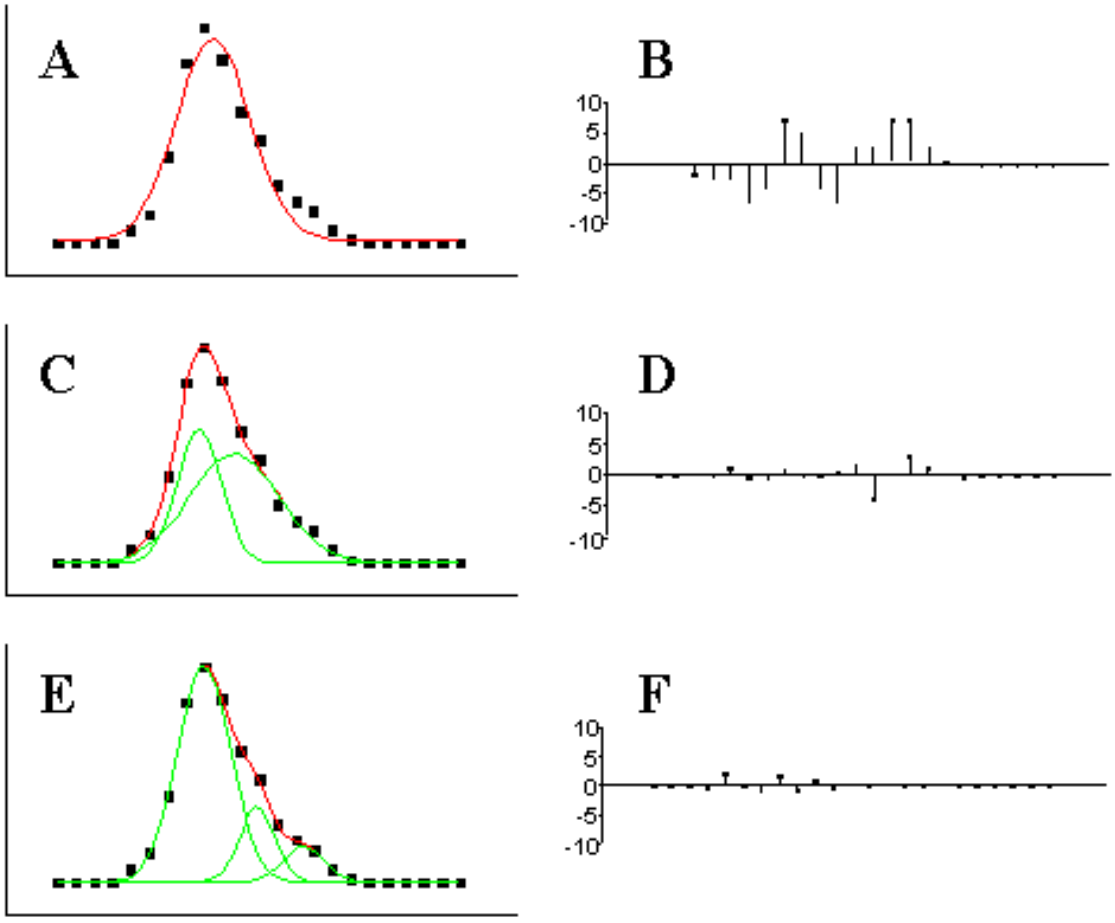

Figure 2. Fits and residuals of the ATD of bradykinin fragment 1-5 $[M+H]^+$ ions generated from MALDI samples prepared in 100% methanol. Red lines delineate the entire fit and green lines delineate the individual gaussian curve. A) Fit of 1 gaussian curve to the ATD of bradykinin fragment 1-5 $[M+H]^+$ ions, B) Plotted residual differences between the data and the fit pictured in A, C) Fit of 2 gaussian curves to the ATD of bradykinin fragment 1-5 $[M+H]^+$ ions, D) Plotted residual differences between the data and the fit pictured in C, E) Fit of 3 gaussian curves to the ATD of bradykinin fragment 1-5 $[M+H]^+$ ions, and F) Plotted residual differences between the data in the fit pictured in E.

making this technique especially useful for studying the fragmentation patterns of different conformers of the same species. Following the dissociation, ions are mass analyzed in a linear time-of-flight (TOF) mass spectrometer. IM-SID-MS experiments were performed on instrumentation described previously (Figure 3).[41] Briefly, ions formed by MALDI and separated using an ion mobility cell are dissociated by energetic (40 eV) collisions with a fluorinated self-assembled monolayer (F-SAM) surface. Helium gas pressures of 1-2 torr were used in the mobility cell.

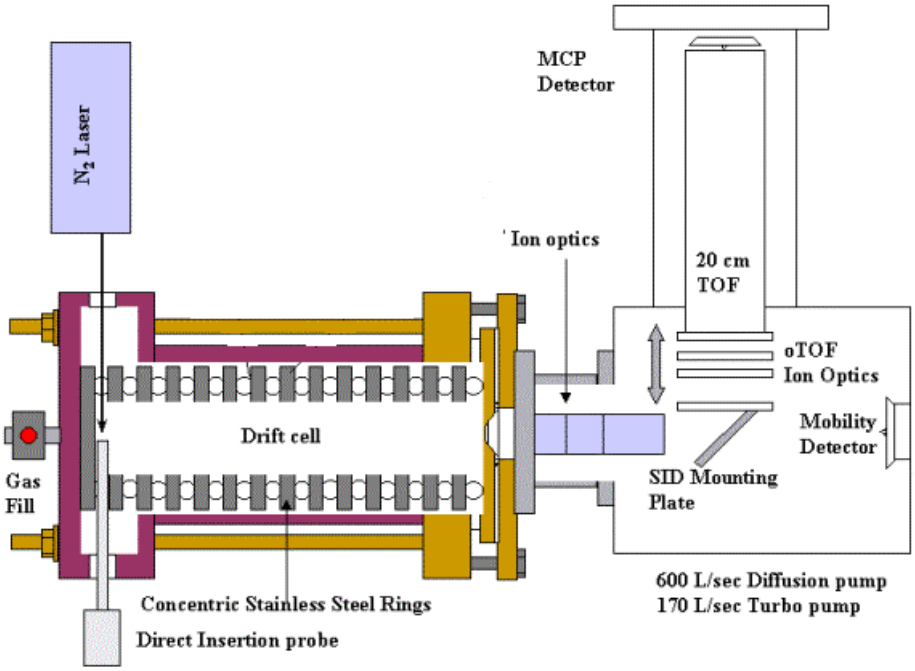

Figure 3. Schematic drawing of the home-built ion mobility-surface-induced fragmentation-mass spectrometer.

Gas-Phase Hydrogen/Deuterium Exchange

Gas-phase Hydrogen/Deuterium (H/D) exchange occurs when a collision complex between a deuterated reagent (D_2O, CD_3OD, ND_3) and a peptide/protein ion results in the exchange of a labile hydrogen (a hydrogen bound to an oxygen, nitrogen or sulfur atom) located on the peptide/protein for a labile deuterium located on the reagent. Gas-phase H/D exchange has been used to characterize protein/peptide structure[42] and to count the number of accessible hydrogens on a protein/peptide.[43] For example, Wang *et al.* resolved different conformations of cardiac muscle troponin C with similar collision cross-sections according to their different rates and extents of exchange with D_2O.[14] Additionally, the authors found that the 6^+ and 7^+ charge states exhibited different gas-phase conformations, according to their H/D exchange behavior, when electrosprayed from different solvent systems, indicating some retention of solution-phase structure in the gas-phase. Different gas-phase conformations of multiply charged states of ubiquitin ions have also been differentiated using gas-phase H/D exchange with D_2O.[26] Freitas *et al.* found that elongated conformers of ubiquitin exchanged slower than the more compact conformers. While this seems counterintuitive to the solution-phase mechanism of H/D exchange, it corresponds the gas-phase relay mechanism for H/D exchange, which requires the charge site and a basic site to be in close spatial proximity with one another in order for facile exchange with D_2O to occur.

Several factors affect the gas-phase H/D exchange reaction including the relative proton affinity of the deuterating agent to the basic sites in the analyte, the number and location of basic sites within the analyte, charge state as well as accessibility of the labile

hydrogen atoms, location of charge sites, ability of the analyte to self-solvate and proximity of function groups, *i.e.*, the secondary/tertiary structure of the reacting ion.[42, 44, 45] Temporal data from H/D exchange experiments are used to calculate rates of exchange, which for idealized systems can yield information about the number of conformers present. Some sites on a peptide/protein have a higher probability of exchange than others, however, the first exchange does not necessarily have to occur at this or any one specific site.[42] The rate of the first exchange is usually a sum of exchange at several different sites on the peptide/protein. Therefore, the $[M+D]^+$ species is most likely comprised of a several species of the peptide/protein labeled with deuterium at different sites.[42] H/D exchange studies discussed herein are focused on the first exchange reaction because of concerns that structural rearrangement reactions of the initially formed peptide ions may occur during the lifetime of the ion-molecule collision complex[46, 47], *i.e.*, time that solvent (H/D reagent) interacts with the ion. The lifetime of the H/D exchange ion-molecule collision complex has previously been investigated both through experimental and theoretical methods and it has been concluded that the complex is particularly long-lived. For example, Campbell *et al.* observed that activation of the ion before the reaction resulted in less exchange and the authors suggest that this is due to the high translational and vibrational energies of the ion reducing the likelihood of formation of a hydrogen-bonded (*i.e.*, long lived) ion-molecule collision complex.[42] Furthermore, the authors concluded from theoretically generated potential energy surfaces that ND_3-peptide complexes can be long lived and undergo multiple exchanges due to the energy and number of wells on the surfaces of the onium ion

mechanism.[42] Additionally, Wyttenbach and Bowers observed, through molecular dynamics simulations, that D_2O forms a long lived (> 1ns) complex with protonated bradykinin ions.[45] Therefore our concerns of possible structural rearrangement reactions are valid and the H/D exchange data must be treated with care. Additionally, the H/D exchange kinetic studies are focused on the first exchange due to the complexity of the kinetics of the exchanges after the first exchange. These exchanges are multi-exponential and therefore it is very difficult to extract information regarding specific sites of exchange.

Some of the rate plots presented herein demonstrate curvature at short reaction times, which has been attributed to vibrationally and translationally hot ions.[42] Ions could be vibrationally and translationally hot due to excitation during the MALDI process. Ion cooling is traditionally accomplished via collisions, however collisions in a Fourier transform-ion cyclotron resonance cell cause extensive ion loss.[49] Quadrupolar axialization is a technique in which ions undergo collisions without ion loss, however it has also been shown to result in excitation of the ions (see below).[49]

Gas-phase H/D exchange of proteins/peptides with D_2O, CD_3OD, or CD_3CO_2D predominantly results in a single exchange per collision event. It has been proposed that D_2O, CH_3OD and CD_3CO_2D exchange via the relay mechanism.[42, 45] In this mechanism exchange occurs when a collision complex between the protein/peptide is created through intermolecular hydrogen bonds with D_2O, CH_3OD or CD_3CO_2D. A hydrogen is extracted from the charge site on protein/peptide by D_2O, CH_3OD or CD_3CO_2D as a deuterium is extracted from the deuterating reagent by a carbonyl group on the

protein/peptide. The deuterium can then be transferred throughout the molecule back to the charge site. If extensive intra-molecular hydrogen bonds exist within the protein/peptide, a collision complex will not be formed, resulting in little to no exchange. Additionally, the charge site and a site basic enough to extract a deuterium from the D_2O, CH_3OD or CD_3CO_2D must be sufficiently close to one another and accessible to the deuterating reagent in order for facile exchange to occur.[42]

Gas-phase H/D exchange with ND_3 is proposed to occur through the "onium" ion mechanism, in which ND_3 extracts a hydrogen from the peptide and the resulting complex is then solvated by the peptide.[44] During the lifetime of the complex, exchange of one (or more) deuterium(s) for hydrogen(s) occurs. Exchange of multiple deuteriums for hydrogens during a single collision event occurs 22% of the time.[42] In order for exchange with ND_3 to occur, the basic sight can not be strongly solvated; it must be accessible to the deuterated solvent.[44]

Gas-phase H/D exchange ion-molecule reactions were carried out using a 3 tesla Fourier transform (FT) ion cyclotron resonance (ICR) mass spectrometer pictured in Figure 4.[48] Ions formed by MALDI using a ND:YAG laser operated at 355nm are trapped in the source region of a two-section cylindrical (4.0cm X 4.0cm) cell (Figure 5). To facilitate H/D exchange, ions were trapped in the presence of deuterated gas for times ranging from 0.005 to 360 seconds. Pseudo-first order kinetics were obtained by operating at background deuterated gas pressures of $6x10^{-8}$ torr. Temporal plots were generated by plotting ion intensity, corrected for the natural isotope abundance, versus time.

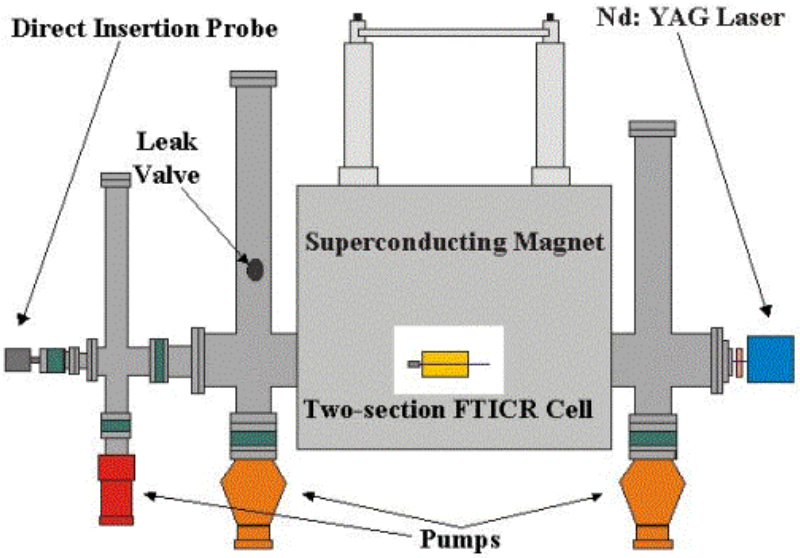

Figure 4. Schematic drawing of the 3 Tesla Fourier transform-ion cyclotron resonance-mass spectrometer.

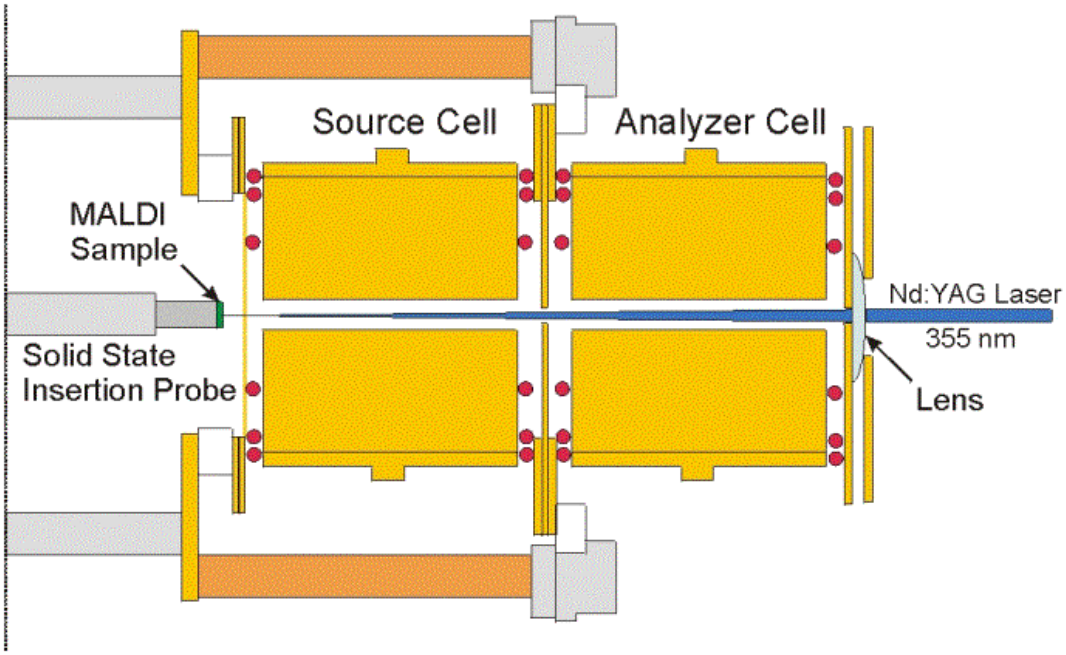

Figure 5. Schematic drawing of the 2-section cell (source and analyzer regions) of the 3-Testla Fourier transform-ion cyclotron resonance-mass spectrometer pictured in Figure 4.

Fourier Transform Ion Cyclotron Resonance Mass Spectrometry

Fourier Transform-Ion Cyclotron Resonance Mass Spectrometry (FT-ICR MS) uses both a magnetic and electric field to trap ions in a cell for long periods of time (minutes to hours). The motion of an ion in an ICR cell is a combination of three types of motion resulting from the electric and magnetic fields. Cyclotron motion, the basis for FT-ICR MS and how ions are mass analyzed, is a result of ions' interaction with the magnetic field (Figure 6B).[49] Cyclotron motion is perpendicular to the plane of the magnetic field (B) and the frequency of cyclotron motion (f_c) is inversely proportional to the mass of the ion (m):

$$f_c = \frac{q\mathrm{B}}{2\pi m},$$[49]

where q is the ion's charge. The second motion an ion undergoes in an ICR cell is trapping motion or axial motion, which arises from the voltages applied to the trapping electrodes, found perpendicular to the magnetic field (Figure 6A).[49] These voltages create a potential well across the cell, resulting in harmonic oscillation of the ion packet between the trapping plates.[49] Magnetron motion, the third ion motion in an ICR cell, is a result of the presence of an electric field in a magnetic field and is pictured in Figure 6C.

To achieve high mass resolution and adequate transfer of ions from the source region (1st section) to then analyzer region (2nd section) of 2-section ICR cell the ion packet must be located in the middle of the ICR cell. Ions formed by MALDI often result in a wide spread plume of ions, in contrast to those formed by electron ionization where the ions are formed in the center of the cell. Additionally if the ions have

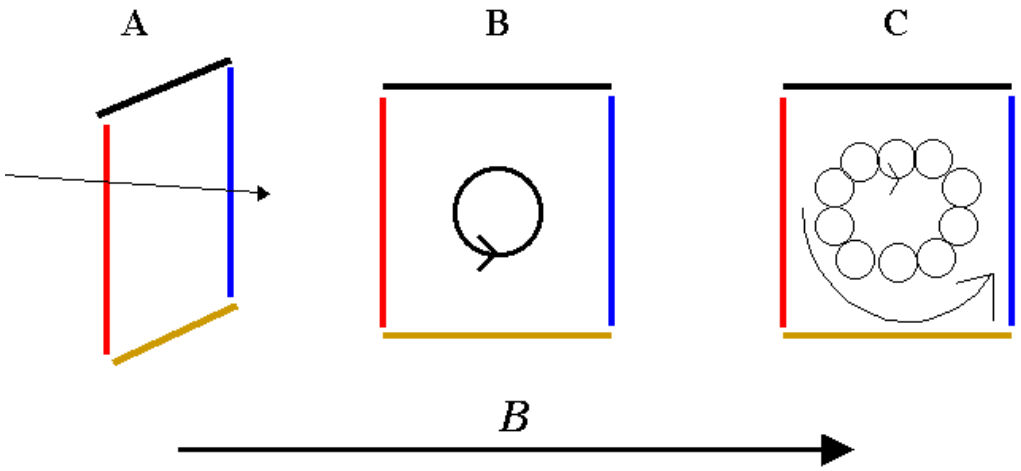

Figure 6. Pictorial representation of the three types of motion an ion undergoes in magnetic and/or electric fields: A) trapping or axial motion, B) cyclotron motion, and C) cyclotron and magnetron motion.

undergone a reaction through collisions, *i.e.*, H/D exchange, ions are no longer located centrally in the ICR cell due to exponential decrease of axial motion and cyclotron radius and an exponential increase in the magnetron radius.[49, 50] Therefore, there is considerable desire for a technique to re-center an ion packet in the ICR cell. Quadrupolar axialization is a technique in which ion excitation in the presence of collisional damping results in returning an ion packet to the center of the cell. During quadrupolar axialization a two-dimensional quadrupolar rf potential with a frequency equal to that of the ion of interest's unperturbed cyclotron frequency is applied in the presence of collisional damping.[49-51] The application of the rf potential results in the inter-conversion of magnetron and cyclotron motions while the collisions result in the exponential increase of magnetron radius and decrease of cyclotron radius.[49-51] The overall effect of the quadrupolar axialization is a periodic decrease in both cyclotron and magnetron radii resulting in a re-centering of the ion packet in the ICR cell.

Marshall and McLafferty report that quadrupolar axialization can lead to heating of the ions which may result in destruction of the intra-molecular interactions that contribute to the structure of the ion.[52, 53] Additionally, Guan *et al.* demonstrated that a quadrupolar axialization voltage of 0.67 V could produce a maximum kinetic energy of approximately 45 eV in less than 1 second.[54] Some of this energy may be converted into internal energy through ion-neutral collisions, resulting in destruction of intra-molecular interactions as well as fragmentation.[54]

Gas-phase H/D exchange ion-molecule reactions were carried out on the 3 tesla FT-ICR mass spectrometer pictured in Figure 4. Ions were formed by MALDI using a ND:YAG laser operated at 355nm. The ions were formed in the source region of a two-section cylindrical (4.0cm X 4.0cm) cell (Figure 5) and either trapped there for the reaction or transferred to the analyzer region of the cell after a quadrupolar axialization event.

Electrospray Ionization Mass Spectrometry: Charge State Distribution Analysis

Analysis of the charge state distribution produced by electrospray ionization (ESI) has recently emerged as a technique to study protein conformation[55] and protein folding dynamics.[56] The charge state distribution in electrospray ionization mass spectra depend on a number of factors, most notably protein/peptide conformation, solvent composition, temperature, and instrumental parameters.[57-59] There have been several suggestions as to how protein conformation contributes to the ESI charge state distribution. One suggestion is that dissimilar conformations of a protein/peptide may yield different charge state distributions in an ESI mass spectrum due to a difference in

the availability of ionizable basic sites between the conformations.[55] Larger conformations may have a higher number of ionizable basics sites on the surface of the protein/peptide and therefore might yield a higher charge state distribution than would a smaller conformation in which the basic sites may be buried. It has been suggested that this mechanism for the conformational dependence of proteins/peptides on the charge state distribution would allow analysis of said distribution to be appropriate only for changes in tertiary structure.[60] Konermann *et al.* suggest that only the breakdown of tertiary structure elements lead to an increase in solvent accessibility, whereas the presence of such secondary structure elements as β-sheets, β-turns and α-helices do not lead to a substantial decrease in solvent accessibility. Alternatively, it has been proposed that unfolded structures are able to stabilize higher charges due to an increased distance between charges of the same polarity whereas more compact structures might not be able to stabilize a high number of like charges due to coulombic repulsion.[61] It has also been suggested that the charge state distribution of proteins/peptides depends on the amount of charge neutralization that occurs during the ESI process.[61] Grandori proposes that neutralization of pre-existing negative charges found in proteins/peptides in bulk solution can more readily occur in unfolded structures where these charges are not participating in intra-molecular interactions, resulting in higher charge states. This mechanism for the conformational dependence of proteins/peptides on the charge state distribution would allow analysis of the charge state distribution to detect changes in the secondary structure in addition to tertiary structure of a protein/peptide.

Several groups have demonstrated the use of charge state distribution analysis in the investigation of protein/peptide structure. Katta *et al.* used analysis of the electrospray charge state distribution to study the conformation of myoglobin under different solution conditions.[62] The authors found than under denaturing pH values the charge state distribution lay at higher values, suggesting the presence of a larger conformation, while under native pH values the charge state distribution centered around lower values, suggesting the presence of a smaller conformation. Konermann and Douglas used a comparison of results from optical spectroscopy and ESI charge state distribution analysis to study the acid denaturation of cytochrome c in different solvent conditions.[63] The authors found that changes in the charge state distribution of cytochrome c occurred at a pH range when a change in the tertiary structure is observed by optical spectroscopy. Douglas has also combined ESI charge state distribution analysis with hydrogen/deuterium exchange[64, 65] and Soret absorption[66] to study protein/peptide folding dynamics and structure.

Studies of the charge state distribution presented here were performed on an electrospray triple quadrupolar reflectron TOF mass spectrometer (MDS Sciex QSTAR Pulsar), shown in Figure 7. Ions are formed by electrospray ionization in the source region and travel through three quadrupoles. After exiting the third quadrupole, ions enter the TOF source where they are pulsed into a reflectron TOF mass spectrometer for mass analysis. The solvent systems used were composed of varying concentrations of water and methanol and analyte concentrations were approximately 1 mg/mL.

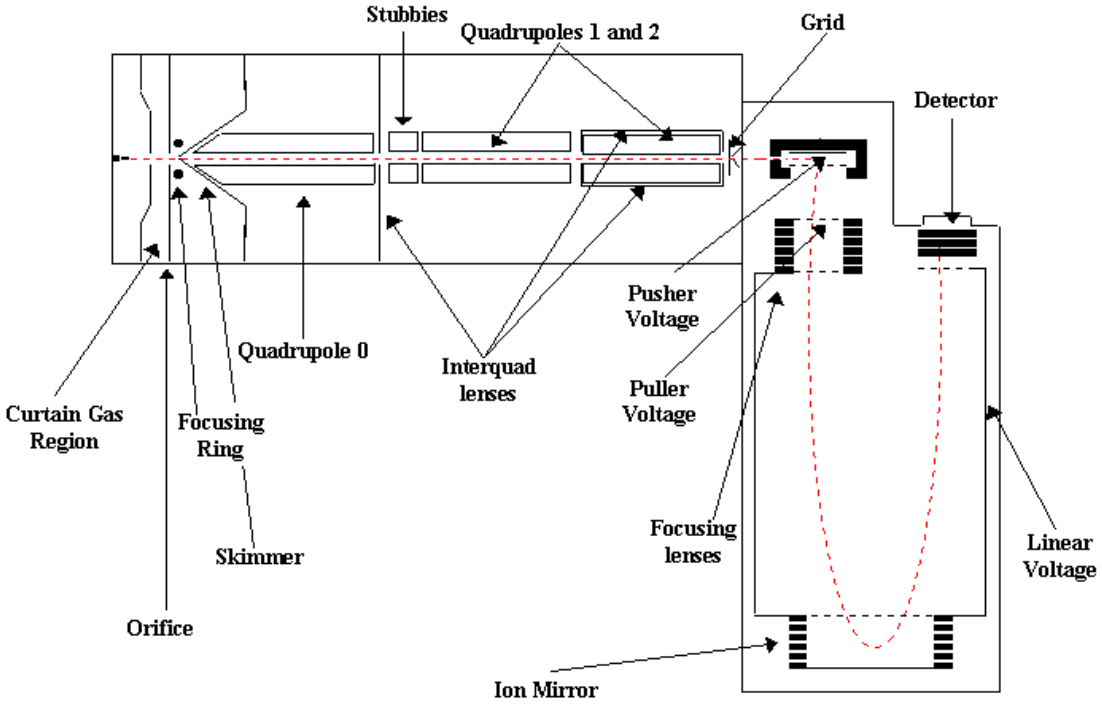

Figure 7. Schematic drawing of the MDS Sciex QSTAR Pulsar electrospray triple quadrupolar reflectron time-of-flight mass spectrometer.

Circular Dichroism

Circular dichroism (CD) is an absorption technique used to quantify secondary structure of proteins/peptides and probe conformational protein/peptide dynamics as a result of perturbation. Specifically, CD measures the difference in absorption of left and right-handed circularly polarized light, the two components of plane polarized light. If one type of circularly polarized light is absorbed, while the other remains the same, the amplitudes of the two types of light are different, resulting in elliptically polarized light. By measuring the difference in absorptivities, CD measures the ellipticity of the circularly polarized light after it has been absorbed. Absorption of circularly polarized

light occurs when an electronic transition has occurred. There are two main types of electronic transitions in peptides/proteins. The first is at the amide bond, which allows the secondary structure of the peptide/protein to be probed. The second is at aromatic amino acid side chains and di-sulfide bonds, allowing the tertiary structure of the peptide/protein to be probed. Fingerprint CD spectra of secondary structure elements such as α-helices, β-sheets, and β-turns have been thoroughly characterized, allowing for easy identification of such elements.[67]

CD experiments were performed on an Aviv 62DS model CD spectrophotometer (Aviv Associates, Lakewood, NJ). A 0.1 mm path length was used and the spectra were taken at 4°C. The wavelength was scanned from 250 nm to 180 nm in 0.5 nm steps with an average time for each step of 3 seconds.

CHAPTER III

A COMPUTATIONAL AID TO STRUCTURE PREDICTION BY ION MOBILITY-MASS SPECTROMETRY

Introduction

Molecular modeling (MM) is becoming increasingly important for the interpretation of experimental results of ion mobility mass-spectrometry (IM-MS). IM-MS can be used to investigate the gas-phase conformation of biomolecules to a limited level of certainty. However, such experimental information can then be used along with MM data to address specific structural issues (*i.e.,* helical vs. globular structure, intra-molecular interactions, charge-stabilization, or salt bridge interactions).

The utility of combining computational chemistry with IM-MS to generate possible structures that correlate with experimental data has been demonstrated. Bowers and coworkers have used IM-MS and molecular dynamics to generate possible structures for bradykinin[31], as well as substance P and bombesin.[24] To generate structures, Bowers uses a simulated annealing technique in which a molecule, to which an all atom forcefield has been applied, is heated to 800K, ramped down to 100K over 10 picoseconds and then minimized. This is repeated, usually 100 times, to generate a population of structures of the molecule. Energies of each molecule are calculated semi-empirically using AM1 and PM3 parameters. Cross-sections of the structures are calculated using a Monte Carlo approach in which the structure is projected onto a plane and random points in the plane are chosen and designated as hits or misses on the

projected structure.[68] The calculated energies and cross-sections are used to generate scatter plots, which are used in structure selection.

Jarrold and coworkers have studied α-helices in the gas phase with the aid of computational studies.[32, 33] Jarrold applies a modified CHARMM forcefield with a 21.3 parameter set to the molecules and then uses a simulated annealing technique to generate a population of structures. During the simulated annealing event, molecules are heated to temperatures ranging from 100K to 700K and times steps from 15 picoseconds to 1 femtoseconds are used. Simulated annealing procedures involving iterative steps of different parameters have also been used by Jarrold and coworkers.[33] The collision cross-sections of each structure are calculated using the projection approximation, the exact hard sphere scattering method and the trajectory method using a program designed by Mesleh, *et al*.[69, 70]

Clemmer and coworkers have also used molecular modeling in conjunction with IM experiments to study the structure of polyalanine helices.[71] The authors used a molecular dynamics approach where a extensible systematic forcefield (BIOSYM DISCOVER 3.0.0) was applied and simulations were performed at an effective temperature of 300 K for times ranging from 0.25 to 1 ns. Theoretical cross-sections for the structures were calculated using the exact hard sphere scattering (EHSS) method and subsequently calibrating the EHSS values relative to trajectory method values.

This chapter will detail the computational process used to generate and select structures that correlate to the gas-phase experimental IM-MS data presented throughout this dissertation. This process will include a simulated annealing procedure used to

generate structures, calculations of semi-empirical energies and cross-sections, analysis of cluster plots as well as selections of structures for higher-level calculations. A model system, tyrosine-containing tripeptides, will be used to evaluate the computational process used. Additionally, the importance of MM in addressing the role of specific structural issues on the interpretation of IM-MS experimental data will be addressed.

Computational Methods

Molecular Dynamics: Simulated Annealing

Simulated annealing is used to generate a population of structures.[72, 73] In this technique, a forcefield is applied to a peptide to define the energy of the system in terms of the position of its atoms, which allows computation of molecular properties that are based on energy (*i.e.*, structure). After application of a forcefield, the ion structure is heated from 300 Kelvin (K) to 1000 K in steps of 50 K with relaxation times of 0.1 picoseconds (ps), making the entire simulation time 280 ps for 100 cycles. All molecular dynamics calculations were performed with the Cerius (Accelrys) suite of programs using the consistent forcefield (CFF1.01).[74]

Energy Calculations

Once a population of structures is generated, their energies are calculated. Semi-empirical calculations using Austin Model 1 parameters were used to determine the energy of each structure.[75] Additionally, higher-level theory (6-311+G(2d.p) basis set) calculations are performed on structures selected from cluster analysis (see below).

Cross-Section Calculations

The collision cross-sections of each structure were calculated by the projection approximation, the exact hard sphere scattering method and the trajectory method using a program designed by Mesleh, *et al*.[69, 70] For both the projection approximation and the exact hard sphere scattering method, each atom in the molecule is represented by a hard sphere with a radii equal to the hard sphere contact distance of that atom. The projection approximation calculates the collision cross-section by averaging the cross-section over all possible orientations in space. This method ignores the possibility of one buffer gas molecule hitting the peptide ion more than once; therefore, the projection approximation tends to underestimate the collision cross-section by 1 to 10%. The exact hard sphere scatter method calculates the collision cross-section by calculating the scattering angles between the incoming and outgoing buffer gas atom. This method tends to overestimate the effect of multiple encounters between the buffer gas and the ion, which overestimates the collision cross-section. The trajectory method calculates the collision cross-section by calculating the scattering angle between the incoming and outgoing buffer gas atom and averaging these over all orientation in space, similar to the exact hard sphere scatter method, but in the trajectory method the atoms of the peptide molecule are represented by Leonard Jones potentials. Cross-sections calculated by the trajectory method tend to fall between those calculated by the projection approximation and the exact hard sphere scattering method. Trajectory method cross-section values were used in the cluster analysis (see below) of $[M+H]^+$, $[M+Na]^+$, $[M+K]^+$, and

$[M+2Na-H]^+$ ions while the projection approximation values were used in the cluster analysis of $[M+Cs]^+$ and $[M+2Cs-H]^+$ ions.

Cluster Analysis

Cluster analysis[76, 77] of the structures generated by molecular dynamics can be used to narrow down the number of candidate structures or to select candidate structures for higher-level theory calculations. Cluster analysis was performed on all peptides by applying three cluster dimensions: AM1 energy value, theoretical cross-section value, and group number. The group number dimension was determined by evaluating the intra-molecular interactions present in each structure. Such an evaluation can be accomplished visually or by measuring the root mean square deviation (RMSD) relative to a standard structure. Once each dimension is plotted, distinct clusters are typically present. The lowest energy structures in the most populated clusters are chosen as candidate structures for evaluation by higher-level theory calculations and/or further experimental data.

Systems Studied

Analysis of the computational approach described above was accomplished by applying the approach to a set of model tyrosine-containing tripeptides (GGY, GYG, and YGG). The protonated and alkali metal ion (Na^+, K^+ and Cs^+) adducted species of the tyrosine-containing tripeptides were studied. Three hundred simulated annealing cycles were applied to the protonated forms of the tyrosine-containing peptides while one hundred simulated annealing cycles were applied to the alkali metal ion adducts of the tyrosine-containing tripeptides. Theoretical cross-sections were calculated for each

peptide. Semi-empirical AM1 parameterized energies were calculated for all peptides with the exception of the Cs^+ adducted species, for which there are no AM1 parameters. Cluster analysis with three parameters (cross-section value, AM1 energy, and group classification) was performed on the tyrosine-containing tripeptides with the exception of the Cs^+ adducted species, for which cluster analysis was performed with two parameters (cross-section values, and group classification). This analysis was used to select tyrosine-containing structures for high-level theory calculations. The lowest-energy structure from the most populated groups was chosen for 6-311+G(2d.p)[78, 79] energy minimization.

Results and Discussion

Techniques such as IM-MS and gas-phase H/D exchange are assumed to sample low-energy structures as opposed to other techniques, such as dissociation, that are probing the sequence and, possibly, structure of activated ions. Therefore, the structures that lie in the local and global minima of the peptide/protein's potential energy surface are candidate structures that might be sampled by IM-MS. Simulated annealing is used to thoroughly sample the potential energy surface of the peptide/protein and generate structures that lie throughout the potential energy surface, especially those that lay in the local and global minima of the surface. The potential energy surface can be considered to be adequately sampled when repeat structures, structures with the same intra-molecular interactions and AM1 energies, are observed. If repeat structures are not observed the number of cycles in the simulated annealing process should be increased. After 300 simulated annealing cycles for protonated GGY, GYG and YGG, the entire

trajectory is represented by 22.3%, 16.9%, and 20.3% of the structures, respectively. This indicates that 77.7%, 81.1% and 79.7% of the trajectory is repeat information, structures that have the same intra-molecular interactions (relatively low, < 2 Å, RMSD values) and/or AM1 energies of structures that have already been observed. Therefore, the simulated annealing approach applied is thoroughly sampling the potential energy surface of the tyrosine-containing tripeptides.

In order to evaluate the validity of the simulated annealing approach in sampling local and global minima high-level theory calculations were performed on select structures of the tyrosine-containing tripeptides. The 6-311+G(2d.p) minimized structures were then compared to the simulated annealed minimized structures and the root mean square deviation (RMSD) of the two structures was determined. A low RMSD value indicates that the simulated annealed minimized structure closely matched

Table 1. Root mean squared deviation values for the 6-311+G(2d.p) minimized and simulated annealing minimized structures of the protonated and alkali metal ion adducted tyrosine-containing tripeptides.

Species	RMSD Values (Å)
$[GGY+H]^+$	0.242
$[GGY+Na]^+$	0.258
$[GGY+K]^+$	0.531
$[GGY+Cs]^+$	0.812
$[GGY+2Cs-H]^+$	0.309
$[GYG+H]^+$	0.217
$[YGG+H]^+$	0.294
$[YGG+Na]^+$	0.439
$[YGG+K]^+$	0.720
$[YGG+Cs]^+$	0.236
$[YGG+2Na-H]^+$	0.059
$[YGG+2Cs-H]^+$	0.270

the 6-311+G(2d.p) minimized structure, indicating that the starting structure (the simulated annealed minimized structure) is a low-energy structure. Shown in Table 1 are the RMSD values for the protonated and alkali metal ion adducted tyrosine-containing tripeptides. All of the RMSD values are below 1 Å, indicating that all of the structures generated by simulated annealing and selected by cluster analysis are low-energy structures. Therefore, the simulated annealing approach is sampling structures that lie in the local and/or global minima of the potential energy surface of the peptides.

Energy measurements are a fundamental part of computational analysis for structure prediction because IM-MS experimental techniques sample low-energy conformations. *Ab initio* and density functional theory (DFT) calculations made with a reasonable basis set can be used to study small molecules but for larger molecules (> 50 atoms), or a large number of structures, such calculations become extremely time intensive. An alternative to *ab initio* calculations is to calculate the energy semi-empirically by applying a set of parameters on the molecules in order for time-saving approximations to be made.[75] AM1 parameterized semi-empirical energies were calculated for all protonated and alkali metal ion adducted species of the tyrosine-containing tripeptides with the exception of Cs^+ adducted species for which there are no parameters. *Ab initio* energy calculations were also performed on structures selected from cluster analysis. While the value of the energies might change when the level of theory is changed, the use AM1 parameterized semi-empirical energies in place of *ab initio* energy calculations can be evaluated by comparing the relative order of energies of the structures. For a set of five peptides, several structures were chosen from cluster

analysis to be energetically evaluated by AM1 and *ab initio* calculations. The order of energies as calculated by DFT without zero-point energy corrections were compared to the order of AM1 calculated energies. For all but two of the species the lowest energy species was the same for both the AM1 and DFT calculations. For the two cases in which the lowest energy structure as calculated with AM1 parameters was not the lowest energy structure as calculated by DFT, the two structures' DFT-calculated energies differed by less than 0.01 atomic units (≈6 kcal/mol). Therefore, while AM1 calculations are an excellent method for cursory energy calculations for a large population of structures, calculations at a higher level of theory are recommended for a small number of structures selected by cluster analysis.

The theoretical calculation of cross-sections of computationally generated structures is integral to structure prediction by IM-MS. There are several methods currently employed for cross-section calculations.[69, 70, 80] The collision cross-sections of each structure were calculated using the projection approximation, the exact hard sphere scattering method and the trajectory method using a program designed by Mesleh, *et al*.[69, 70] All of the theoretically calculated cross-sections are within 2% of the experimentally determined cross-sections (see Chapters IV-VI).

Once a population of structures is generated, their energies and hard sphere collision cross-sections are calculated. Several different structures will have a calculated cross-section that is within the error of the experimental cross-section measured by IM-MS, making it necessary for more characteristics of the ion of interest to be known before a structural assignment can be made. Cluster analysis[76, 77] of the structures

generated by molecular dynamics can be used to narrow down the number of candidate structures or to select candidate structures for higher-level theory calculations by organizing a large amount of information into differently populated subsets. Selection of statistically favorable structures is accomplished by looking at a cluster plot in the desired cross-section and energy range and choosing structures from the most populated cluster. Cluster analysis based on three dimensions (AM1 energy value, theoretical cross-section value, and group number) does very well in systematically selecting structures that accurately represent the experimental data. In a specific case, through the use of cluster analysis, a 4% difference in experimentally calculated cross-sections was attributed to the presence of cation-π interactions in one molecule and the absence such interactions in the other (see Chapter IV). Furthermore, cluster analysis was able to determine that a 5 $Å^2$ difference in cross-section was due to slight differences in the intra-molecular interactions resulting in the presence of a β-turn in one conformation and its absence in the other (see Chapter VI). Agreement between the theoretical and experimental cross-sections is well within 2%, when three-dimensional cluster analysis is applied, with the percent difference often being less than 1 (see Chapters IV-VI).

Conclusions

It is evident from current literature that the use of computational techniques in the interpretation of experimental data for structural characterization is continually rising. Computational techniques are used to generate a population of structures, calculate the energies and cross-sections of those structures as well as select structures that are used in conjunction with experimental data to form realistic hypothesis

regarding gas-phase peptide structure. Due to the emphasis placed on the computationally generated structures in the interpretation of experimental data, validation of the computational technique used is necessary. The computational approach presented in this chapter includes a simulated annealing procedure used to generate structures, calculations of semi-empirical energies and cross-sections, analysis of cluster plots as well as selections of structures for higher-level calculations. Application of the approach to a model system, tyrosine-containing tripeptides, successfully validated the approach. It was effectively demonstrated that the simulated annealing technique thoroughly samples the entire potential energy of the tyrosine-containing tripeptides. Additionally, the use of AM1 parameters for the semi-empirical calculation of the energies of the structures was shown to be an effective method for establishing the relative energies of a large number of structures while not requiring the time that *ab initio* calculations do. Accurate (within 2% of experimental value) calculation of theoretical cross-sections through the use of the program designed by Mesleh, *et al.*[69, 70] was also achieved. Finally, the use of cluster analysis aids in the systematic selection of structures for higher-level theory calculations as well as for selection of candidate structures that accurately describe the experimental data. Overall, the computational approach described in this chapter is suitable computation companion to IM-MS experimental data for the prediction of structure.

CHAPTER IV

INVESTIGATION OF THE EFFECT OF SALT ADDUCTION ON THE GAS-PHASE STRUCTURE OF TYROSINE-CONTAINING PEPTIDES USING ION MOBILITY AND H/D EXCHANGE MASS SPECTROMETRY

Introduction

Studies of native proteins/peptides in solution clearly illustrate that a delicate balance of multiple forces determines the secondary and tertiary structures of proteins/peptides. Forces such as those between the solvent and the protein/peptide as well as intra-molecular interactions such as hydrogen bonding, van der Waals interactions and hydrophobic forces have all been recognized for their key roles in determining protein/peptide structure. Additionally, the noncovalent cation-π interaction has also been found to be a dominant force in many molecular biology systems, particularly in protein/peptide structure. For example, it has been observed that NH groups in a protein/peptide tend to be near aromatic side chains. In a statistical study of 33 diverse proteins, 50% of the aromatic side chains were in close contact with amino groups, indicating that cation-π interactions might have a significant influence on protein/peptide structure.[81] Cation-π interactions have also been observed to influential in other molecular biological systems such as the binding of acetylcholine, alkylating reactions involving S-adenosylmethionine, as well as steroid biosynthesis.[82] Additionally, cation-π interactions have been observed to be particularly important in the selectivity of K^+ and Na^+ cations over other alkali metals in ion channels, indicating that cation-π interactions might be extremely important in salt adduction processes.[82]

Alkali metal ion adduction has been studied by mass spectrometry for over a decade. Russell and Mallis used CID to study sodium adducts of model peptides and concluded that, upon sodium ion adduction, the cation coordinates to the most basic sites in the molecule. They proposed that the sodium cation is preferentially coordinated to the nitrogen present in the highly basic side chains of arginine and/or histidine, and to the amide nitrogens along the backbone of the peptide as well as to the N-terminus.[8] For molecules in which two sodium ions were adducted, it is suggested that the second sodium interacts with the free carboxy terminus of the molecule.[83] Gross and coworkers observed different fragmentation patterns for metastable ion decay versus CID. However, from both of the fragmentation patterns they deduce that Li^+ and Na^+ cations interact with the carbonyl oxygens and the C-terminus.[84] Teesch and Adams investigated alkali metal adduction with the group 1 alkali metals[85] and concluded that while the place of metal adduction depends on the size of the cation, the main interactions are between the cation and the carbonyl oxygens along the backbone with some contributing interactions from basic side chains.[86] Wesdemiotis and coworkers used post-source decay to study Na^+ and K^+ adduction and concluded that the cations mainly interact with the carbonyl oxygens on the backbone.[87]

The binding energies of several cations to various ligands have been measured. It can be noted that as the radius of the cation increases the binding energy decreases. For example, the binding energy of Li^+, Na^+, and K^+ to benzene is 38.3, 28.0, and 19.2 kcal/mol, respectively.[88] Ion beam experiments performed by Armentrout and coworkers indicate that the binding energies of Na^+ to a carbonyl functionality is 32 ± 8

kJ/mol, to water is 95 ± 8 kJ/mol, and to NH_3 is 102 ± 5 kJ/mol.[88] Additionally, the binding energy of Na^+ to benzene is 88 ± 4 kJ/mol while the binding energy to C_6H_5OH is 99 ± 3 kJ/mol.[88] Furthermore, the binding energy of Na^+ to imidazole (arginine side chain moiety) and pyridine (histidine side chain moiety) have been measured to be 140 ± 5 and 127 ± 3 kJ/mol, respectively.[88] These values can be compared to 32 ± 8 kJ/mol for CO and 102 ± 5 kJ/mol for NH_3, binding energies of cations to other functional groups (or functional group mimics) found in peptides.[88] From these results it can be concluded that the cation-π interaction is an extremely competitive interaction to other intra-molecular interactions found in peptide and protein molecules.

Ion mobility-mass spectrometry (IM-MS) has also been used to study alkali ion adducts. For example, Bowers and coworkers have observed alkali ion adducts to deviate from the expected linear relationship observed in ion mobility.[31] These deviations were rationalized in terms of conformational change to the peptide upon alkali metal ion adduction.[89] By comparing IM-MS data with computational structures, Bowers and coworkers concluded that when sodium binds to sugars, the metal strongly interacts with six to seven oxygens from the sugar moiety, and the most stable conformer of the sodiated saccharide had a globular shape.[90] They also observed that sodium adducts of bradykinin had similar cross-sections to that of the protonated peptide.[31] Additionally, Hill and coworkers have observed similarities between the collision cross-sections of the protonated and sodiated species of certain drugs, and in some cases, such as heroin, the sodiated species has a smaller collision cross-section than does the protonated species.[91] They interpreted these results to indicate that the oxygen groups

on the drug interact with the sodium to form a compacted ion. Bowers and coworkers also report IM-MS data for adduction of larger alkali metals, concluding that the charge solvation structure is more stable upon adduction of larger cations (K^+, Rb^+, Cs^+).[89] They predict that alkali cationization of basic residues results in a zwitterionic structure. For smaller alkali metal adducted species, they suggest the structures exist as salt bridges. They also compared the mobilities of Li^+, Na^+, and Cs^+ cationized polymers.[92] Structures were obtained from molecular modeling that showed that all three cations coordinate to oxygen atoms with lithium coordinating to the least number, sodium next and cesium the most.

The tyrosine moiety has been observed to be extremely important in cation-π interactions found in many molecular biology systems. Specifically, tyrosine is present in both Na^+ and K^+ channels and has been directly linked to the specificity of K^+ channels.[88] A conserved tyrosine-containing sequence is found in the pore region of K^+ channels and appears to be essential for K^+ selectivity.[93] IM-MS and Hydrogen/Deuterium (H/D) ion-molecule experiments performed on tyrosine containing tripeptides and the salt adducted species as well as proposed structures, generated from molecular modeling, will be presented in this chapter. This data will be discussed in terms of the intra-molecular interactions present in the protonated species and how those interactions change upon alkali salt adduction, as well as how the sequence of the peptide, particularly the placement of the aromatic tyrosine residue, affects the intra-molecular interactions present in the peptides.

Experimental and Computational Methods

Mobility measurements were made using a matrix-assisted laser desorption-ionization (MALDI) ion mobility (IM) time-of-flight (TOF) mass spectrometer (MS) described previously (see Chapter II). Briefly, ions formed by MALDI drift through the IM cell (0.5-5 torr of Helium) where they are separated on the basis of collision cross-section (Ω). The collision cross-sections reported herein were obtained using an internal calibration method.[40] Briefly, a peptide with a known cross-section is used as a standard (bradykinin) and the difference between the drift times of the standard and the ion of interest is measured multiple times and is used to calculate the Ω of the ion of interest relative to the standard. The arrival time distributions (ATDs) presented in this paper are acquired by selecting a narrow mass range from the two-dimensional (mass spectrum and mobility spectrum) data and looking at it in one-dimension (mobility spectrum). The ATDs of GGY and YGG $[M+H]^+$ and $[M+Cat]^+$ (where Cat is an alkali metal ion) ions were deconvoluted using a gaussian curve-fit equation with Origin graphing software (OriginLab Corporation). Both a single and multiple gaussian curves were used in the equations to determine the best fit of the ATDs. Because the fit will continue to improve by increasing the number of gaussian curves used, the best fit would be the number of gaussian curves, N, that most improved the fit over N-1 gaussian curves and resulted in little to no improvement in the fit of N+1 gaussian curves. For the $[M+H]^+$, $[M+Na]^+$, $[M+K]^+$, $[M+Cs]^+$, $[M+2Na-H]^+$, and $[M+2Cs-H]^+$ ions of both GGY and YGG, the ATDs were best fit with one gaussian curve. For the mixture of GGY and YGG $[M+H]^+$ ions, the ATD was best fit with two gaussian curves.

Gas-phase H/D exchange ion-molecule reactions were carried out on a 3 tesla Fourier transform (FT) ion cyclotron resonance (ICR) MS described previously (see Chapter II). Ions were formed by MALDI using a ND:YAG laser operated at 355nm. The ions were formed in the source region of a two-section cylindrical (4.0cm X 4.0cm) cell and either trapped there or transferred to the analyzer region of the cell after a quadrupolar axialization event. To facilitate H/D exchange, ions were trapped in the presence of methanol-d_4 gas for times ranging from 0.005 to 900 seconds. Pseudo-first order kinetics were obtained by operating at background deuterated gas pressures of $6x10^{-8}$ torr. Temporal plots were generated by plotting ion intensity, corrected for the natural isotope abundance, versus time.

All molecular dynamics calculations were performed with the Cerius (Accelrys) suite of programs using the consistent forcefield (CFF1.01). Model structures for the peptide ions were generated using a simulated annealing cycle[72, 73] where the structure was heated from 300 Kelvin (K) to 1000 K in steps of 50 K with relaxation times of 0.1 picoseconds (ps), making the entire simulation time 280 ps for 100 cycles. Semi-empirical calculations using AM1 parameters were used to determine the energy of the protonated, sodiated and potassiated species. The collision cross-sections of each structure were calculated using the projection approximation, the exact hard sphere scattering method and the trajectory method using a program designed by Mesleh, *et al*.[69, 70] The trajectory method values were used for protonated, sodiated and potassiated species while the projection approximation values were used for the cesiated species. Cluster analysis of the structures generated by molecular dynamics, in which the

conformations are evaluated and grouped into clusters based on similarities in intra-molecular interactions, was used to select candidate structures for higher-level theory calculations. Energies of select structures and charge density surfaces were calculated with the 6-311+G(2d.p)[78, 79] basis set. The structures proposed herein were chosen based on agreement between the experimental collision cross-section, cluster population (structures in the most populated cluster within the cross-section range were considered most likely) as well as energy level. Structures proposed in this chapter are within 6 kcal/mol of the lowest energy structure (with the exception of the cesium containing peptides for which AM1 energies could not be calculated). The calculated collision cross-section of each proposed structure was within 3 $Å^2$ of the experimentally measured collision cross-section.

Peptides were purchased from Sigma Aldrich and Bachem and used without further purification. 2', 4', 6'-trihydroxyacetophenone monohydrate, 3-amino benzoic acid, D(-)fructose, and methanol-d_4 were purchased from Sigma Aldrich and used without further purification. Alpha-cyano-4 hydroxycinnamic acid was purchased from Sigma Aldrich and was recrystalized prior to use. HPLC grade methanol and deionized (Milli-Q Water System, Millipore) water were used for all experiments. The solutions for IM-MS measurements were prepared using either α-cyano-4 hydroxycinnamic or 3-amino benzoic acid as matrix with a matrix-to-analyte molar ratio of 100-150:1. The collision cross-sections of the alkali metal adducts of GYG could not be measured due to low abundance. Solutions for the H/D exchange reactions were prepared using 2', 4', 6'-trihydroxyacetophenone monohydrate as matrix and D(-)fructose as a matrix additive

with a additive:matrix:analyte molar ratio of 1000:500:1. D(-)fructose has been previously been observed to reduce the internal energies of the ions resulting in enhanced ionization and less fragmentation[94] and it was for this reason that D(-)fructose was added to the MALDI sample preparation for the H/D exchange ion-molecule reactions presented in this chapter. In the cases for H/D exchange of the protonated forms of GGY, GYG and YGG a cation-exchange resin was used in the MALDI preparation to facilitate formation of the protonated species over salt-adducted species. The cation-exchange resin (AG 50W, mesh size: 100-200 μm) was obtained from Bio-Rad laboratories in the proton form. It was converted from the proton form to the ammonium form by washing the resin with concentrated ammonium hydroxide and then flushing with deionized water to wash out any salts.[95] The ammonium-form resin was then vortexed for 30 minutes with the peptide, matrix and fructose to ensure that all salts were extracted from the samples before the MALDI sample was prepared for the H/D exchange experiment.

Results

The ATD of $[GGY+H]^+$ ions, shown in Figure 8A, reflects that of a single conformer having a collision cross-section of 121 ± 4 Å^2. The ATD of $[YGG+H]^+$ ions, shown in Figure 8B, also reflects that of a single conformer, however, the collision cross-section of YGG is calculated to be 116 ± 4 Å^2, making $[M+H]^+$ ions of YGG ≈4% smaller in collision cross-section than those of GGY. The difference in collision cross-section is effectively illustrated by the ATD of a mixture of $[YGG+H]^+$ and $[GGY+H]^+$ ions shown in Figure 8D. The collision cross-section of $[GYG+H]^+$ ions (ATD shown in

Figure 8C) was measured to be 113 ± 7 Å^2, making protonated GYG smaller than both protonated YGG and GGY by ≈3% and ≈7%, respectively.

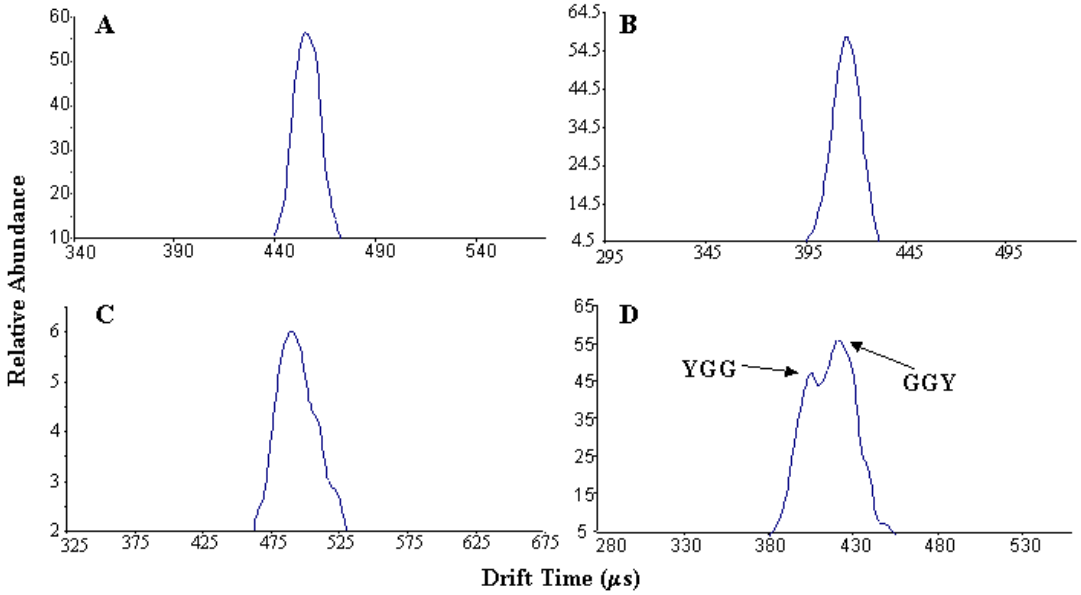

Figure 8. Arrival time distributions of $[M+H]^+$ ions of A) GGY, B) YGG, C) GYG, and D) GGY and YGG.

The collision cross-sections of the alkali metal adducts of GGY and YGG were also measured (see Table 2). A decrease in collision cross-section relative to the $[M+H]^+$ ions was observed upon adduction of sodium and potassium to GGY, whereas an increase in collision cross-section relative to the $[M+H]^+$ ions was observed upon adduction of sodium and potassium to YGG. The 2-dimensional mass-mobility plots of GGY ions and YGG ions are shown in Figures 9 and 10, respectively, with numbered peaks listed in Tables 3 and 4, respectively. The ATDs of the alkali adducts of GGY and YGG are also pictured in Figures 11A and B, respectively. The collision cross-section

of $[GGY+Na]^+$ ions was measured to be 116 ± 6 $Å^2$, making $[GGY+Na]^+$ ions ≈4% smaller in cross-section than $[GGY+H]^+$ ions. $[GGY+K]^+$ ions were measured to have a collision cross-section of 119 ± 7 $Å^2$, making $[GGY+K]^+$ ions 2% smaller in cross-section than $[GGY+H]^+$ ions. On the contrary, the collision cross-section of $[YGG+Na]^+$ ions was measured to be 121 ± 4 $Å^2$, making $[YGG+Na]^+$ ions ≈4% larger in cross-section than $[YGG+H]^+$ ions. Furthermore, $[YGG+K]^+$ ions were measured to have a collision cross-section of 123 ± 4 $Å^2$, making $[YGG+K]^+$ ions ≈6% larger in cross-section than $[YGG+H]^+$ ions.

Table 2. Experimentally calculated collision cross-sections of protonated and alkali metal ion adducted species of GGY and YGG.

GGY Species	Experimental Ω	YGG Species	Experimental Ω
$[GGY+H]^+$	121	$[YGG+H]^+$	116
$[GGY+Na]^+$	116	$[YGG+Na]^+$	121
$[GGY+K]^+$	119	$[YGG+K]^+$	123
$[GGY+Cs]^+$	125	$[YGG+Cs]^+$	128
$[GGY+2Na-H]^+$	115	$[YGG+2Na-H]^+$	123
$[GGY+2Cs-H]^+$	140	$[YGG+2Cs-H]^+$	142

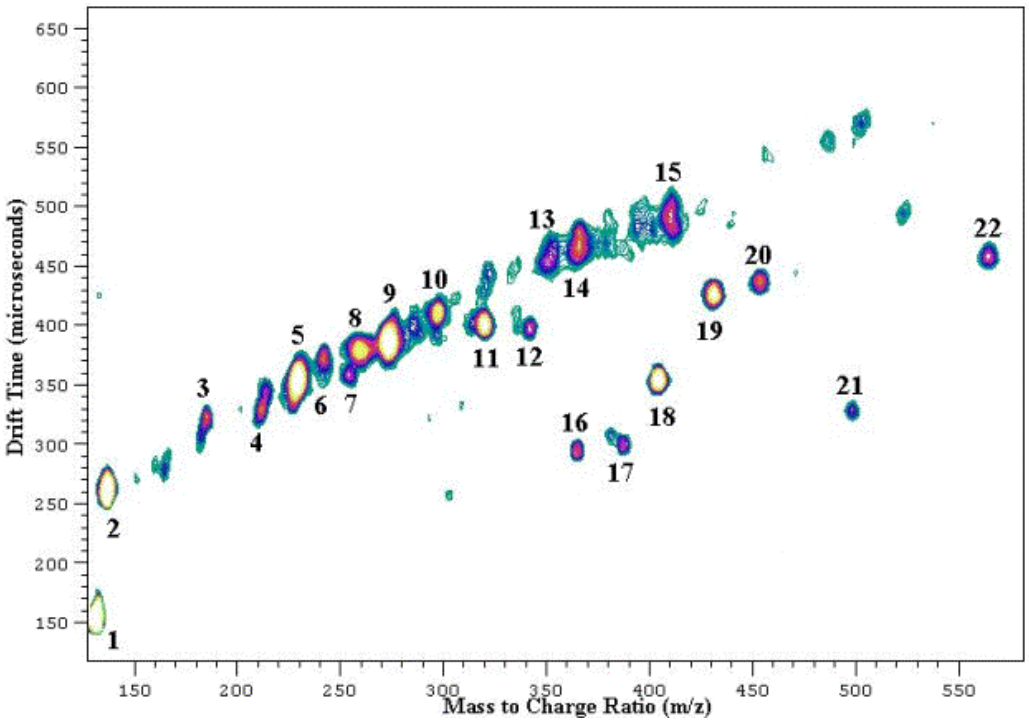

Figure 9. Two-dimensional mass-mobility plot of GGY ions.

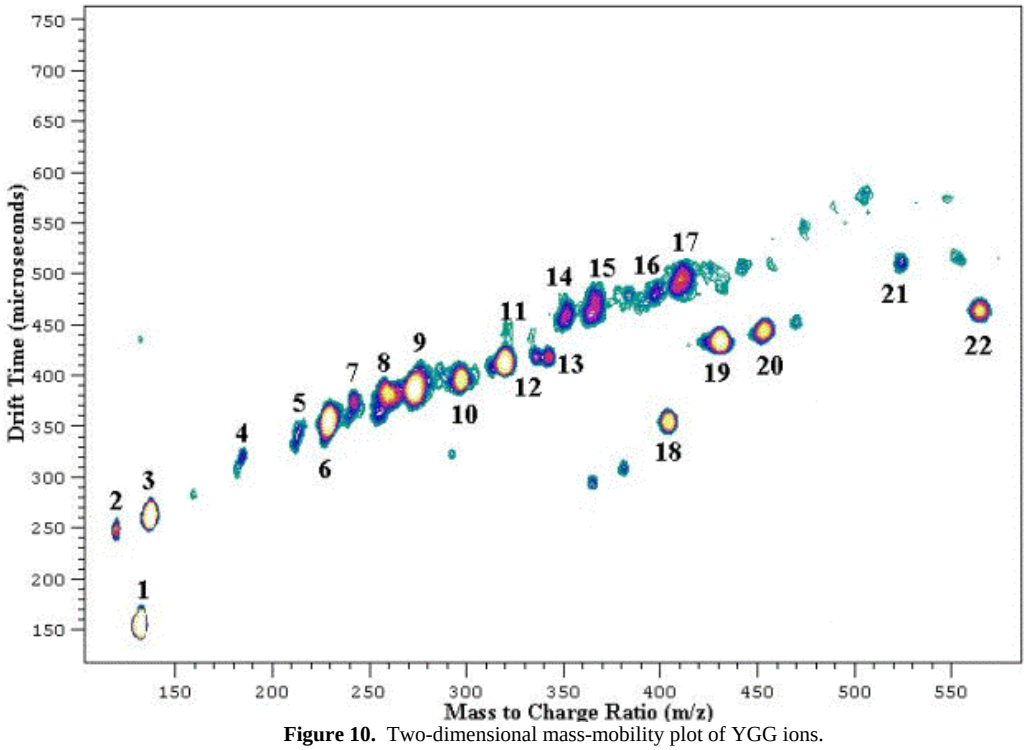

Figure 10. Two-dimensional mass-mobility plot of YGG ions.

Table 3. List of identified peaks in the two-dimensional mass-mobility plot of YGG ions.

Peak Number	Species
1	Cs^+
2	[3-Aminobenzoic acid]$^+$ (matrix)
3	[3-Aminobenzoic acid + 2Na - H]$^+$
4	[3-Aminobenzoic acid dimer – COOH – NH_2]$^+$
5	[3-Aminobenzoic acid dimer – COOH]$^+$
6	y^2 fragment of GGY or [3-Aminobenzoic acid dimer – $2NH_2$]$^+$
7	[GGY – CONH]$^+$
8	[3-Aminobenzoic acid dimer – H_2O]$^+$
9	[3-Aminobenzoic acid dimer + H]
10	[GGY + H]$^+$
11	[GGY + Na]$^+$
12	[GGY + 2Na - H]$^+$
13	[3-Aminobenzoic acid trimer – COOH – NH_2]$^+$
14	[3-Aminobenzoic acid trimer – COOH]$^+$
15	[3-Aminobenzoic acid trimer + H]$^+$
16	[Cs_2Cl + K + Na]$^+$
17	[Cs_2Cl + K + 2Na]$^+$
18	[Cs_2Cl + 2K + Na]$^+$
19	[GGY + Cs]$^+$
20	[GGY + Cs + Na – H]$^+$
21	[Cs_3Cl + K + Na]$^+$
22	[GGY + 2Cs – H]$^+$

Table 4. List of identified peaks in the two-dimensional mass-mobility plot of YGG ions.

Peak Number	Species
1	Cs^+
2	[3-Aminobenzoic acid – H_2O]$^+$
3	[3-Aminobenzoic acid + H]$^+$
4	[3-Aminobenzoic acid + 2Na – H]$^+$
5	[3-Aminobenzoic acid dimer – COOH – NH_2]$^+$
6	[3-Aminobenzoic acid dimer – COOH]$^+$
7	y^2 fragment of YGG or [3-Aminobenzoic acid dimer – $2NH_2$]$^+$
8	[3-Aminobenzoic acid dimer – H_2O]$^+$
9	[3-Aminobenzoic acid dimer + H]$^+$
10	[YGG + H]$^+$
11	[YGG + Na]$^+$
12	[YGG + K]$^+$
13	[YGG + 2Na – H]$^+$
14	[3-Aminobenzoic acid trimer – COOH – NH_2]$^+$
15	[3-Aminobenzoic acid trimer – COOH]$^+$
16	[3-Aminobenzoic acid + 2Cs – H]$^+$
17	[3-Aminobenzoic acid trimer + H]$^+$
18	[Cs_2Cl + 2K + Na]$^+$
19	[YGG + Cs]$^+$
20	[YGG + Cs + Na – H]$^+$
21	[YGG + 2(3-Aminobenzoic acid) – COOH]$^+$
22	[YGG + 2Cs – H]$^+$

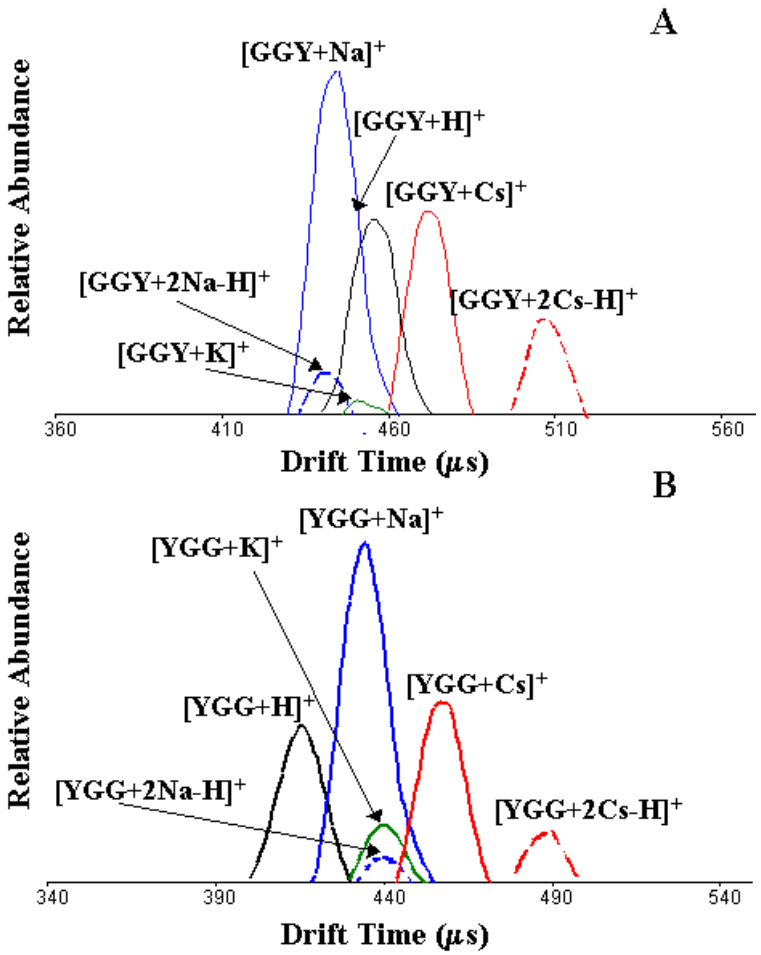

Figure 11. Arrival time distributions of $[M+H]^+$, $[M+Na]^+$, $[M+K]^+$, $[M+Cs]^+$, $[M+2Na-H]^+$, $[M+2Cs-H]^+$ ions of A) GGY, and B) YGG.

Similar behavior is observed upon the adduction of 2 sodium ions to the tyrosine-containing tripeptides. The collision cross-section of $[GGY+2Na-H]^+$ ions was measured to be 115 ± 4 Å^2, making $[GGY+2Na-H]^+$ ions ≈5% smaller in cross-section than $[GGY+H]^+$ ions and ≈1% smaller than $[GGY+Na]^+$ ions. Whereas, the collision cross-section of $[YGG+2Na-H]^+$ ions was measured to be 123 ± 5 Å^2, making $[YGG+2Na-H]^+$ ions ≈6% larger in cross-section than $[YGG+H]^+$ ions and ≈2% larger than $[YGG+Na]^+$ ions.

The collision cross-sections were larger upon adduction of cesium to both GGY and YGG. The collision cross-section of $[GGY+Cs]^+$ ions was measured to be 125 ± 4 $Å^2$, making $[GGY+Cs]^+$ ions ≈3% larger in cross-section than $[GGY+H]^+$ ions. Upon adduction of two cesium ions the collision cross-section was measured to be 140 ± 4 $Å^2$, making $[GGY+2Cs-H]^+$ ions ≈14% larger in cross-section than $[GGY+H]^+$ ions and ≈11% larger than $[GGY+Cs]^+$ ions. The collision cross-section of $[YGG+Cs]^+$ ions was measured to be 128 ± 4 $Å^2$, making $[YGG+Cs]^+$ ions ≈9% larger in cross-section than $[YGG+H]^+$ ions. $[YGG+2Cs-H]^+$ ions were measured to have a collision cross-section of 142 ± 4 $Å^2$, making $[YGG+2Cs-H]^+$ ions ≈18% larger in cross-section than $[YGG+H]^+$ ions and ≈10% larger than $[YGG+Cs]^+$ ions. The collision cross-sections of the alkali metal adducts of GYG could not be measured due to low abundance.

In an effort to better understand the structure of GGY and YGG gas-phase H/D exchange experiments were performed. Ion abundance was monitored as a function of reaction time with deuterated methanol (MeOH-d_4). Discussion and interpretation of H/D exchange reaction kinetics is focused on the first exchange for reasons detailed in CHAPTER II. GGY, GYG and YGG undergo H/D exchange to somewhat similar extents. Additionally the slopes of the rate plots of the first exchange are very similar in value being 0.12, 0.11, and 0.10, respectively. The alkali metal adducts (sodium and cesium) of GGY, GYG and YGG all undergo H/D exchange to a decreased extent as compared to the protonated species. The rates and orders of exchange of these species are similar, as well.

As stated earlier, $[GGY + H]^+$ ions exchange up to four hydrogens for deuteriums in 35 seconds, as seen in the temporal plot shown in Figure 12A. The rate plot of the first exchange, shown in Figure 12B, is a straight line with a slope of 0.10. The sodium and cesium adducted species of GGY exchange both slower and to a lesser extent than does the protonated species of GGY, as seen in the temporal plots shown in Figures 13A, C and E, respectively. The rate plots for the first exchange of each of these species, shown in Figures 13B, D and F, is a straight line with similar slopes (0.016, 0.010, and 0.005, respectively).

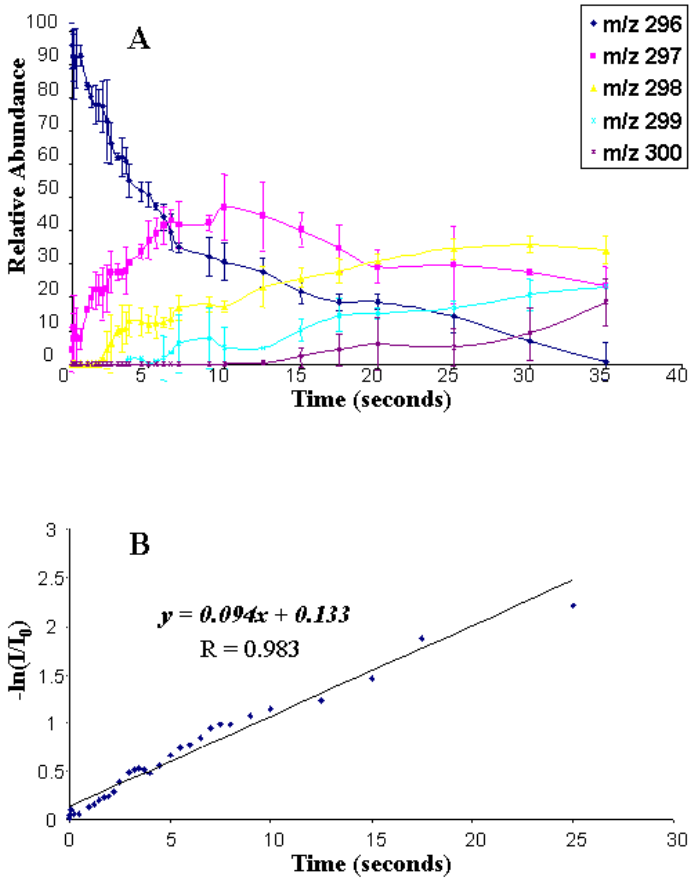

Figure 12. A) Temporal plot of the H/D exchange ion-molecule reaction of GGY $[M+H]^+$ ions with MeOH-d_4, and B) inverse log plot of the first exchange of GGY $[M+H]^+$ ions.

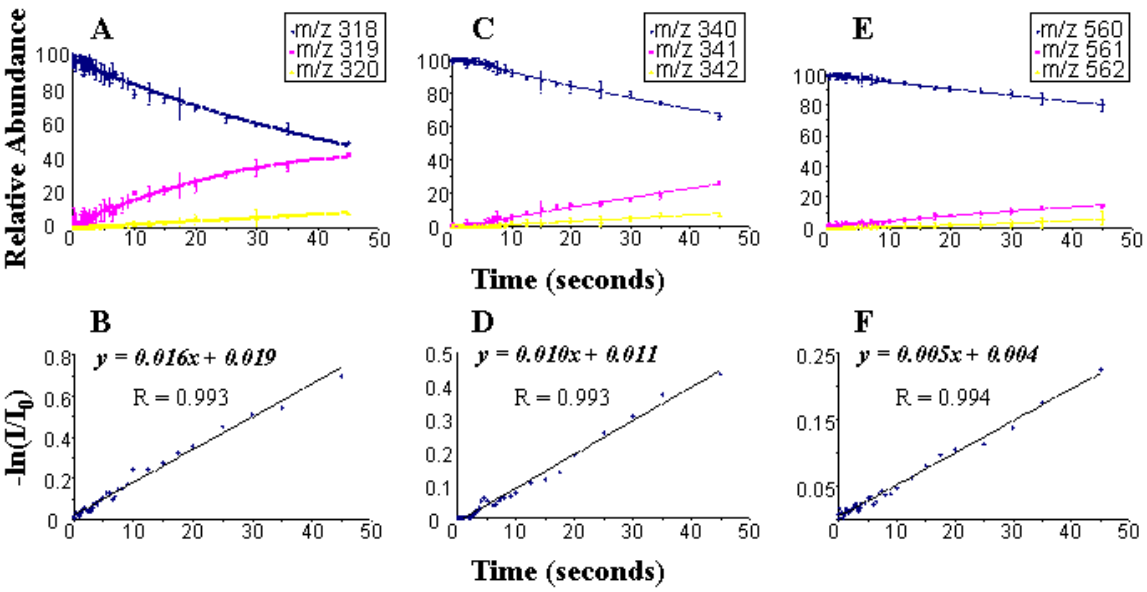

Figure 13. A) Temporal plot of the H/D exchange ion-molecule reaction of GGY $[M+Na]^+$ ions with MeOH-d_4, B) inverse log plot of the first exchange of GGY$[M+Na]^+$ ions, C) Temporal plot of the H/D exchange ion-molecule reaction of GGY $[M+2Na-H]^+$ ions with MeOH-d_4, D) inverse log plot of the first exchange of GGY $[M+2Na-H]^+$ ions, E) Temporal plot of the H/D exchange ion-molecule reaction of GGY $[M+2Cs-H]^+$ ions with MeOH-d_4, and F) inverse log plot of the first exchange of GGY $[M+2Cs-H]^+$ions.

$[GYG + H]^+$ ions exchange up to five hydrogens for deuteriums in 45 seconds, as can be seen in the temporal plot pictured in Figure 14A. The rate plot of the first exchange, shown in Figure 14B, is a straight line with a slope of 0.11. Like GGY, the salt adducted (sodium and cesium) species of GYG exchange both slower and to a lesser extent than does the protonated species of GYG, as can be seen in the temporal plots pictured in Figures 15A, C, and E. The rate plots of the first exchanges of $[GYG+Na]^+$,$[GYG+2Na-H]^+$, and $[GYG+2Cs-H]^+$ ions, shown in Figures 15B, D and F, are straight lines with similar slopes (0.008, 0.006 and 0.006, respectively).

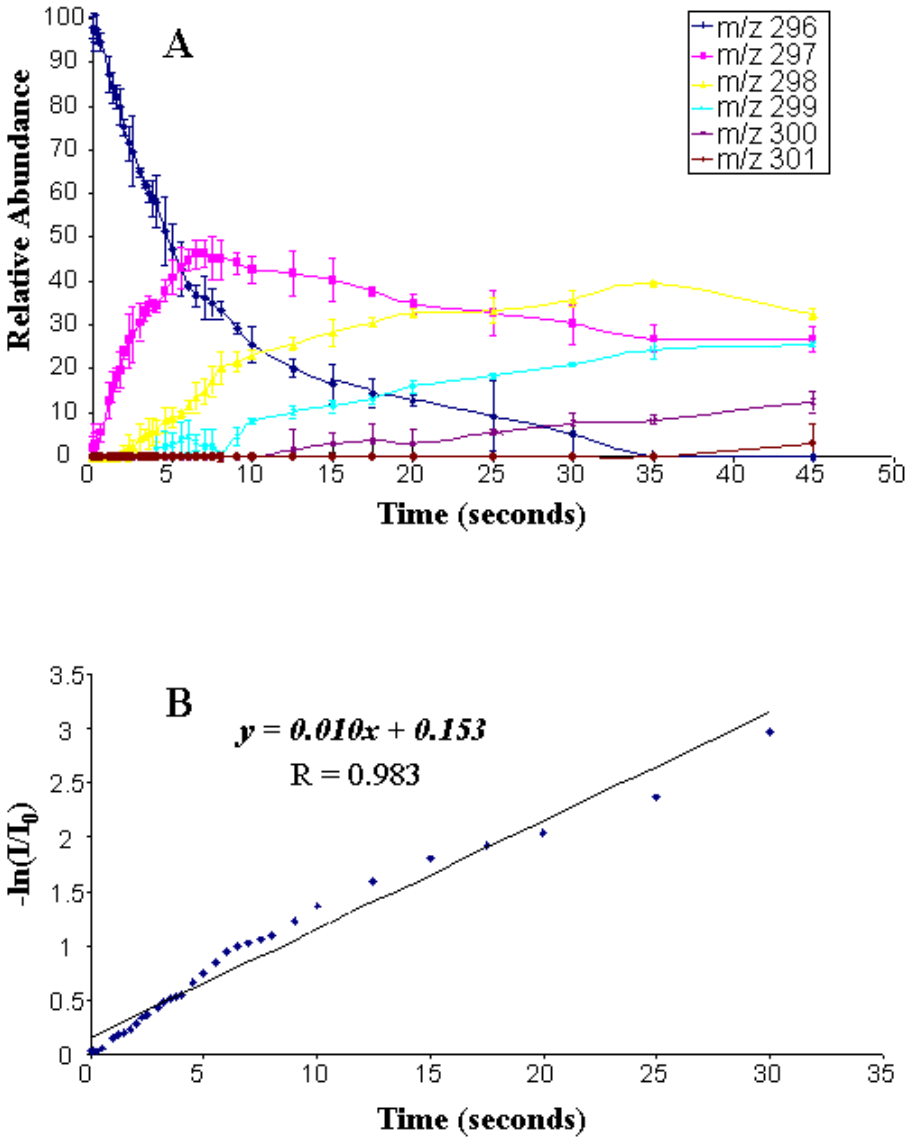

Figure 14. A) Temporal plot of the H/D exchange ion-molecule reaction of GYG $[M+H]^+$ ions with MeOH-d_4, and B) inverse log plot of the first exchange of GYG $[M+H]^+$ ions.

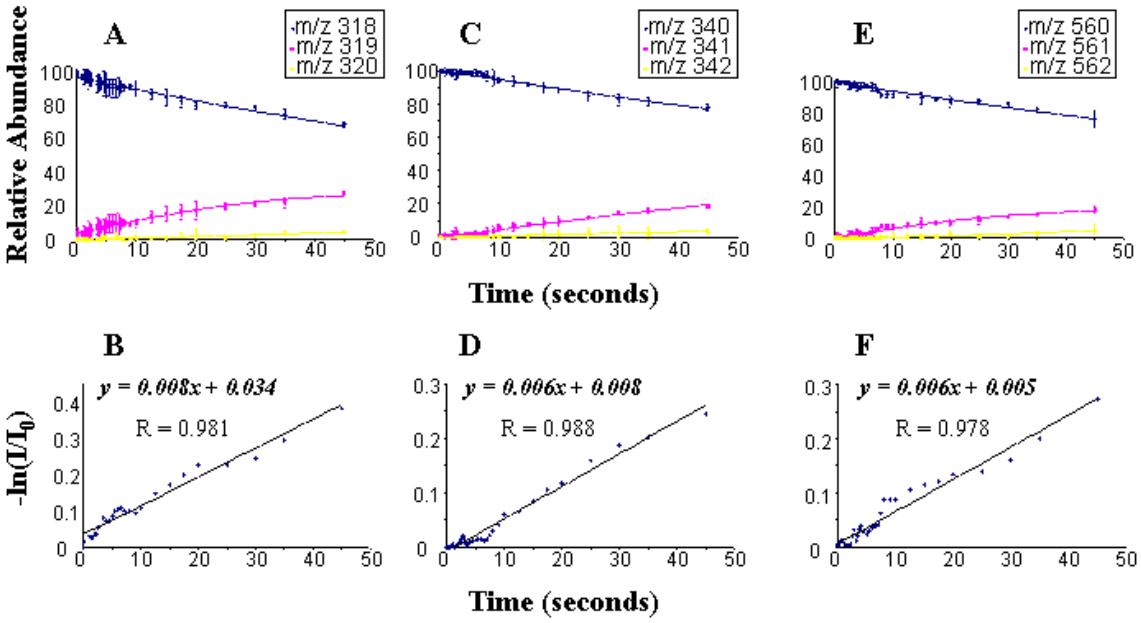

Figure 15. A) Temporal plot of the H/D exchange ion-molecule reaction of GYG [M+H$^+$ ions with MeOH-d_4, B) inverse log plot of the first exchange o f GYG [M+Na]$^+$ ions, C) Temporal plot of the H/D exchange ion-molecule reaction of GYG [M+2Na-H]$^+$ ions with MeOH-d_4, D) inverse log plot of the first exchange of GYG [M+2Na-H]$^+$ ions, E) Temporal plot of the H/D exchange ion-molecule reaction of GYG [M+2Cs-H]$^+$ions with MeOH-d_4, and F) inverse log plot of the first exchange of GYG [M+2Cs-H]$^+$ ions.

[GYG+H]$^+$ ions and [YGG + H]$^+$ ions exhibit similar H/D exchange behavior, as can be seen in the temporal plot shown in Figure 16A. The rate plot of the first exchange, shown in Figure 16B, is a straight line with a slope of 0.12. The salt adducted (sodium and cesium) species of YGG exchange both slower and to a lesser extent than does the protonated species of YGG, as seen in the temporal plots for these species shown in Figures 17A, C and E, respectively. The rate plots of the first exchange, shown in for these species, shown in Figures 17B, D and F, are linear with identical slopes (0.01 for each).

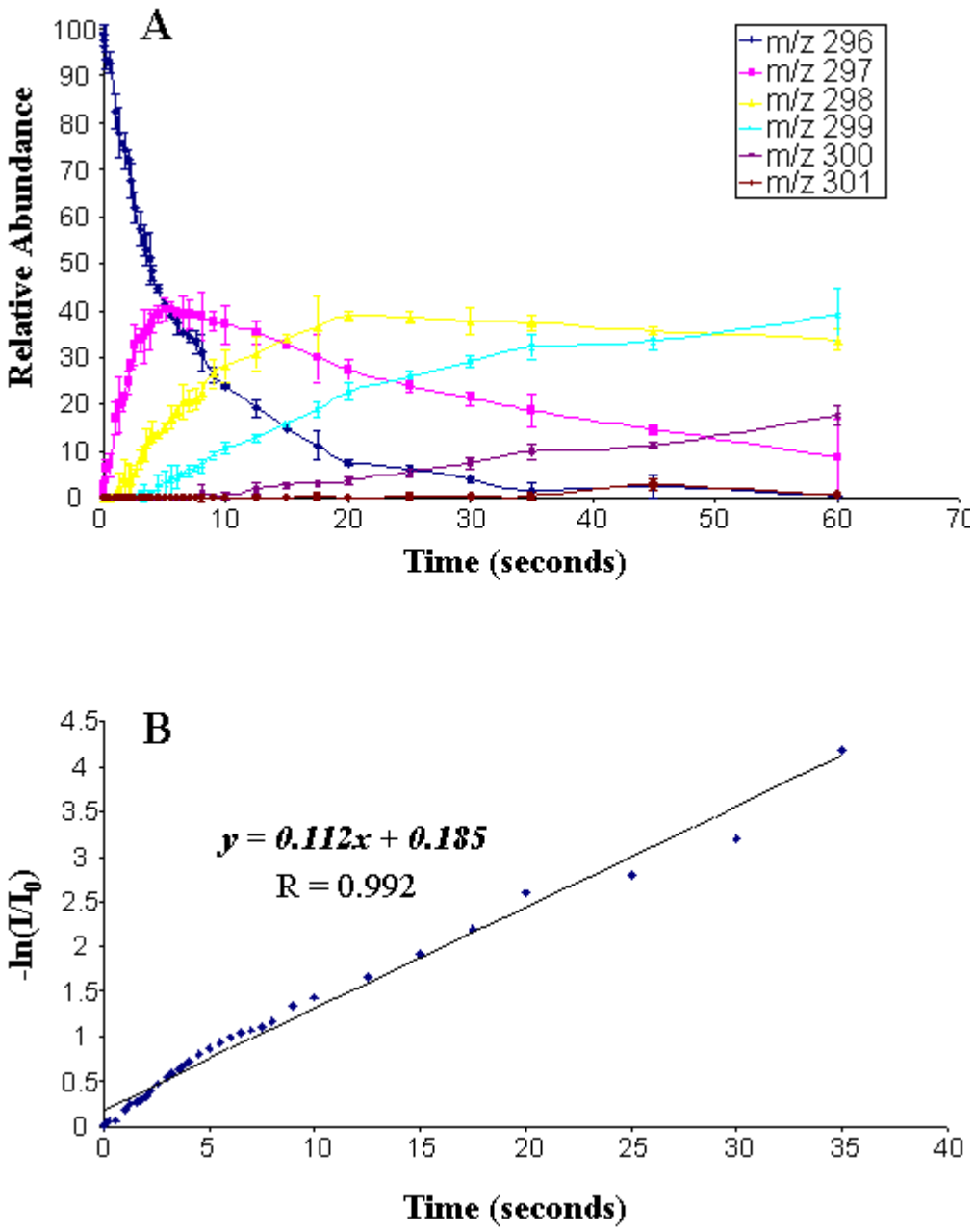

Figure 16. A) Temporal plot of the H/D exchange ion-molecule reaction of YGG $[M+H]^+$ ions with MeOH-d_4, and B) inverse log plot of the first exchange of YGG $[M+H^+$ ions.

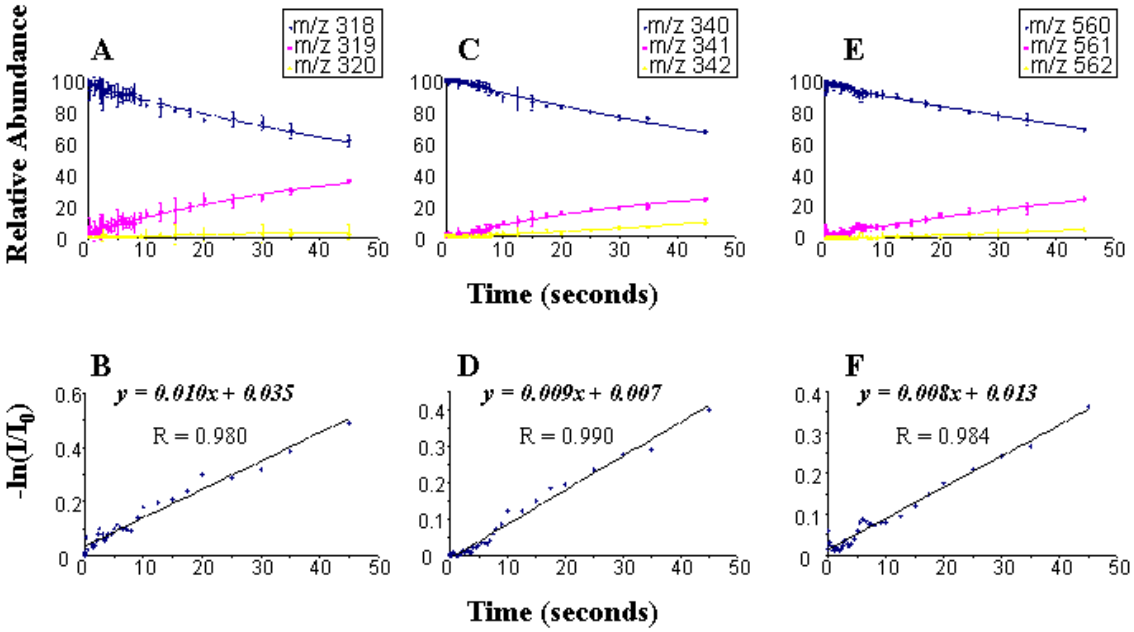

Figure 17. A) Temporal plot of the H/D exchange ion-molecule reaction of YGG $[M+Na]^+$ ions with MeOH-d_4, B) inverse log plot of the first exchange of YGG $[M+Na]^+$ ions, C) Temporal plot of the H/D exchange ion-molecule reaction of YGG $[M+2Na-H]^+$ ions with MeOH-d_4, D) inverse log plot of the first exchange of YGG $[M+2Na-H]^+$ ions, E) Temporal plot of the H/D exchange ion-molecule reaction of YGG $[M+2Cs-H]^+$ ions with MeOH-d_4, and F) inverse log plot of the first exchange of YGG $[M+2Cs-H]^+$ ions.

H/D exchange reactions of singly and doubly sodiated GGY and YGG ions with deuterated methanol were also performed in the analyzer cell of the ICR instrument. In order to obtain sufficient amounts of ions in the analyzer cell, a quadrupolar axialization event was performed prior to transfer from the source cell to the analyzer cell. Ions were trapped in the presence of deuterated methanol for times ranging up to 900 seconds. For $[GGY+Na]^+$ and $[GGY+2Na-H]^+$ ions no difference in the extent of exchange was seen for reactions performed after quadrupolar axialization at reactions times of 360 seconds (see temporal plots in Figures 18A and C, respectively). Additionally exchange reactions performed after quadrupolar axialization occur with much lower rates than to

do exchanges performed without quadrupolar axialization. For example, the slopes of the rates plots for the first exchange of $[GGY+2Na-H]^+$, $[YGG+Na]^+$ and $[YGG+2Na-H]^+$ ions are 0.01 and 0.001 for reactions performed without and with (Figures 18D, 19B and 19C) quadrupolar axialization, respectively. The slopes of the rates plots for the first exchange of $[GGY+Na]^+$ ions are 0.02 and 0.001 for reactions performed without and with (Figure 18B) quadrupolar axialization, respectively.

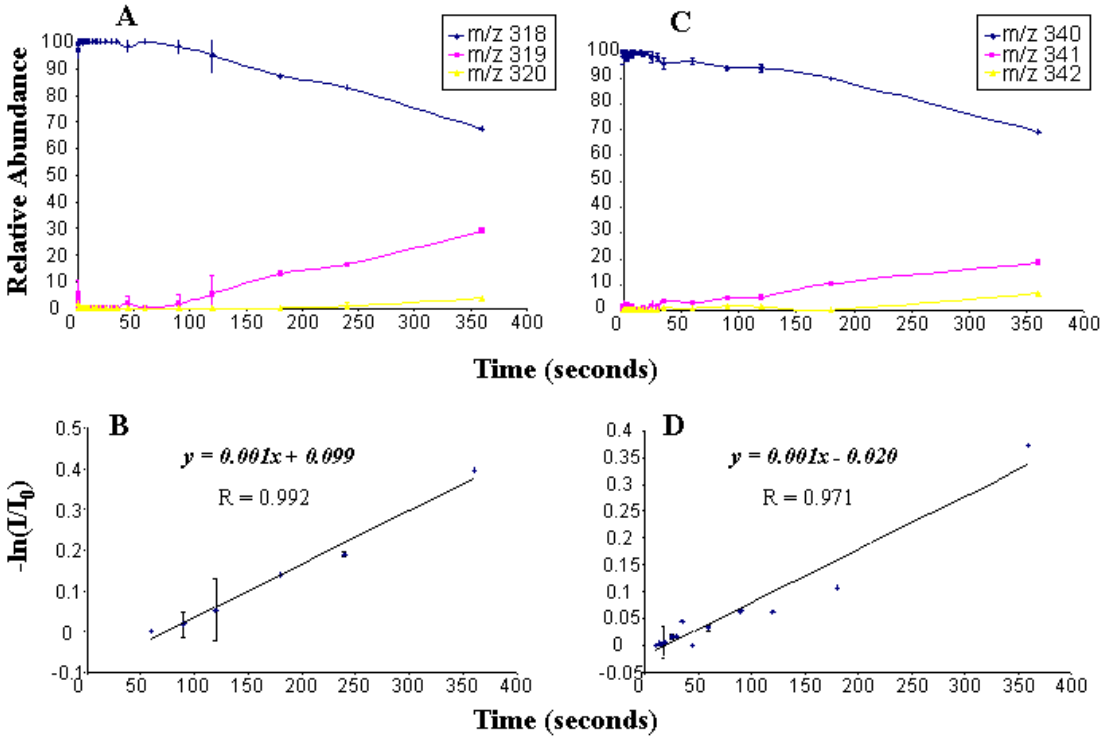

Figure 18. A) Temporal plot of the H/D exchange ion-molecule reaction of GGY $[M+Na]^+$ ions with MeOH-d_4 after a quadrupolar axialization event, B) inverse log plot of the first exchange of GGY $[M+Na]^+$ ions after a quadrupolar axialization event, C) Temporal plot of the H/D exchange ion-molecule reaction of GGY $[M+2Na-H]^+$ ions with MeOH-d_4 after a quadrupolar axialization event, and D) inverse log plot of the first exchange of GGY $[M+2Na-H]^+$ ions after a quadrupolar axialization event.

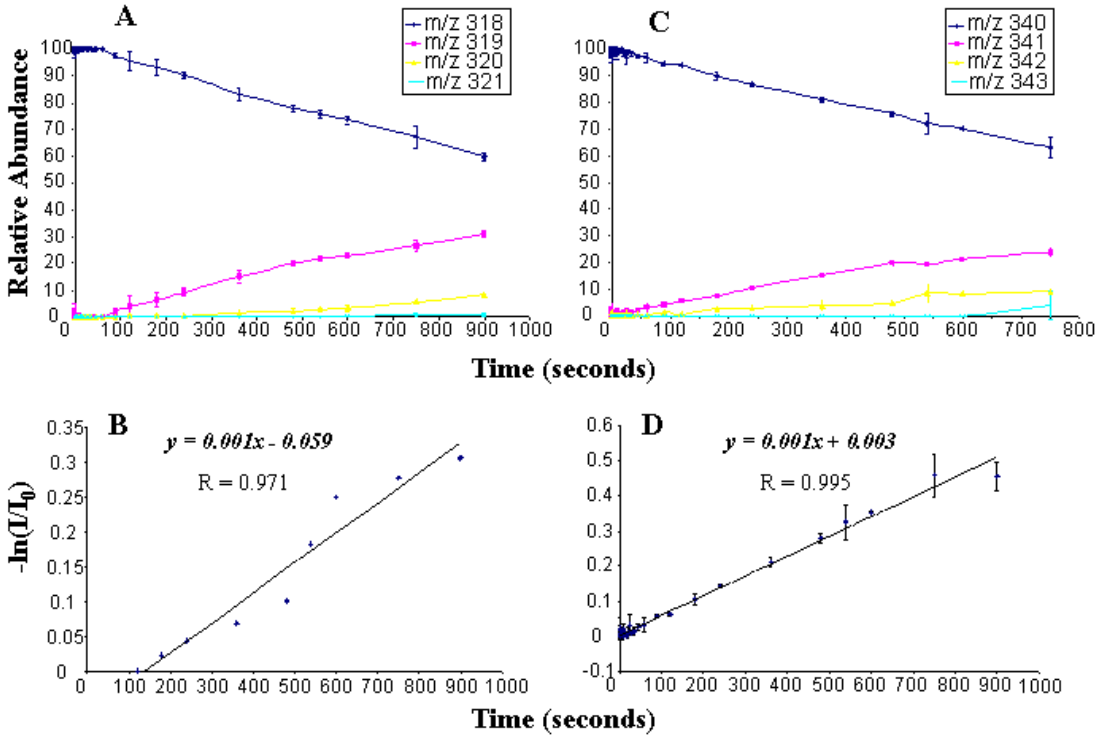

Figure 19. A) Temporal plot of the H/D exchange ion-molecule reaction of YGG $[M+Na]^+$ ions with MeOH-d_4 after a quadrupolar axialization event, B) inverse log plot of the first exchange of YGG $[M+Na]^+$ ions after a quadrupolar axialization event, C) Temporal plot of the H/D exchange ion-molecule reaction of YGG $[M+2Na-H]^+$ ions with MeOH-d_4 after a quadrupolar axialization event, and D) inverse log plot of the first exchange of YGG $[M+2Na-H]^+$ ions after a quadrupolar axialization event.

Molecular modeling, energy calculations and filtering techniques were used to generate and select possible conformations for GGY, GYG and YGG. Simulated annealing was used to generate a population of structures for all species of GGY, GYG and YGG. Each structure was characterized in terms of energy and collision cross-section. One to three hundred low-energy (within 6 kcal/mol of the lowest energy structure) structures were clustered based on structure and intra-molecular interactions. Representative structures were chosen based on agreement between the experimental collision cross-section, cluster population (structures in the most populated cluster within the cross-section range were considered most likely) as well as energy level.

Shown in Figure 20A is the cluster plot of 300 structures of $[GGY+H]^+$ generated by molecular dynamics. Each color in the cluster plot represents a structural group with different intra-molecular interactions. Figure 20A clearly illustrates that group 2 is the most populated group in the cross-section range of interest for the $[GGY+H]^+$ ions (117 –125 $Å^2$).

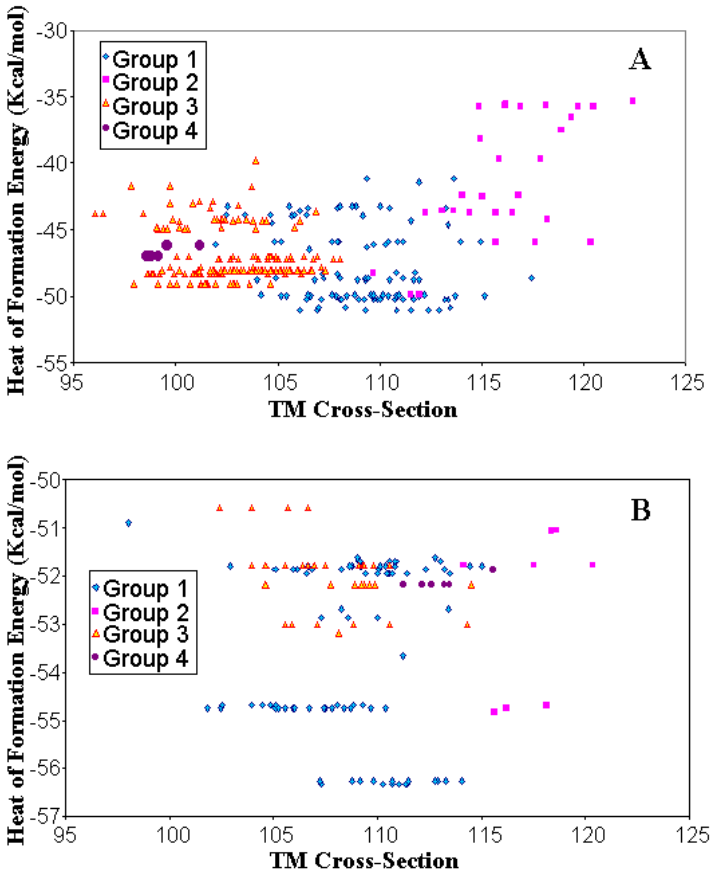

Figure 20. Cluster plots of 300 structures generated by molecular dynamics of A) $[GGY+H]^+$ ions, and B) $[YGG+H]^+$ ions. Each color in the cluster plot represents a structural group with different intra-molecular interactions.

Low-energy structures closely matching the experimentally determined cross-section were compared with the H/D exchange data to select a candidate structure. The

same method was applied to the alkali metal ion adduct species of GGY as well as to all species of GYG and YGG. In some cases, multiple groups were similarly populated in the cross-section range of interest. For example, the cluster plot of $[YGG+H]^+$ structures indicates that both groups 1 and 2 have a similar number of structures in the cross-section range, as can be seen in Figure 20B (the cross-section range is 112-120 $Å^2$). In such a case, low-energy structures closely matching the experimentally determined cross-section from each group are selected and compared to the gas-phase H/D exchange data. By comparing structures from groups 1 and 2 with exchange data, a representative structure from group 2 was chosen.

The proposed structures for protonated GGY as well as for its alkali metal ion adducted species have prominent cation-π interactions present. The proposed structure for $[GGY+H]^+$ ions (Ω_{theo}= 120) is shown in Figure 21A. In this conformation, an amide nitrogen is participating in a cation-π interaction with the tyrosine moiety. Additionally, the protonated N-terminus is involved in a hydrogen bonding interaction with the C-terminus. The alkali metals in the proposed structures for $[GGY+Na]^+$ (Ω_{theo}= 1115) and $[GGY+K]^+$ ions (Ω_{theo}= 118), shown in Figures 21B and 21C, participate in very similar binding. The metal ions are participating in a cation-π interaction with the phenol ring in the tyrosine side chain as well as interacting with the carbonyl oxygens. Cesium is interacting with the tyrosine side chain in a cation-π interaction as well as with the C-terminus in the proposed structure for $[GGY+Cs]^+$ ions (Ω_{theo}= 122), shown in Figure 21D. The proposed structure for the doubly cesiated species of GGY (Ω_{theo}= 137), shown in Figure 21E, is similar to that of the singly adducted species with the second

cesium located at the other end of the molecule interacting with the N-terminus and a carbonyl oxygen. The proposed structure for $[GGY+2Na-H]^+$ (Ω_{theo}= 1115), Figure 21F, indicates that one sodium is participating in a cation-π interaction with the tyrosine residue as well as with the C-terminus, while the other sodium is interacting with the C-terminus and both carbonyl oxygens.

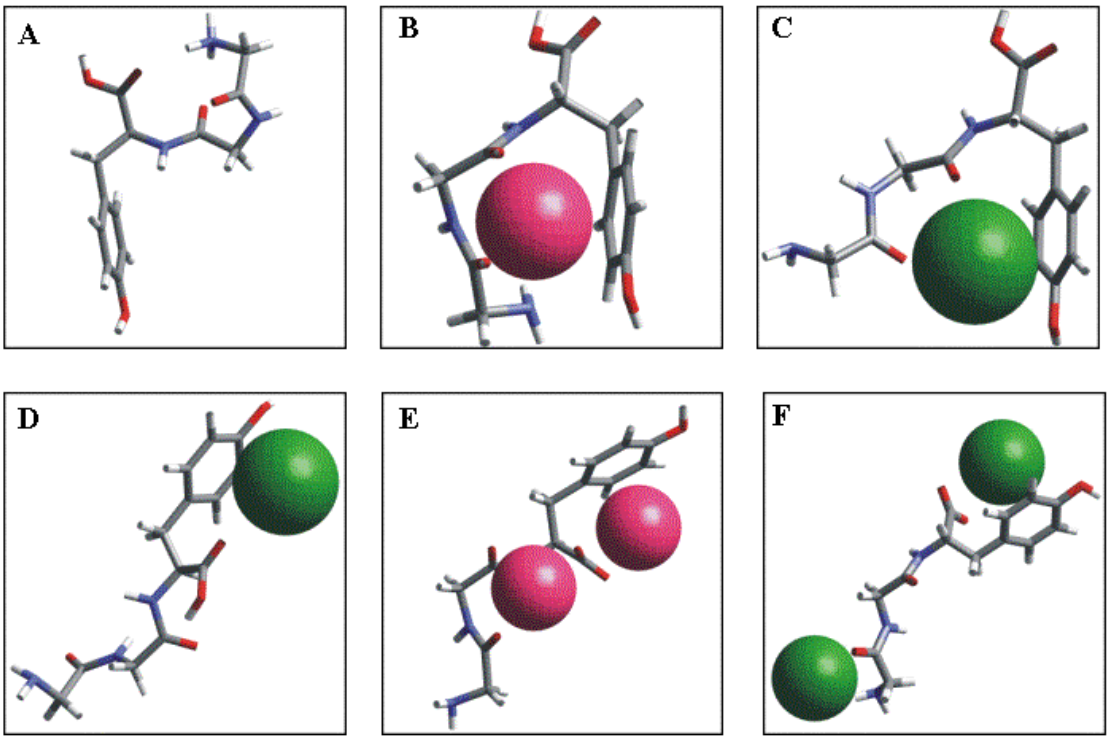

Figure 21. Proposed structures for A) $[GGY+H]^+$, B) $[GGY+Na]^+$, C) $[GGY+K]^+$, D) $[GGY+Cs]^+$, E) $[GGY+2Na-H]^+$, and F) $[GGY+2Cs-H]^+$.

Unlike the proposed structure for $[GGY+H]^+$ ions, the structure proposed for $[GYG+H]^+$ ions (Ω_{theo}= 112) has no cation-π interactions present, as can be seen in Figure 22. Neither the N-terminus nor any backbone amide nitrogens are in close

proximity to the tyrosine side chain. However, in this structure, the charged N-terminus is participating in a hydrogen bonding interaction with the C-terminus as well as with a backbone carbonyl oxygen.

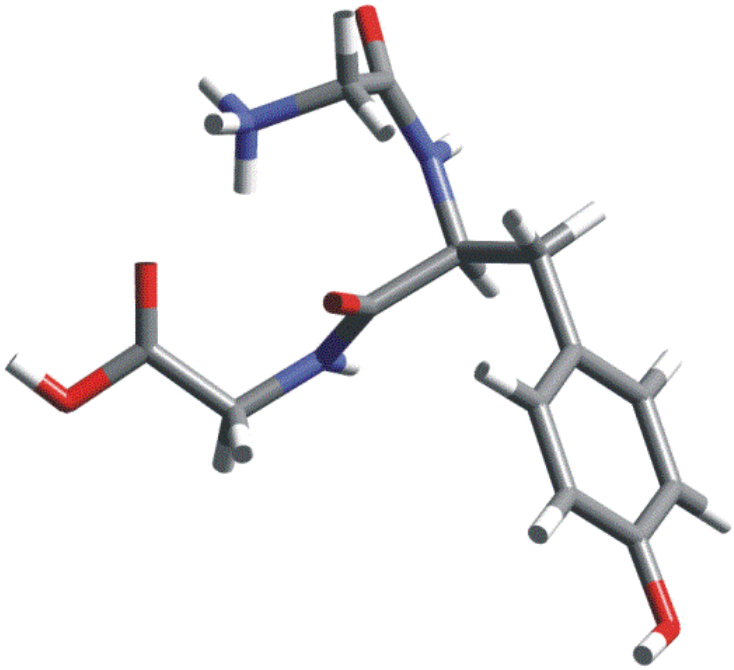

Figure 22. Proposed structure for $[GYG+H]^+$ ions.

While the proposed structures for all species of GGY indicate the presence of cation-π interactions, the proposed structures for protonated YGG and its alkali metal adducted species indicate that absence of such an interaction. In fact, hydrogen bonding interactions are the prominent interactions in the proposed structure for $[YGG+H]^+$ ions (Ω_{theo}= 116). In the proposed conformation of $[YGG+H]^+$ ions, Figure 23A, the N-terminus is interacting with the carbonyl oxygens as well as with the tyrosine side chain.

The alkali metals in the proposed structures for $[YGG+Na]^+$ (Ω_{theo}= 121) and $[YGG+K]^+$ (Ω_{theo}= 123), shown in Figures 23B and 23C, are interacting with the C-terminus as well as with both carbonyl oxygens while the alkali metal in $[YGG+Cs]^+$ ions (Ω_{theo}= 128) is in close proximity to the N-terminus and a carbonyl oxygen, as shown in Figure 23D. The proposed structures for $[YGG+2Na-H]^+$ (Ω_{theo}= 123) and $[YGG+2Cs-H]^+$ ions (Ω_{theo}= 139) are extremely similar and indicate that one alkali metal is interacting with the C-terminus while the second alkali metal is sharing the interaction with the C-terminus as well as interacting with a carbonyl oxygen (see Figures 23E and 23F, respectively).

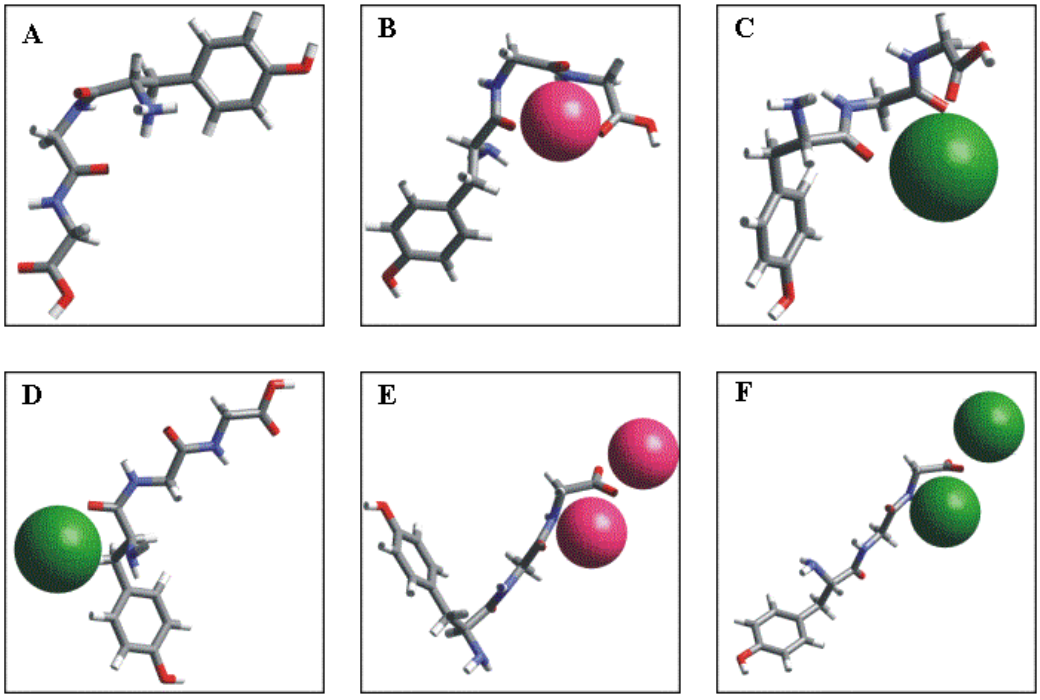

Figure 23. Proposed structures for A) $[YGG+H]^+$, B) $[YGG+Na]^+$, C) $[YGG+K]^+$, D) $[YGG+Cs]^+$, E) $[YGG+2Na-H]^+$, and F) $[YGG+2Cs-H]^+$.

Discussion

The presence of a single peak in the ATD of protonated and cationized species of GGY, GYG and YGG is interpreted to indicate that the $[M+H]^+$ and $[M+Cat]^+$ ions are composed of one conformer, or one population of conformers with similar (≤ 2% difference) cross-sections. The difference in the cross-sections of the $[M+H]^+$ ions of GGY and YGG is interpreted to suggest that the gas-phase structure of the tripeptides is highly dependent on the position of the tyrosine residue (C-terminal or N-terminal) and the IM-MS behavior of the alkali metal adducts of GGY and YGG further supports this interpretation. The sodiated and potassiated adducts of GGY have smaller collision cross-sections than the protonated species, which would result in a deviation from the expected linear relationship between mass and drift time as has been previously observed for alkali metal ion adducts of certain biomolecules.[31, 91]

As observed from gas-phase H/D exchange ion-molecule reactions, protonated GGY ions exchange up to four hydrogens for deuteriums in 45 seconds while $[YGG+H]^+$ ions exchange five. This can be contrasted to the previously observed lack of exchange of leucine enkephalin (contains a N-terminal tyrosine), which was explained in terms of lack of a mobile proton.[96] Therefore it seems likely that the proton is mobile in protonated YGG, GYG and GGY. Exchange of the alkali-adducted species of GGY, GYG and YGG, however, were much slower and to a lesser extent than the protonated species. Behavior similar to this has been previously observed and has been explained in terms of either a change in conformation or lack of a mobile proton upon alkali metal ion adduction.[97, 98] While the proposed structures for protonated GGY differ from those

proposed for the sodiated, doubly sodiated and doubly cesiated species, the proposed structures for protonated, sodiated, doubly sodiated and doubly cesiated YGG are all very similar. Additionally, the proposed structure for sodiated GGY is significantly different from those proposed for doubly sodiated and doubly cesiated GGY, but their exchange behavior is very similar. Therefore, it seems more likely that the difference in exchange behavior between the protonated and alkali metal ion adducted species of GGY and YGG is more accurately described by the mobile proton model explanation rather than a conformational change. Upon alkali metal ion adduction the charge site becomes the cation and to what it is bound. This differs significantly from the charge site in protonated species being a peptide functionality (basic side chain or N-terminus). Because the H/D exchange mechanism for methanol-d_4 is charge directed replacement of a proton with a cation would significantly affect the exchange by hindering formation of the proton bridge intermediate that leads to exchange. Additionally, as Reyzer *et al.* suggest, the presence of an alkali ion in place of a proton makes the other labile hydrogens in the molecule less acidic and therefore less labile.[98] Calculated charge state densities for the protonated and alkali metal ion adducted species of GGY and YGG illustrate that upon alkali metal ion adduction the hydrogens in the molecule have a less positive charge distribution. For example, the N-terminal hydrogens in $[YGG+H]^+$ ions are very acidic, as can bee seen in Figure 24A (blue represents a positive charge density). Upon sodium ion adduction the N-terminal hydrogens become less acidic (less intense blue color) as can be seen in the charge density maps for $[YGG+Na]^+$ and $[YGG+2Na-H]^+$ ions (Figures 24B and 24C, respectively). The charge state densities

support the proposal by Reyzer *et al.* that upon alkali metal ion adduction the labile hydrogens become less acidic, slowing the rate and lessening the extent of H/D exchange.

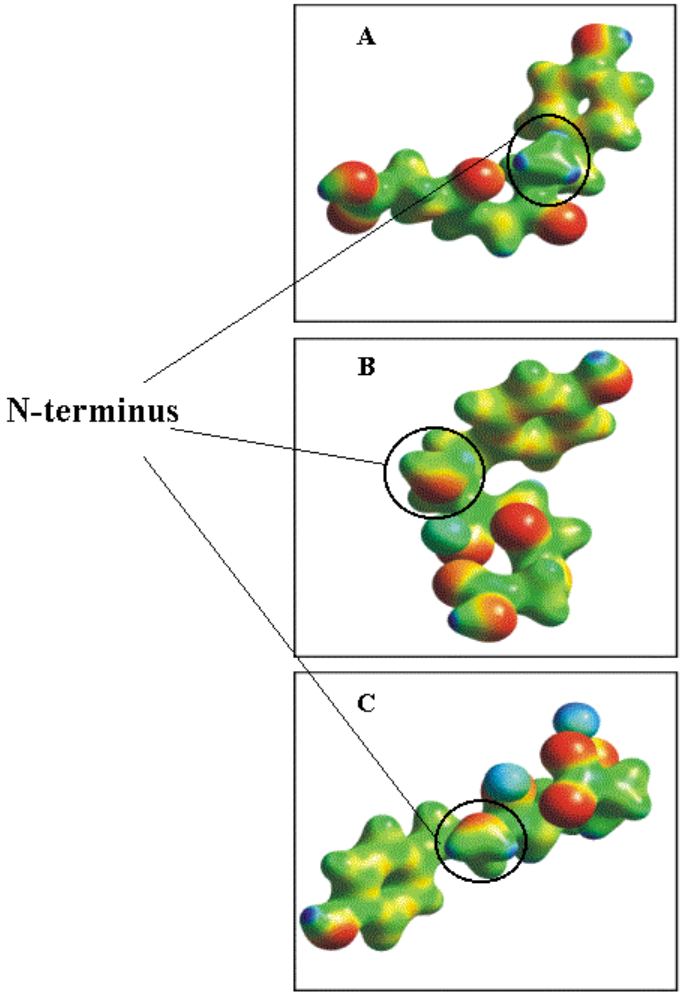

Figure 24. Calculated charge density maps for A) $[YGG+H]^+$ ions, B) $[YGG+Na]^+$ ions, and C) $[YGG+2Na-H]^+$ ions.

The rate plots of the $[M+H]^+$ and $[M+Cat]^+$ ions are straight lines, which is interpreted to indicate the presence of only one rate for the exchange reaction and therefore the presence of only one conformation or a population of conformations with similar ion-neutral accessibilities and reactivities; this is in agreement with the appearance of a single peak in the IM-MS data. The decrease in the H/D exchange reactivity of the $[M+Na]^+$ and $[M+2Na-H]^+$ ions of GGY and YGG upon quadrupolar axialization can be attributed to the heating the ions undergo during a quadrupolar axialization event, which can lead to a destruction of the intra-molecular interactions that contribute to the structure of the ion.[52, 53] Such destruction in the intra-molecular interactions could lead to a more extended conformation, which might be unable to stabilize the methanol-d_4 molecule through hydrogen-bonding. The lack of such stabilization would not allow the long-lived ion-neutral complex necessary for facile H/D exchange, leading to a decrease in reactivity.[42, 45, 98]

In the proposed structures for the protonated and alkali metal ion adducted GGY ions the alkali ion is participating in a cation-π interaction with the tyrosine side chain as well as coordination with the backbone carbonyl oxygens. These results are in agreement with previous CID fragmentation data, where the authors report that alkali metal ions are coordinated to π-systems.[8] Furthermore, in the proposed structure for doubly sodiated GGY one Na^+ is coordinated to the tyrosine side chain and to the C-terminus while the other Na^+ is coordinated to the C-terminus and backbone carbonyl oxygens, which is in agreement with previous reported CID fragmentation data where the authors similarly suggest that in doubly sodiated peptides containing a basic residue, the first Na^+ is

coordinated to a pi systems while the second Na^+ ion is coordinated to the carboxy terminus.[83] Additionally, previous ion mobility data of doubly sodiated bradykinin indicate that the first Na^+ is coordinated to the arginine side chains (cation-π interactions) while the second Na^+ is interacting with the carbonyl oxygens[31], further validating the proposed structure for doubly sodiated GGY. The proposed structures for the protonated and cationized species of GGY (correlated with the IM-MS data presented earlier) are consistent with previous IM and MM results where deviations from the expected mass-mobility trend line for alkali metal ion adducted species are linked to the presence of cation-π interactions in gas-phase structures.[31, 91]

While proposed structures of protonated and alkali adducted GGY have prominent cation-π interactions, the proposed structures for protonated and alkali metal ion adducted YGG illustrate that the alkali metal ion is coordinated to oxygen-containing functionalities (C-terminus and backbone carbonyl oxygens) only. These results are in agreement with previous CID fragmentation data, which indicate that alkali metal ions are coordinated to oxygen-containing moieties.[84-87]

Conclusions

IM-MS, gas-phase H/D exchange and MM were successfully used to probe the intra-molecular interactions present in both the protonated and alkali adducted species of GGY and YGG. It was observed by IM-MS that the conformation of a model tripeptide is highly dependent on the position of the tyrosine moiety (C-terminal or N-terminal). IM-MS experiments show that the Na^+ and K^+ adducted species of GGY have smaller collision cross-sections than the protonated species. However, the alkali-adducted

species (Na^+, K^+, and Cs^+) of YGG ions all have larger collision cross-sections than the protonated species. Structures generated by molecular modeling illustrate that cation-π interactions are prevalent in the protonated and alkali metal ion adducted species of GGY whereas other intra-molecular interactions (primarily interactions between the cation and oxygen-containing groups) dominate the structures proposed for YGG. These results are interpreted to suggest that the presence of the tyrosine moiety on the N-terminus prohibits cation-π interactions in the protonated as well as cationized forms whereas the presence of the tyrosine on the C-terminus promotes cation-π interactions between an amide nitrogen in the protonated species as well as between the cations in the sodiated, potassiated and cesiated forms.

Additionally, it was observed with gas-phase H/D ion-molecule reaction experiments that replacing the proton with a cation significantly slows the rate and lowers the extent of exchange. These results are due to the presence of a cation as the charge site resulting in lowering the acidity of the other labile hydrogens in the molecule. Therefore, exchange might not be indicative of conformational changes but more indicative of a change in the nature of the charge site.

Overall, results presented in this chapter demonstrate that the cation-π interaction can be a dominant non-covalent force that highly contributes to gas-phase peptide ion conformation, and is a force that can be competitive with traditional intra-molecular interactions (*i.e.*, hydrogen bonding, van der Waals interactions and hydrophobic forces). The presence of cation-π interactions also seems to be highly dependent on the primary structure of the peptides, particularly on the position of the π-system.

CHAPTER V

INVESTIGATION OF THE EFFECT OF SALT ADDUCTION ON GAS-PHASE STRUCTURE USING ION MOBILITY-MASS SPECTROMETRY AND H/D EXCHANGE MASS SPECTROMETRY: A DETAILED STUDY OF BRADYKININ ANALOGUES

Introduction

Bradykinin is a nine-residue peptide (ArgProProGlyPheSerProPheArg) hormone found in human blood and urine.[99] It is known to participate in the widening of arteries to increase blood flow and is also connected to algesic activities. Bradykinin and analogs of bradykinin are excellent test cases to critically evaluate IM-MS and H/D exchange as structural probes because they have been extensively studied in the both the solution and gas phase.

For example, CD and NMR experiments indicate that 90% dioxane induces hydrogen bonding in bradykinin and that bradykinin exists in a more highly ordered configuration in hydrophobic environments[100], whereas the major hydrogen bonding interactions present in aqueous solutions are those between the peptide and the solvent.[101] Additionally, a β-turn interaction was found to be present in bradykinin fragments 1-4 and 1-5 when in organic solvent systems[99, 100, 102,], but no β-turn interactions were detected for bradykinin in aqueous solutions.[103] However, in aqueous solvent conditions it was observed that the side chain of the first arginine is in a strongly asymmetric environment, possibly that of the aromatic ring of the phenyalanine residue

in the fifth position.[103] A β-turn interaction was also found to be present in residues 6-9 when bradykinin is in SDS.[104]

The solution-phase H/D exchange behavior of bradykinin as a function of its solvent system has also been studied.[4] It was observed that the isotopic peak distribution of bradykinin shifts to higher masses as D_2O is added to organic solvent systems. We suggested that bradykinin has a more compact conformation in organic solvents than in aqueous solvents, making the peptide less accessible to the deuterated solvent, resulting in smaller amounts H/D exchange.

Additionally, the gas-phase structures of $[M+H]^+$ ions of bradykinin and its analogues have been extensively studied. It has been proposed that intra-molecular hydrogen bonds exist between the N- and C-terminal arginine residues as well as between the serine side chain and the protonated guanidine group by Gimon-Kinsel *et al.*,[5] whereas Neumann *et al.*, suggested that the protonated guanidine group of bradykinin interacts with Pro^3 or Phe^5.[105] Gas-phase H/D exchange and blackbody infrared dissociation (BIRD) of bradykinin and derivatives of bradykinin indicate that the $[M+H]^+$ ion of bradykinin might exist as a zwitterion.[6, 27] However, hydroiodic attachment studies suggest that the $[M+H]^+$ ion does not exist as a zwitterion due to its ability to attach two HI molecules.[106] Ion mobility experiments demonstrate that the drift-time distribution of bradykinin is slightly larger than that calculated for an ion of a single conformation, suggesting that gas-phase bradykinin $[M+H]^+$ ions are composed of multiple interconverting conformers having a range of collision cross-sections that differ by as much as ±2%.[31]

Alkali metal ion adduction to bradykinin has also been studied in the gas phase. Bowers and coworkers observed alkali ion adducts of bradykinin to deviate from the expected linear relationship observed in ion mobility; it was observed that the collision cross-sections of the sodium adducts of bradykinin were very similar to those of protonated bradykinin ions.[31] These deviations were rationalized in terms of conformational change to the peptide upon alkali metal ion adduction.[89] Cerda *et al.*, concluded from post-source decay data that sodium ions anchor to the N-terminal portion of bradykinin and its des-arg analogues, which would result in significant changes to the structure.[87]

Although, the structure of gas-phase bradykinin $[M+H]^+$ and $[M+Cat]^+$ (where Cat is an alkali metal ion) ions has been extensively studied, much can still be learned regarding its gas-phase structure. In order to characterize the NMR spectrum of bradykinin, London *et al.*, studied the NMR spectra of its fragments.[101] A similar approach could prove to be beneficial to the study of the gas-phase structure(s) of bradykinin, as well. In this chapter, the protonated and alkali metal ion adducted (Na^+, K^+ and Cs^+) species of bradykinin (BK) and bradykinin fragments 1-5 (BK1-5), 1-6 (BK1-6), 1-7 (BK1-7), 1-8 (BK1-8), 2-7 (BK2-7), 5-9 (BK5-9) and 2-9 (BK2-9) are studied using ion mobility-mass spectrometry (IM-MS). Gas-phase hydrogen/deuterium (H/D) ion-molecule reactions and molecular modeling are used to further probe the fine structure detail of these molecules.

Experimental and Computational Methods

Ion mobility measurements were made using a matrix-assisted laser desorption-ionization (MALDI)-ion mobility-reflectron-time-of-flight (TOF) mass spectrometer described previously (see Chapter II). Briefly, ions formed by MALDI drift through the ion mobility (IM) cell where they are separated on the basis of collision cross-section (Ω). Threshold laser powers (attenuated with a neutral density filter) were used to collect the arrival time distributions (ATD) for bradykinin and its fragments. IM field strengths ranging from 20 to 30 volts/cm·torr were used to acquire ATDs of BK and its fragments. Both the laser power and the field strength were observed to have an effect on the resolution of the ATDs. High laser powers resulted in a broadening of the ATD for all species and at high field strengths the resolution between the multiple conformations observed in the ATD of BK1-5, BK1-6 and BK1-7 $[M+H]^+$ and $[M+Cat]^+$ (where Cat is an alkali metal ion) ions disappeared. We interpret this to signify that at high laser powers and field strengths the ion population sampled by IM-MS is no longer thermal; the ions have internal energy, allowing interconversion between conformers to occur. The collision cross-sections reported herein were obtained using an internal calibration method.[40] Briefly, a peptide with a known cross-section is used as a standard (bradykinin, 245Å^2) and the difference between the drift times of the standard and the ion of interest is measured multiple times and is used to calculate the Ω of the ion of interest relative to the standard. The arrival time distributions (ATDs) presented in this paper are acquired by selecting a narrow mass range from the two-dimensional (mass spectrum and mobility spectrum) data and looking at it in one-dimension (mobility

spectrum). The ATDs of BK and bradykinin fragment $[M+H]^+$ and $[M+Cat]^+$ (where Cat is an alkali metal ion) ions were deconvoluted using a gaussian curve-fit equation with Origin graphing software (OriginLab Corporation). Both a single and multiple gaussian curves were used in the equations to determine the best fit of the ATDs. Because the fit will continue to improve by increasing the number of gaussian curves used, the best fit would be the number of gaussian curves, N, that most improved the fit over N-1 gaussian curves and resulted in little to no improvement in the fit of N+1 gaussian curves. For BK1-7 $[M+H]^+$, BK1-7$[M+Na]^+$, BK1-7$[M+K]^+$, BK1-7 $[M+Cs]^+$, BK5-9 $[M+H]^+$, BK5-9 $[M+K]^+$, BK2-7 $[M+Na]^+$, BK2-9 $[M+H]^+$, BK2-9 $[M+Na]^+$, BK2-9 $[M+K]^+$, BK1-8 $[M+K]^+$, BK1-8 $[M+Cs]^+$ and BK $[M+K]^+$ ions deconvolution of the ATDs yielded gaussian curves which corresponded to collision cross-section values that were not readily apparent/calculated by a cursory examination of the ATD. In all cases, molecular modeling and cluster analysis determined that best-fit structures corresponding to the additional cross-section values were extremely similar to best-fit structures corresponding to the cross-section values found in Table 5.

Gas-phase H/D exchange ion-molecule reactions were carried out using a 3 tesla Fourier transform (FT) ion cyclotron resonance (ICR) mass spectrometer described previously (see Chapter II). Ions were formed by MALDI using a ND:YAG laser operated at 355nm. The ions were formed and trapped in the source region of a two-section cylindrical (4.0cm X 4.0cm) cell. To facilitate H/D exchange, ions were trapped in the presence of ND_3 acid for times ranging from 0.005 to 360 seconds. Pseudo-first order kinetics were obtained by operating at deuterated gas pressures of $6x10^{-8}$ torr.

Temporal plots were generated by plotting ion intensity, corrected for the natural isotope abundance, versus time.

All molecular dynamics calculations were performed with the Cerius (Accelrys) suite of programs using the consistent forcefield (CFF1.01). Model structures for the peptide ions were generated using a simulated annealing cycle[72, 73] where the structure was heated from 300 Kelvin (K) to 1000 K in steps of 50 K with relaxation times of 0.1 picoseconds (ps), making the entire simulation time 280 ps for 100 cycles. The charge solvation forms of ions were modeled for all species. The zwitterionic forms of ions were modeled only for bradykinin and its alkali adducted species. Due to the high energies of the zwitterionic species of the fragments of bradykinin, most likely due to the presence of only one arginine, the zwitterionic structures were not modeled for the fragments of bradykinin. Semi-empirical calculations using AM1 parameters were used to determine the energy of each structure. The collision cross-sections of each structure were calculated using the projection approximation, the exact hard sphere scattering method and the trajectory method using a program designed by Mesleh, *et al*.[69,70] Structures were clustered based on AM1 energies, calculated cross-sections and intra-molecular interactions. Representative structures were chosen based on agreement between the experimental collision cross-section, cluster population (structures in the most populated cluster within the cross-section range were considered most likely) as well as energy level. All proposed structures presented in this chapter have collision cross-section values within 2% of the experimentally calculated values shown in Table 5.

Peptides were purchased from Sigma Aldrich and SynPep and used without further purification. 2', 4', 6'-Trihydroxyacetophenone monohydrate, KCl, CsCl and D(-)fructose were purchased from Sigma Aldrich and used without further purification. Alpha-cyano-4 hydroxycinnamic acid was purchased from Sigma Aldrich and was recrystalized prior to use. ND_3 gas was purchased from Bachem and used without filtering. HPLC grade methanol and deionized (Milli-Q Water System, Millipore) water were used for all experiments. The solutions for IM-MS measurements were prepared by dried droplet using α-cyano-4 hydroxycinnamic acid as matrix with a matrix-to-analyte molar ratio of 400:1. Solutions for the H/D exchange reactions were prepared by dried droplet using 2', 4', 6'-trihydroxyacetophenone monohydrate as matrix and D(-)fructose as a matrix additive with a matrix:additive:analyte molar ratio of 1000:500:1. D(-)fructose has been previously been observed to reduce the internal energies of the ions resulting in enhanced ionization and less fragmentation[94] and it was for this reason that D(-)fructose was added to the MALDI sample preparation for the H/D exchange ion-molecule reactions presented in this paper. For IM-MS and H/D exchange experiments on the K^+ and Cs^+ alkali metal ion adducts, approximately 1 μL of KCl or CsCl was added to the MALDI sample preparation.

Results

The arrival time distributions (ATDs) and cross-sections of the protonated and alkali metal ion (Na^+, K^+ and Cs^+) adducted species of BK and BK1-5, BK1-6, BK1-7, BK1-8, BK2-7, BK5-9 and BK2-9 were measured. Calculated cross-sections for the protonated and alkali metal ion adducted species are listed in Table 5. The difference

between the calculated cross-sections of the alkali metal ion adducted species and those of the protonated species are about 4% for all bradykinin fragments, resulting in a deviation from the expected peptide trend-line observed in IM-MS experiments (Figure 25).[107] In most cases, the alkali-adducted species are larger than the protonated species; however, the $[M+Na]^+$ ions of BK1-5 and BK, the $[M+Cs]^+$ ions of BK-7, and all the alkali metal ion adducts of BK5-9 have collision cross-sections that are smaller than that of the $[M+H]^+$ ions. For cases of multiple conformations the cross-sections values are compared to the species nearest in value.

Table 5. Experimentally calculated collision cross-sections of protonated and alkali metal ion adducted species of bradykinin and bradykinin fragments 1-5, 1-6, 1-7, 1-8, 2-7, 5-9, and 2-9.

Species	Cross-Section	Species	Cross-Section
$[BK1\text{-}5+H]^+$ A	163 (4)	$[BK1\text{-}8+H]^+$	219 (3)
$[BK1\text{-}5+H]^+$ B	168 (5)	$[BK1\text{-}8+Na]^+$	228 (2)
$[BK1\text{-}5+Na]^+$ A	165 (3)	$[BK1\text{-}8+K]^+$	222 (2)
$[BK1\text{-}5+Na]^+$ B	167 (2)	$[BK1\text{-}8+Cs]^+$	222 (4)
$[BK1\text{-}5+K]^+$ A	165 (3)	$[BK2\text{-}7+H]^+$	167 (3)
$[BK1\text{-}5+K]^+$ B	170 (3)	$[BK2\text{-}7+Na]^+$	170 (3)
$[BK1\text{-}5+Cs]^+$ A	166 (3)	$[BK2\text{-}7+K]^+$	169 (2)
$[BK1\text{-}5+Cs]^+$ B	170 (3)	$[BK2\text{-}7+Cs]^+$	170 (2)
$[BK1\text{-}6+H]^+$ A	178 (2)	$[BK5\text{-}9+H]^+$	178 (3)
$[BK1\text{-}6+H]^+$ B	184 (2)	$[BK5\text{-}9+Na]^+$	177 (3)
$[BK1\text{-}6+Na]^+$ A	181 (3)	$[BK5\text{-}9+K]^+$	176 (2)
$[BK1\text{-}6+Na]^+$ B	187 (4)	$[BK5\text{-}9+Cs]^+$	178 (2)
$[BK1\text{-}6+K]^+$ A	183 (2)	$[BK2\text{-}9+H]^+$	221 (3)
$[BK1\text{-}6+K]^+$ B	188 (3)	$[BK2\text{-}9+Na]^+$	224 (3)
$[BK1\text{-}6+Cs]^+$ A	181 (3)	$[BK2\text{-}9+K]^+$	226 (3)
$[BK1\text{-}6+Cs]^+$ B	191 (3)	$[BK2\text{-}9+Cs]^+$	229 (3)
$[BK1\text{-}7+H]^+$	194 (5)	*$[BK+H]^+$*	*245*
$[BK1\text{-}7+Na]^+$	194 (3)	$[BK+Na]^+$	238 (4)
$[BK1\text{-}7+K]^+$	197 (4)	$[BK+K]^+$	245 (2)
$[BK1\text{-}7+Cs]^+$ A	191 (4)	$[BK+Cs]^+$	253(3)
$[BK1\text{-}7+Cs]^+$ B	201 (5)		

Values in parenthesis are errors.

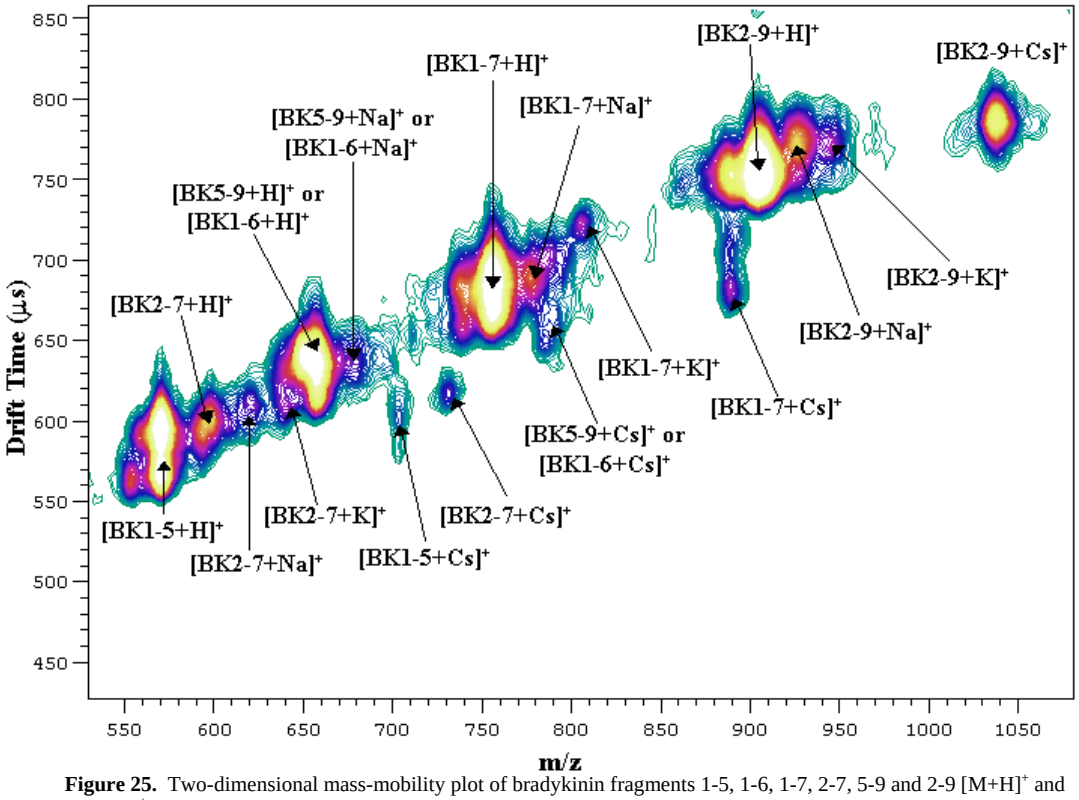

Figure 25. Two-dimensional mass-mobility plot of bradykinin fragments 1-5, 1-6, 1-7, 2-7, 5-9 and 2-9 $[M+H]^+$ and $[M+Cat]^+$ (where Cat is an alkali metal ion) ions.

The ATDs of the $[M+H]^+$ and $[M+Cat]^+$ ions of BK1-5 (Figure 26A) and BK1-6 (Figure 26B) all have multiple peak features. The ATD of BK1-7 $[M+H]^+$ ions (Figure 26C) shows a single broadened peak with a shoulder. Additionally the $[M+Cat]^+$ ions BK1-7 exhibit two peak features in their ATDs (Figure 26C). Furthermore, the resolution between the multiple peak features observed in the ATDs of protonated and cesiated BK1-6 and BK1-7 increases upon cesium ion adduction. The separation between the peak maxima in the ATD of BK1-6 $[M+H]^+$ ions is 25 µs whereas the difference for BK1-6 $[M+Cs]^+$ ions is 37.5 µs. Similarly, two peaks are resolved in the

ATD for BK1-7 $[M+Cs]^+$ ions, whereas for the $[M+H]^+$ ions the ATD is dominated by single peak with a small shoulder.

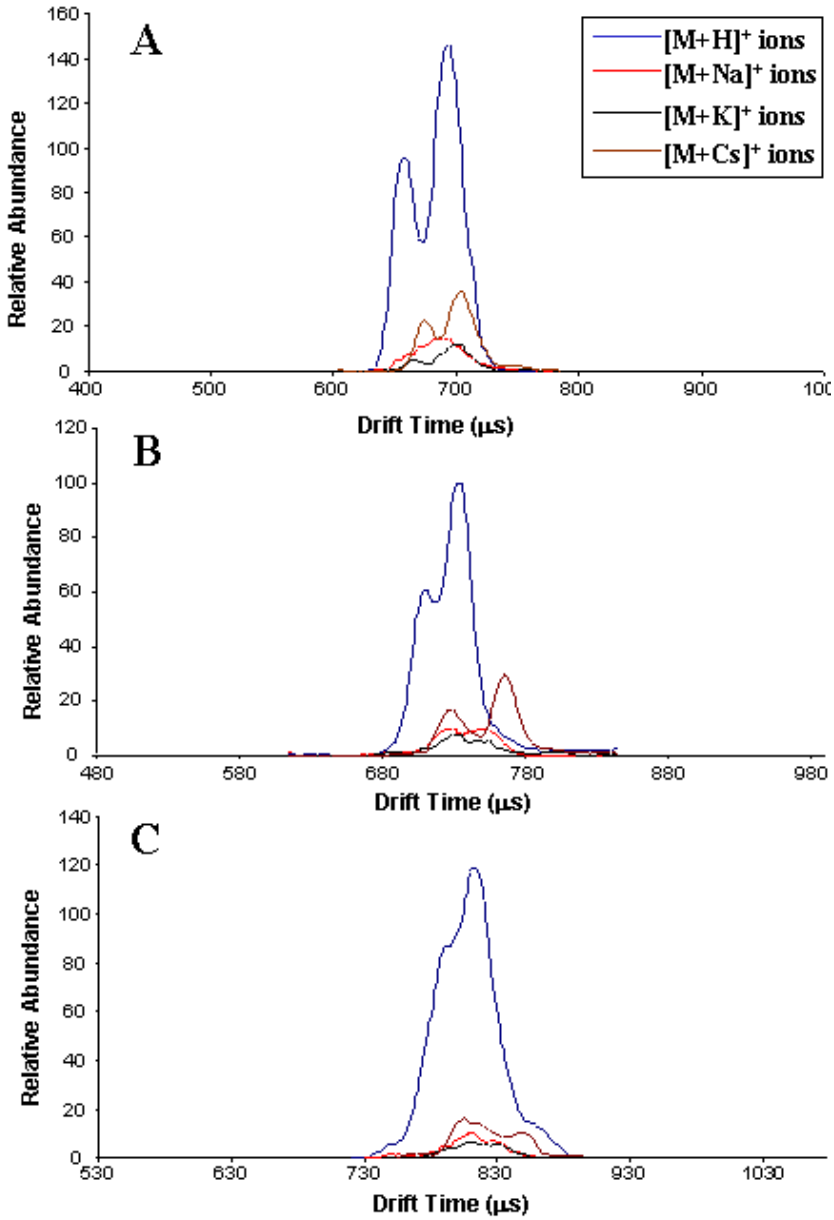

Figure 26. Arrival time distributions of $[M+H]^+$, $[M+Na]^+$, $[M+K]^+$, and $[M+Cs]^+$ ions of A) bradykinin fragment 1-5, B) bradykinin fragment 1-6, and C) bradykinin fragment 1-7.

The ATDs of the $[M+H]^+$ and $[M+Cat]^+$ ions of BK1-5 (Figure 27), BK1-6 (Figure 28), and BK1-7 (Figure 29) were deconvoluted using a gaussian curve-fit equation. The ATDs of the $[M+H]^+$ ions of BK1-5 (Figure 27A), BK1-6 (Figure 28A) and BK1-7 (Figure 29A) were best fit with two gaussian curves. Additionally the ATDs of the alkali metal ion adducted species of BK1-5 (Figure 27B-D) and BK1-6 (Figure 28B-D) were best fit with two gaussian curves, while the alkali metal ion adducted species of BK1-7 (Figure 29B-D) were best fit with three gaussian curves.

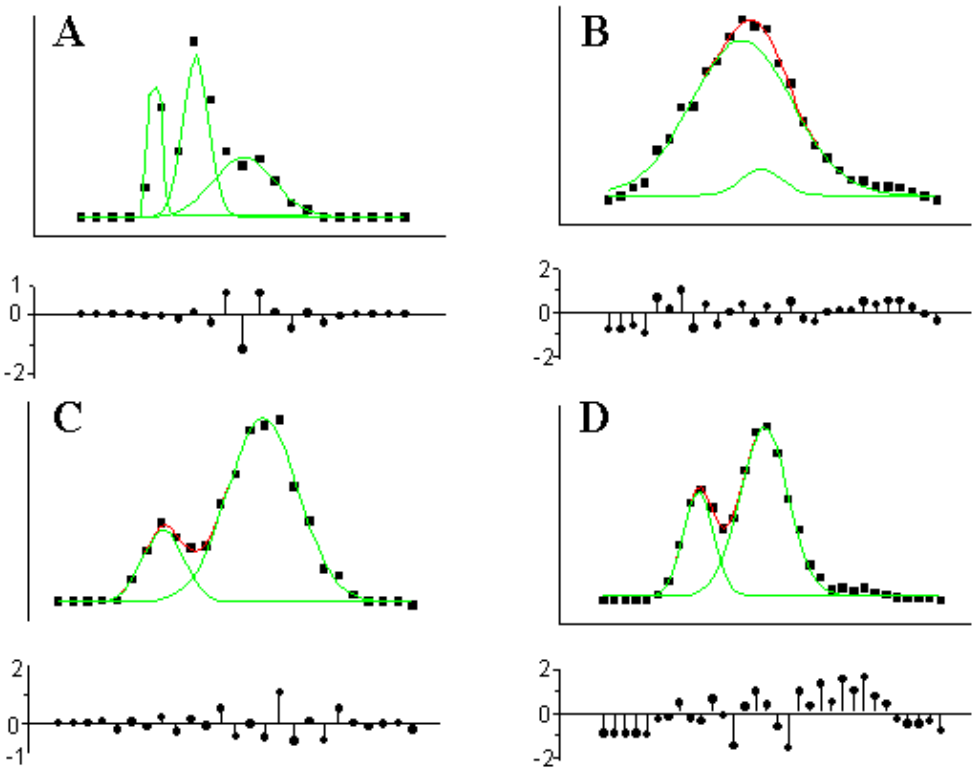

Figure 27. Fits and residuals of the ATD of bradykinin fragment 1-5 A) $[M+H]^+$ ions, B) $[M+Na]^+$ ions, C) $[M+K]^+$ ions, and D) $[M+Cs]^+$ ions.

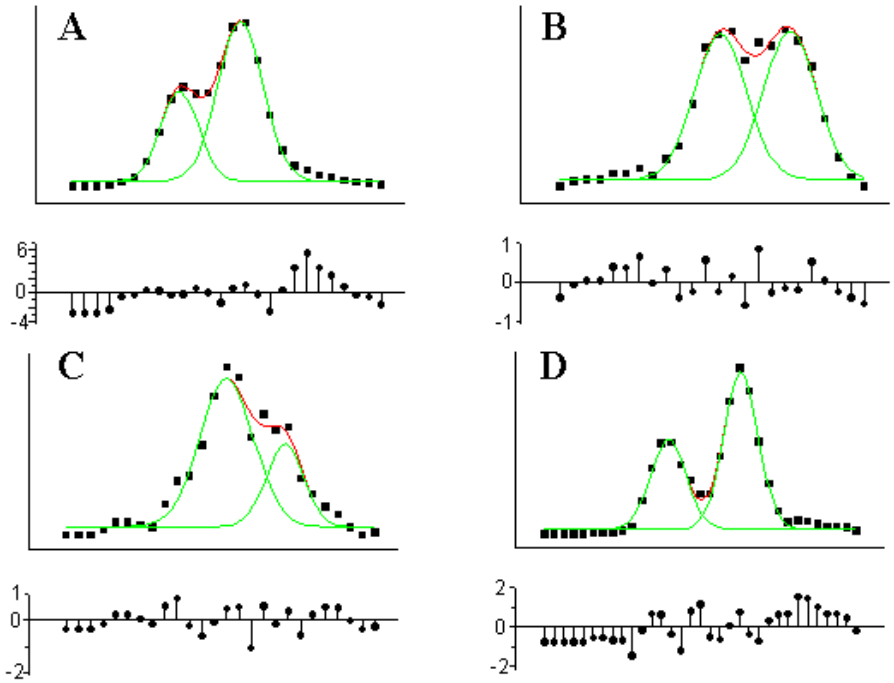

Figure 28. Fits and residuals of the ATD of bradykinin fragment 1-6 A) $[M+H]^+$ ions, B) $[M+Na]^+$ ions, C) $[M+K]^+$ ions, and D) $[M+Cs]^+$ ions.

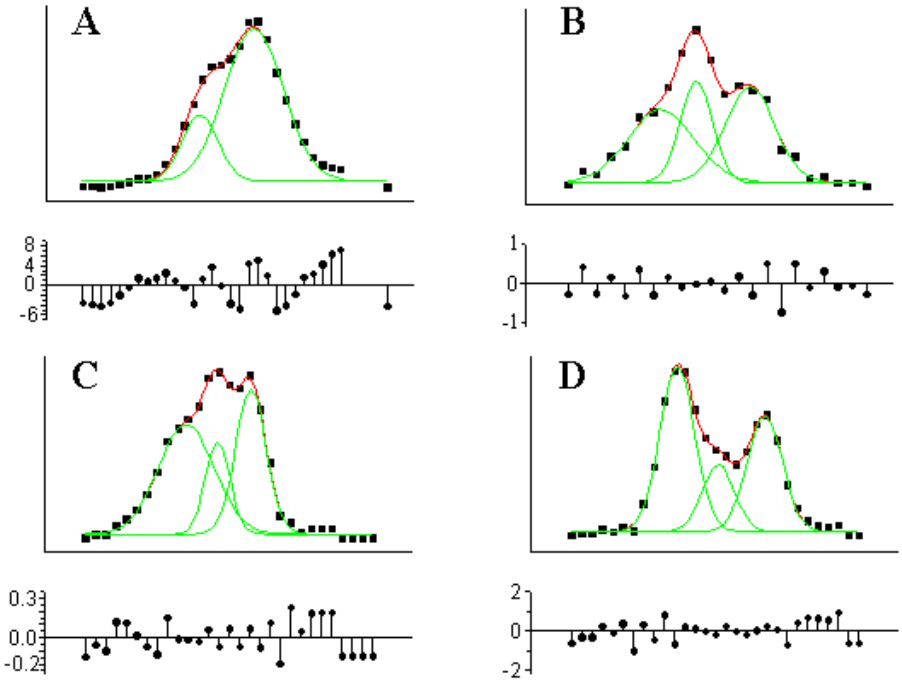

Figure 29. Fits and residuals of the ATD of bradykinin fragment 1-7 A) $[M+H]^+$ ions, B) $[M+Na]^+$ ions, C) $[M+K]^+$ ions, and D) $[M+Cs]^+$ ions.

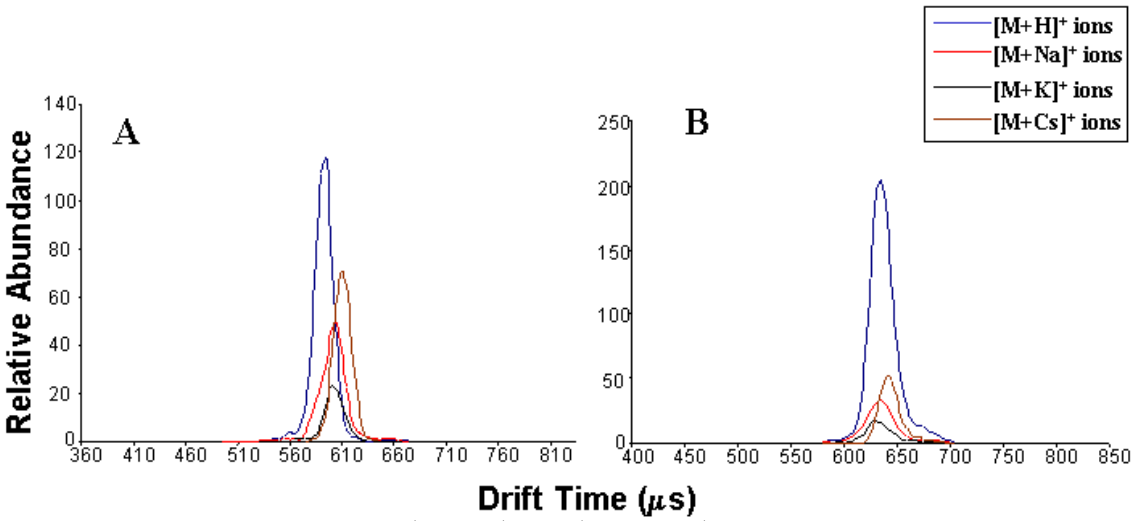

Figure 30. Arrival time distributions of $[M+H]^+$, $[M+Na]^+$, $[M+K]^+$, and $[M+Cs]^+$ ions of A) bradykinin fragment 2-7, and B) bradykinin fragment 5-9.

The ATDs of the protonated and alkali metal ion adducted species of BK2-7 (Figure 30A), BK5-9 (Figure 30B), BK1-8 (Figure 31A), BK2-9 (Figure 31B) and BK (Figure 31C) have a single peak.

However, while the ATDs of the $[M+H]^+$ ions of BK and BK5-9, BK2-7, BK1-8 and BK2-9 are dominated by a single peak, only those of BK (Figure 32A), BK2-7 (Figure 33A), and BK1-8 (Figure 34A) were best fit with a single gaussian curve. The ATDs of $[M+H]^+$ ions of BK5-9 (Figure 35A) and BK2-9 (Figure 36A) were best fit with two gaussian curves. Although a single peak dominates them, the ATDs of BK2-7 (Figure 33B) and BK2-9 (Figure 36B) $[M+Na]^+$ ions, $[M+K]^+$ ions of BK (Figure 32C), BK1-8 (Figure 34C), BK5-9 (Figure 35C) and BK2-9 (Figure 36C) as well as BK1-8 $[M+Cs]^+$ ions (Figure 34D) are best fit with two gaussian curves. The remaining ATDs

(BK1-8 (Figure 34B), BK5-9 (Figure 35B), and BK $[M+Na]^+$ (Figure 32B) ions, BK2-7 $[M+K]^+$ ions (Figure 33C), and BK2-7 (Figure 33D), BK5-9 (Figure 35D), BK2-9

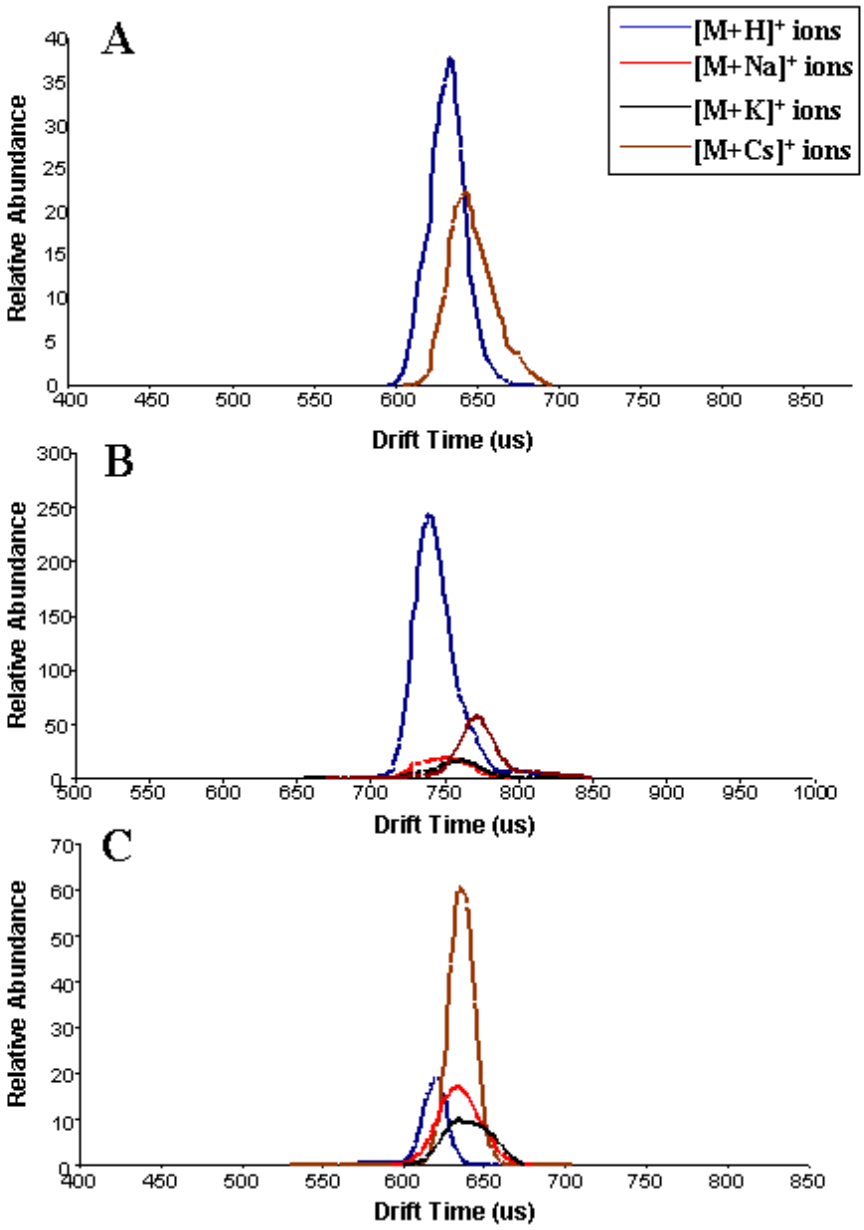

Figure 31. Arrival time distributions of $[M+H]^+$ and $[M+Cs]^+$ ions of A) bradykinin fragment 1-8 and the $[M+H]^+$, $[M+Na]^+$, $[M+K]^+$, and $[M+Cs]^+$ ions of B) bradykinin fragment 2-9, and C) bradykinin.

(Figure 36D), and BK $[M+Cs]^+$ ions (Figure 32D)) are accurately fit with a single gaussian curve.

Gas-phase H/D exchange experiments were performed on BK and BK2-9 $[M+H]^+$ ions as well as on the $[M+H]^+$ and $[M+Cat]^+$ ions of BK1-5, BK1-6, BK1-7, BK1-8, BK2-7, and BK5-9. Discussion and interpretation of H/D exchange reaction kinetics is focused on the first exchange for reasons detailed in CHAPTER II.

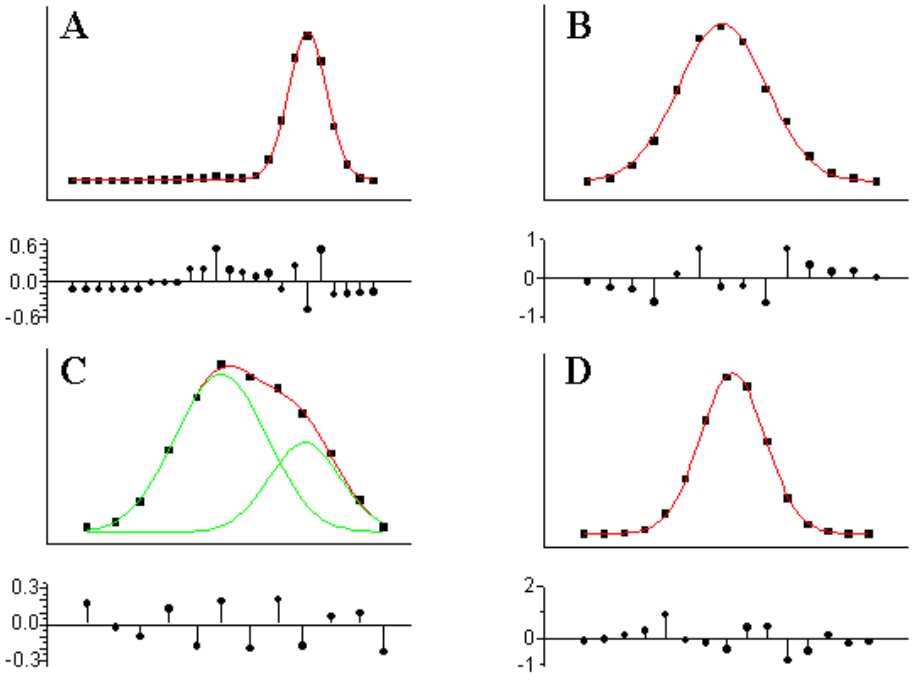

Figure 32. Fits and residuals of the ATD of bradykinin A) $[M+H]^+$ ions, B) $[M+Na]^+$ ions, C) $[M+K]^+$ ions, and C) $[M+Cs]^+$ ions.

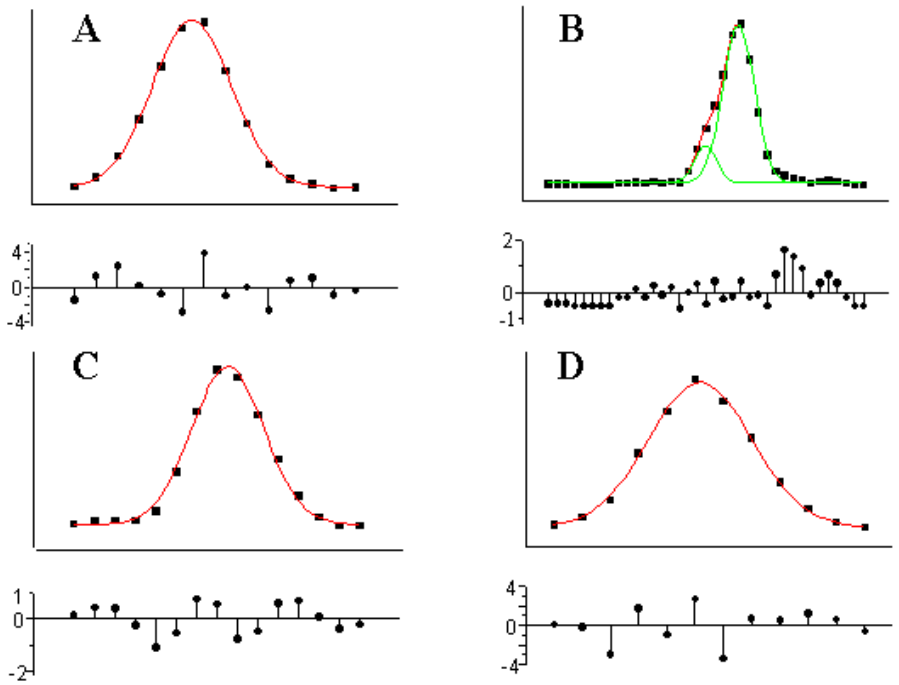

Figure 33. Fits and residuals of the ATD of bradykinin fragment 2-7 A) $[M+H]^+$ ions, B) $[M+Na]^+$ ions, C) $[M+K]^+$ ions, and C) $[M+Cs]^+$ ions.

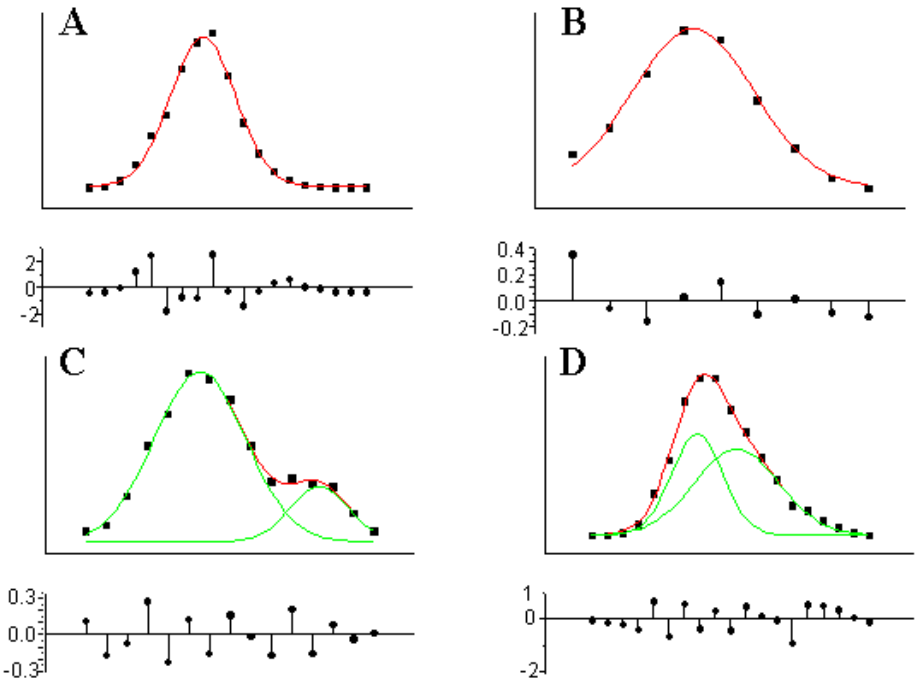

Figure 34. Fits and residuals of the ATD of bradykinin fragment 1-8 A) $[M+H]^+$ ions, B) $[M+Na]^+$ ions, C) $[M+K]^+$ ions, and C) $[M+Cs]^+$ ions.

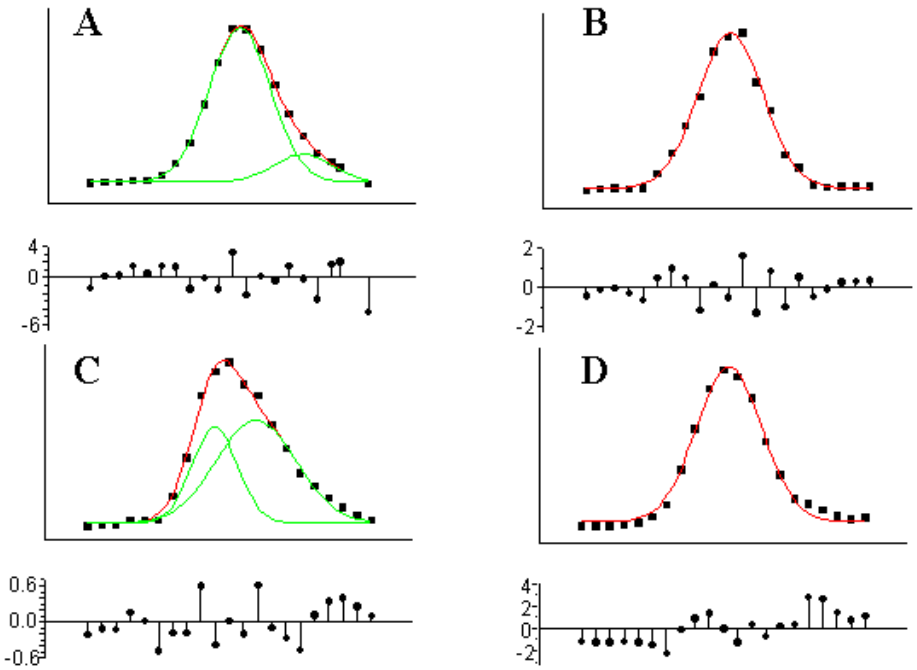

Figure 35. Fits and residuals of the ATD of bradykinin fragment 5-9 A) $[M+H]^+$ ions, B) $[M+Na]^+$ ions, C) $[M+K]^+$ ions, and D) $[M+Cs]^+$ ions.

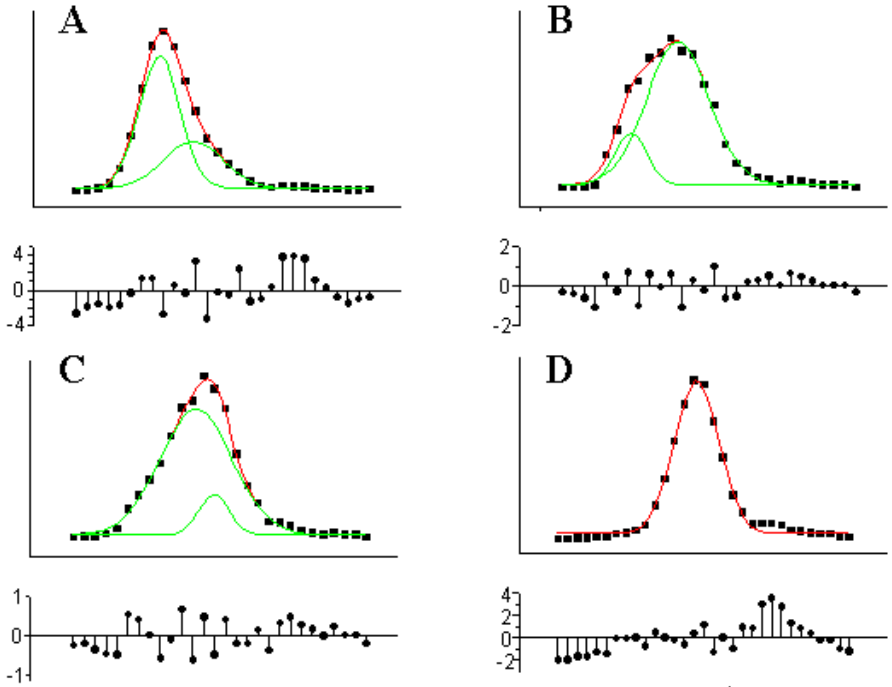

Figure 36. Fits and residuals of the ATD of bradykinin fragment 2-9 A) $[M+H]^+$ ions, B) $[M+Na]^+$ ions, C) $[M+K]^+$ ions, and D) $[M+Cs]^+$ ions.

Gas-phase H/D exchange ion-molecule reactions occur at a slower rate and to a lesser extent (on similar time-scales) for the alkali metal ion adducted species as compared to the protonated species for BK1-5, BK1-6, BK1-7, BK1-8, and BK5-9. However, the H/D exchange of BK2-7 $[M+H]^+$ and $[M+Cat]^+$ ions are very similar. For example, BK1-5 $[M+H]^+$ ions undergo 4 exchanges in 20 seconds of reaction time while $[M+Na]^+$ and $[M+Cs]^+$ ions exchange three and $[M+K]^+$ ions exchange two (Figure 37). Additionally, the rate of exchange is an order of magnitude slower for the alkali metal ion adducted species of BK1-5 relative to the $[M+H]^+$ ions. Similar trends are observed for BK1-6 (Figure 38), BK1-7 (Figure 39), BK1-8 (Figure 40), and BK5-9 (Figure 41).

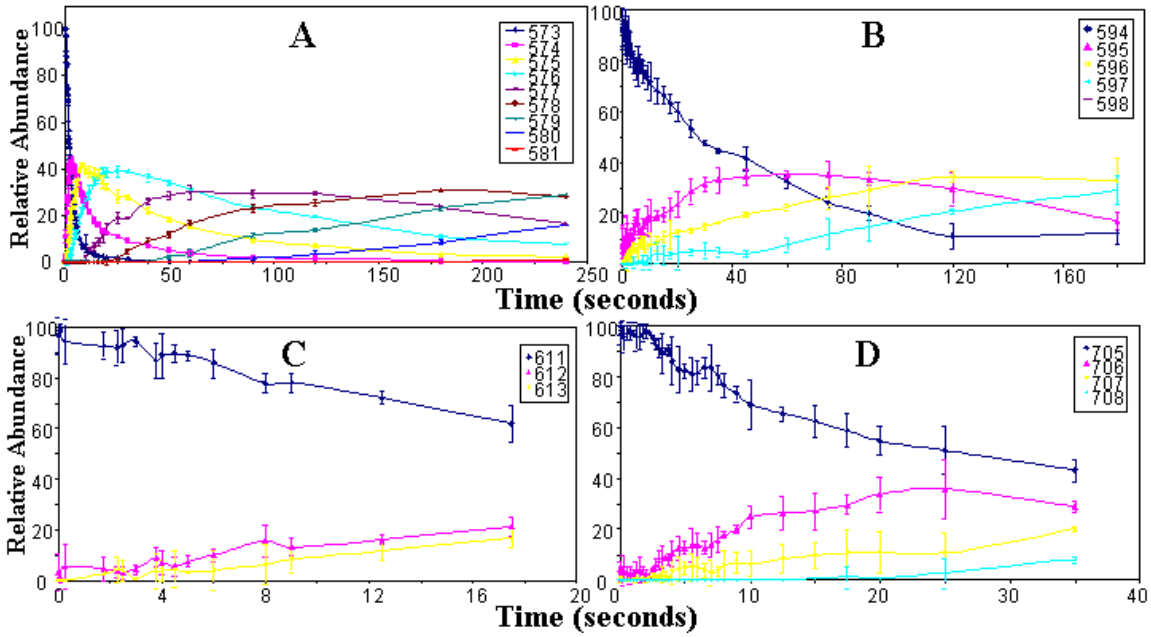

Figure 37. Temporal plots for the H/D exchange ion-molecule reactions of ND_3 with bradykinin fragment 1-5 A) $[M+H]^+$ ions, B) $[M+Na]^+$ ions, C) $[M+K]^+$ ions, and D) $[M+Cs]^+$ ions.

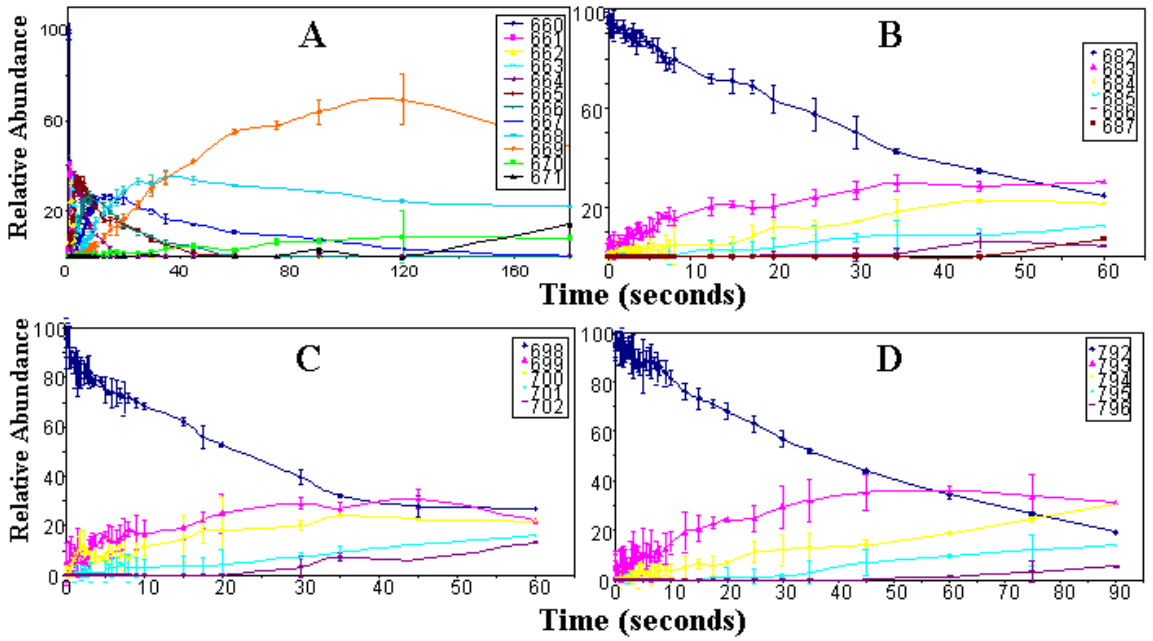

Figure 38. Temporal plots for the H/D exchange ion-molecule reactions of ND_3 with bradykinin fragment 1-6 A) $[M+H]^+$ ions, B) $[M+Na]^+$ ions, C) $[M+K]^+$ ions, and D) $[M+Cs]^+$ ions.

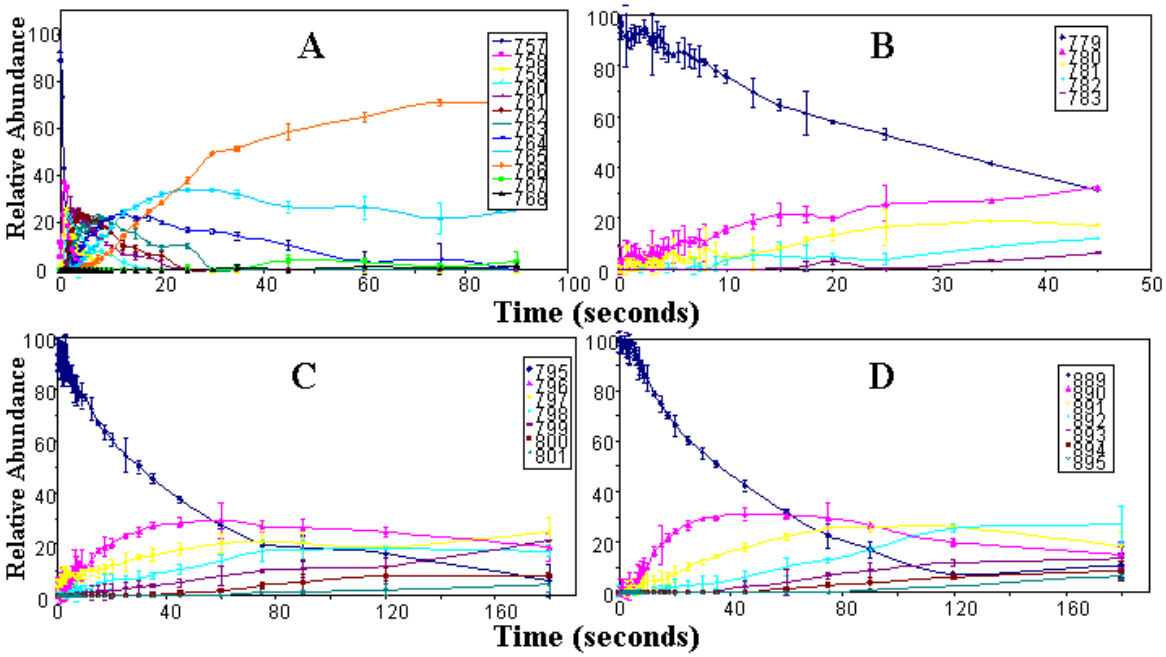

Figure 39. Temporal plots for the H/D exchange ion-molecule reactions of ND_3 with bradykinin fragment 1-7 A) $[M+H]^+$ ions, B) $[M+Na]^+$ ions, C) $[M+K]^+$ ions, and D) $[M+Cs]^+$ ions.

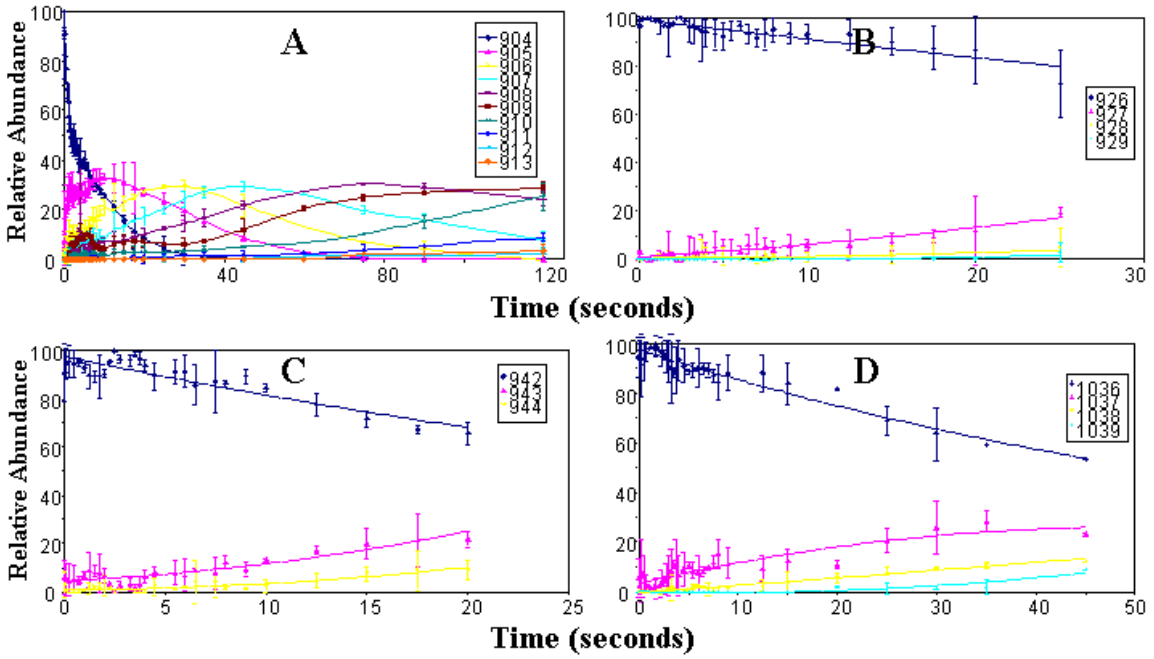

Figure 40. Temporal plots for the H/D exchange ion-molecule reactions of ND_3 with bradykinin fragment 1-8 A) $[M+H]^+$ ions, B) $[M+Na]^+$ ions, C) $[M+K]^+$ ions, and D) $[M+Cs]^+$ ions.

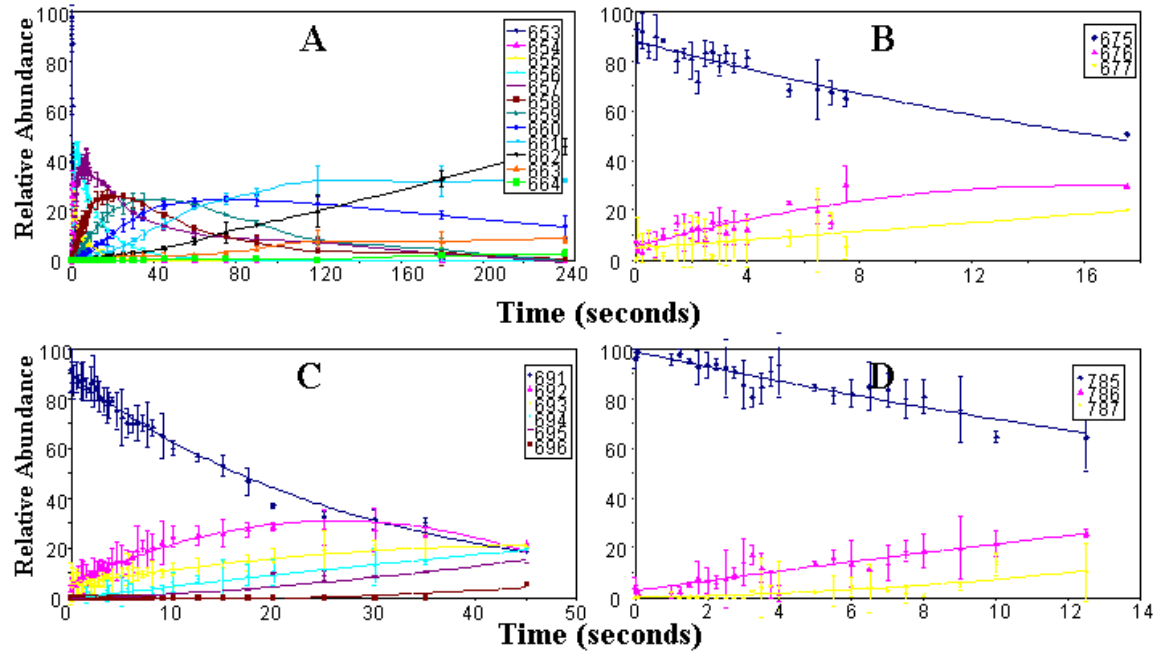

Figure 41. Temporal plots for the H/D exchange ion-molecule reactions of ND_3 with bradykinin fragment 5-9 A) $[M+H]^+$ ions, B) $[M+Na]^+$ ions, C) $[M+K]^+$ ions, and D) $[M+Cs]^+$ ions.

However the rate and extents of H/D exchange for the $[M+Cat]^+$ ions of BK2-7 are very similar to those of the $[M+H]^+$ ions. For example, $[M+H]^+$, $[M+Na]^+$, $[M+K]^+$ and $[M+Cs]^+$ ions exchange five hydrogens for deuteriums (Figure 42). Additionally the rates of exchange of the first hydrogen for a deuterium are very similar for the $[M+H]^+$, $[M+Na]^+$ and $[M+K]^+$ ions whereas the rate for exchange for the $[M+Cs]^+$ ions is an order of magnitude slower than for the other species.

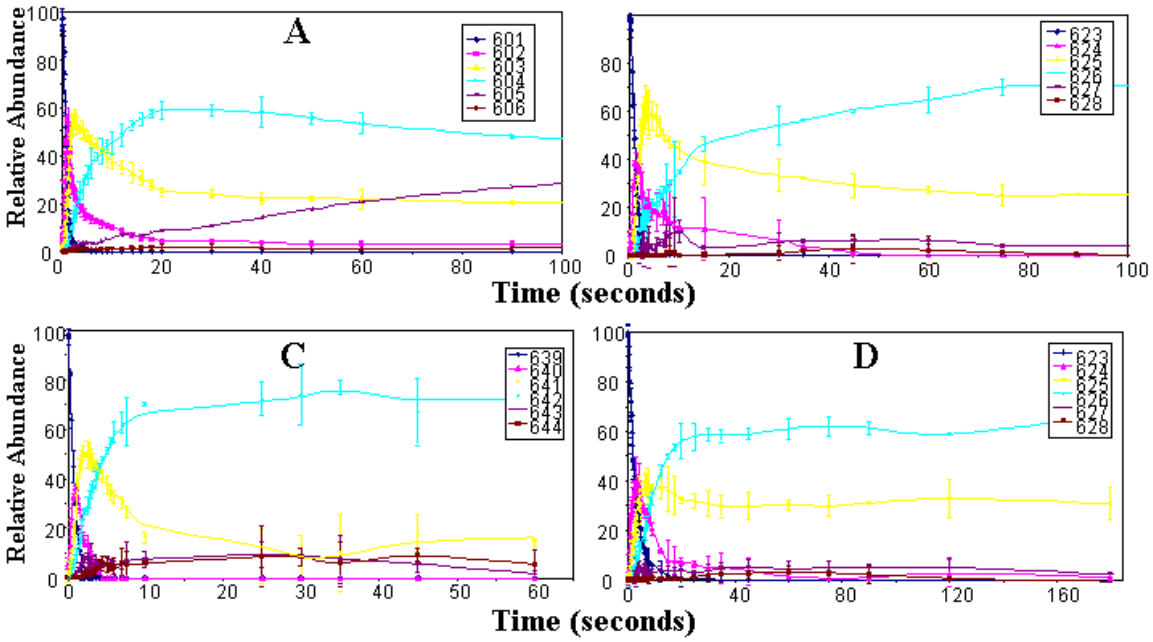

Figure 42. Temporal plots for the H/D exchange ion-molecule reactions of ND_3 with bradykinin fragment 2-7 A) $[M+H]^+$ ions, B) $[M+Na]^+$ ions, C) $[M+K]^+$ ions, and D) $[M+Cs]^+$ ions.

The decay of the signal for the all hydrogen species of the bradykinin fragments during H/D exchange was fit using both a bi-exponential and a single exponential decay equation. A bi-exponential equation gives a good fit to the decay of the all hydrogen

species of $[BK1\text{-}5+H]^+$, $[BK1\text{-}5+Na]^+$, $[BK1\text{-}5+Cs]^+$, $[BK1\text{-}6+K]^+$, $[BK1\text{-}7+K]^+$, $[BK1\text{-}7+Cs]^+$ and $[BK1\text{-}8+H]^+$ ions, whereas a single exponential equation is a better fit to the decay of the all hydrogen species of $[BK1\text{-}5+K]^+$, $[BK1\text{-}6+H]^+$, $[BK1\text{-}6+Na]^+$, $[BK1\text{-}6+Cs]^+$, $[BK1\text{-}7+H]^+$, $[BK1\text{-}7+Na]^+$, $[BK1\text{-}8+Na]^+$, $[BK1\text{-}8+K]^+$, $[BK1\text{-}8+Cs]^+$, $[BK2\text{-}7+H]^+$, $[BK2\text{-}7+Na]^+$, $[BK2\text{-}7+K]^+$, $[BK2\text{-}7+Cs]^+$, $[BK5\text{-}9+H]^+$, $[BK5\text{-}9+Na]^+$, $[BK5\text{-}9+K]^+$, $[BK5\text{-}9+Cs]^+$, $[BK2\text{-}9+H]^+$, and $[BK+H]^+$.

Molecular modeling, energy calculations and filtering techniques were used to generate and select possible conformations for the protonated and alkali metal ion adducted species of the bradykinin fragments. The intra-molecular interactions in the proposed structures for the alkali metal ion adducted species are very similar to those in the proposed structures for the protonated species for each fragment. For the species for which there were multiple peak features in the ATD (BK1-5, BK1-6, and BK1-7), the proposed structures for the more compact cationized species are very similar to the structures proposed for the more compact protonated species and likewise for the more extended conformer.

The two main structures proposed for the two conformers of the $[M+H]^+$ ions of BK1-5 are pictured in Figures 43A and 43B. In the structure corresponding to the lowest cross-section, the N-terminal arginine is interacting with the C-terminus whereas in the structure corresponding to the more extended structure the N-terminal arginine is interacting with the phenylalanine side chain. For each structure proposed for the two conformers of each alkali metal ion adducted species of BK1-5, the alkali metal ion is placed in the center of the circle formed by the peptide backbone and the carbonyl

oxygens are coordinated to the cation (Figures 43C-H). Proposed structures for the two conformers of the protonated and alkali metal ion adducted forms of BK1-6 have intra-molecular interactions that are similar to those seen in the structures proposed for BK1-5 ions (Figure 44).

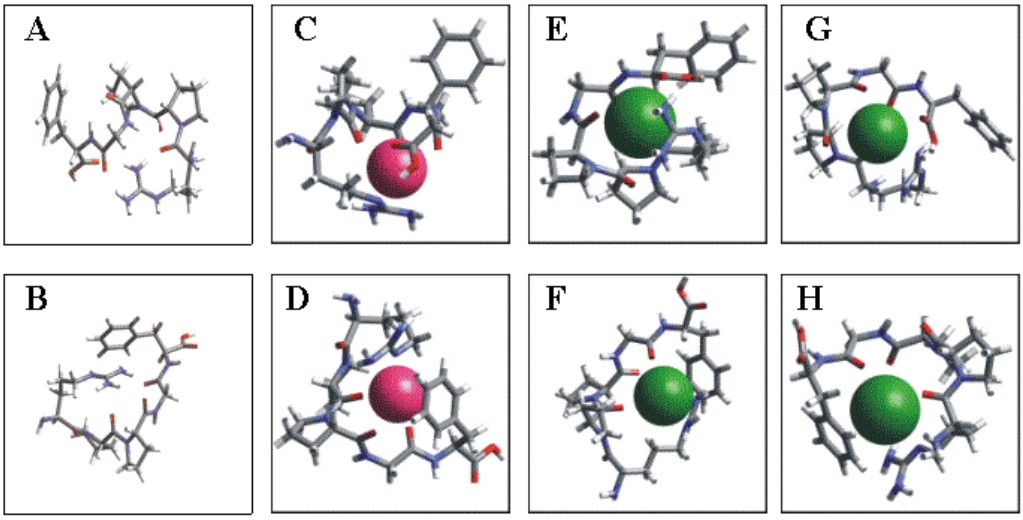

Figure 43. Proposed structures for A) more compact structure of bradykinin fragment 1-5 $[M+H]^+$ ions, B) more extended structure of bradykinin fragment 1-5 $[M+H]^+$ ions, C) more compact structure of bradykinin fragment 1-5 $[M+Na]^+$ ions, D) more extended structure of bradykinin fragment 1-5 $[M+Na]^+$ ions, E) more compact structure of bradykinin fragment 1-5 $[M+K]^+$ ions, F) more extended structure of bradykinin fragment 1-5 $[M+K]^+$ ions, G) more compact structure of bradykinin fragment 1-5 $[M+Cs]^+$ ions, and H) more extended structure of bradykinin fragment 1-5 $[M+Cs]^+$ ions.

A best fit structure for BK1-7 $[M+H]^+$ ions is shown in Figure 45A. The charged arginine side chain is interacting with both the phenylalanine side chain and the C-terminus and the peptide backbone forms a ring-like structure. In the proposed structures for BK1-7 $[M+Na]^+$ and $[M+K]^+$ ions the alkali metal ion is centered in the ring formed by the peptide backbone and is interacting with the C-terminus and the arginine side chain as well as with carbonyl oxygens. Also, in these structures the

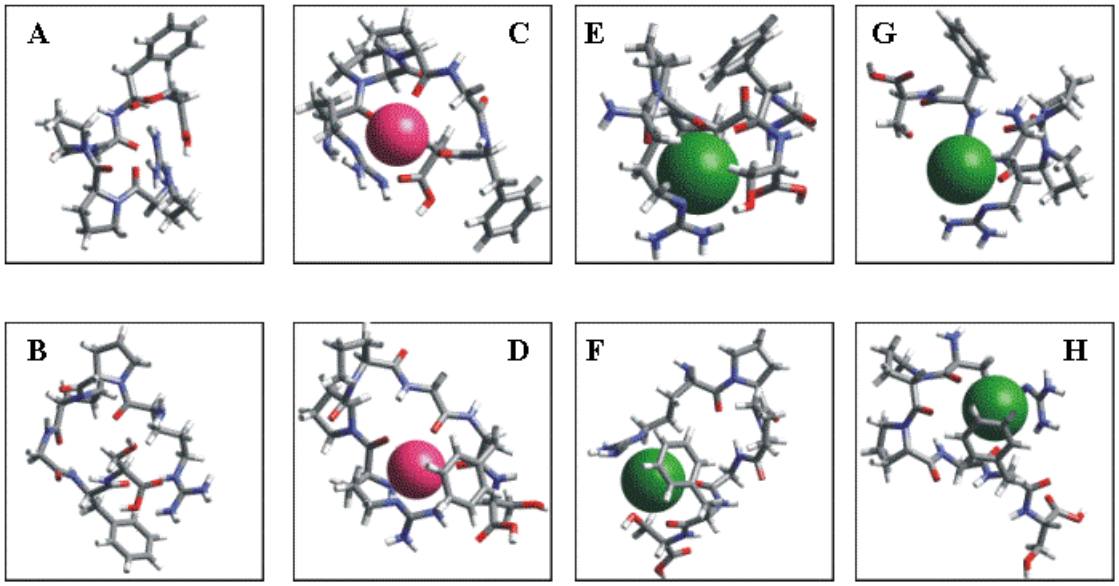

Figure 44. Proposed structures for A) more compact structure of bradykinin fragment 1-6 $[M+H]^+$ ions, B) more extended structure of bradykinin fragment 1-6 $[M+H]^+$ ions, C) more compact structure of bradykinin fragment 1-6 $[M+Na]^+$ ions, D) more extended structure of bradykinin fragment 1-6 $[M+Na]^+$ ions, E) more compact structure of bradykinin fragment 1-6 $[M+K]^+$ ions, F) more extended structure of bradykinin fragment 1-6 $[M+K]^+$ ions, G) more compact structure of bradykinin fragment 1-6 $[M+Cs]^+$ ions, and H) more extended structure of bradykinin fragment 1-6 $[M+Cs]^+$ ions.

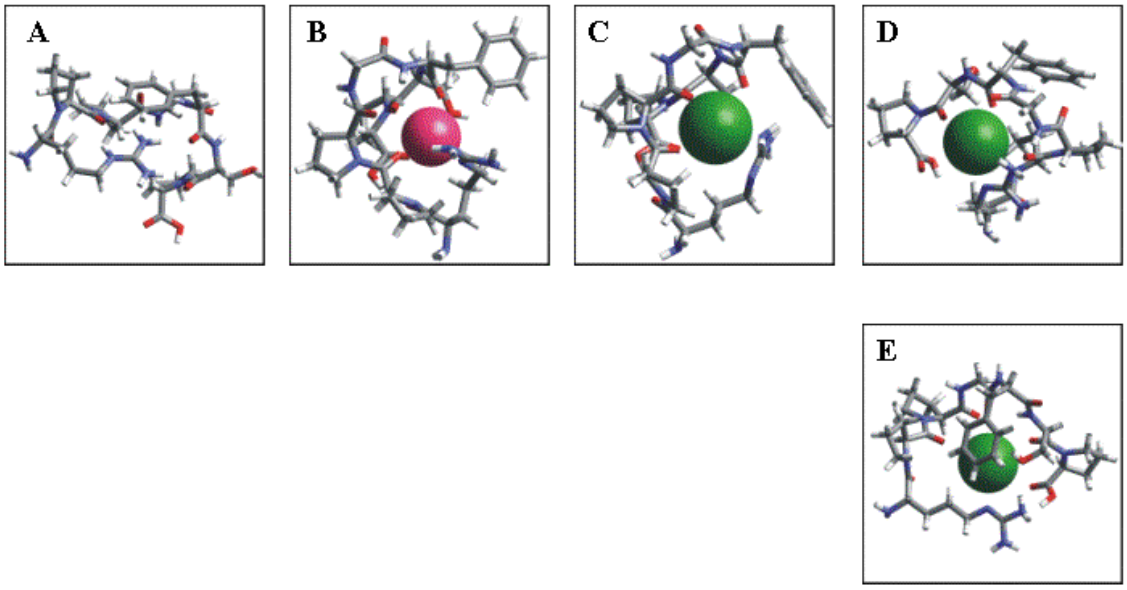

Figure 45. Proposed structures for A) bradykinin fragment 1-7 $[M+H]^+$ ions, B) bradykinin fragment 1-7 $[M+Na]^+$ ions, C) bradykinin fragment 1-7 $[M+K]^+$ ions, D) more compact structure of bradykinin fragment 1-7 $[M+Cs]^+$ ions, and E) more extended structure of bradykinin fragment 1-7 $[M+Cs]^+$ ions.

phenylalanine side chain is in close proximity to the arginine side chain (Figures 45B and 45C). In the proposed structure for the more compact cross-sections of $[M+Cs]^+$ ions the cesium ion is interacting with both the N-terminal arginine side chain and the C-terminus (Figure 45D). The proposed structure for the more extended $[M+Cs]^+$ conformer shows the cesium ion participating in interactions with the C-terminus, N-terminal arginine side chain as well as with the phenylalanine side chain (Figure 45E).

In the proposed structure for BK1-8 $[M+H]^+$ ions, the N-terminal arginine side chain and the C-terminus are participating in a hydrogen bonding interaction that forces the peptide backbone to form a very tight circle (Figure 46A). In the structures proposed for the alkali metal ion adducted species the alkali metal ion is placed between the N-terminal arginine and the C-terminus (Figures 46B-D).

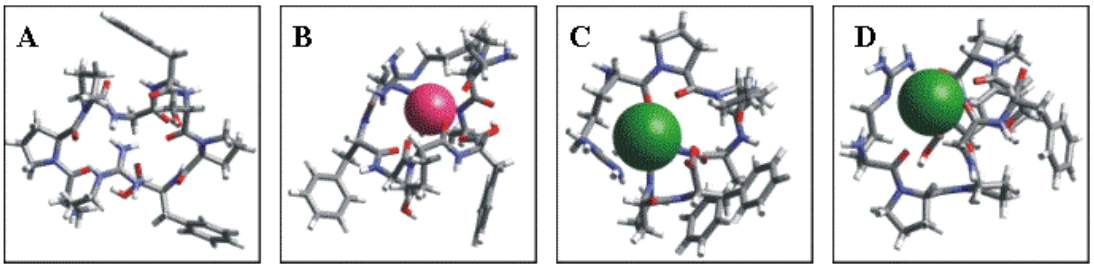

Figure 46. Proposed structures for A) bradykinin fragment 1-8 $[M+H]^+$ ions, B) bradykinin fragment 1-8 $[M+Na]^+$ ions, C) bradykinin fragment 1-8 $[M+K]^+$ ions, and D) bradykinin fragment 1-8 $[M+Cs]^+$ ions.

As can be seen in Figure 47A, the proposed structure for BK2-7 $[M+H]^+$ ions shows interactions occurring between the N-terminus/proline side chain and the C-terminal carbonyl oxygen as well as with the serine side chain. In the structures

proposed for the alkali metal ion adducted species the alkali metal ion is interacting with the N-terminus/proline side chain and the C-terminal carbonyl oxygen (Figures 47B-D).

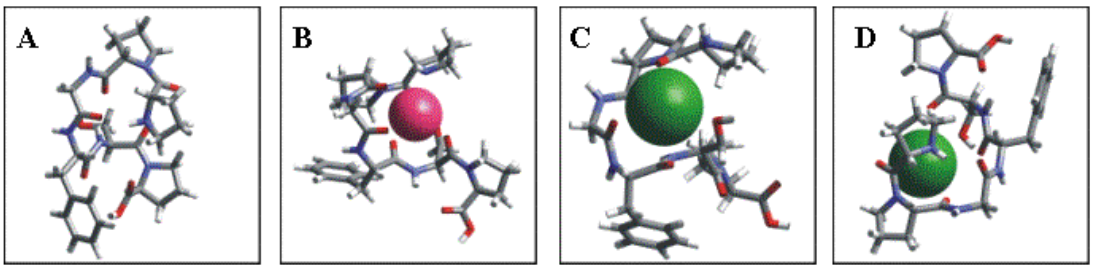

Figure 47. Proposed structures for A) bradykinin fragment 2-7 $[M+H]^+$ ions, B) bradykinin fragment 2-7 $[M+Na]^+$ ions, C) bradykinin fragment 2-7 $[M+K]^+$ ions, and D) bradykinin fragment 2-7 $[M+Cs]^+$ ions.

As shown in Figure 48A, the proposed structure for BK5-9 $[M+H]^+$ ions shows an interaction occurring between the C-terminal arginine side chain and the N-terminal phenylalanine ring. In the proposed structures for the alkali metal ion adducted species, the cation is interacting with the C-terminal arginine side chain and the N-terminal phenylalanine ring (Figures 48B-D).

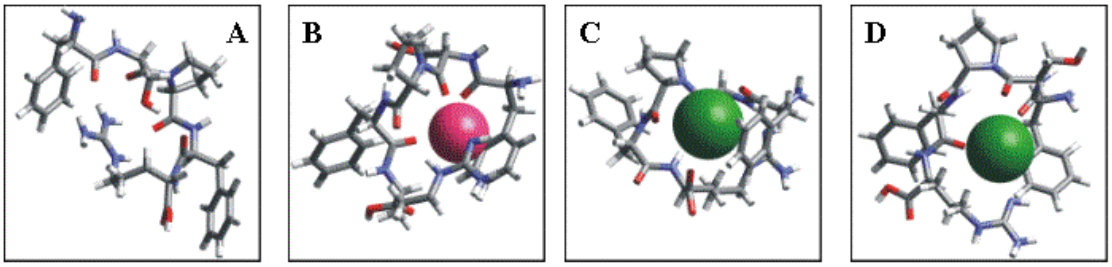

Figure 48. Proposed structures for A) bradykinin fragment 5-9 $[M+H]^+$ ions, B) bradykinin fragment 5-9 $[M+Na]^+$ ions, C) bradykinin fragment 5-9 $[M+K]^+$ ions, and D) bradykinin fragment 5-9 $[M+Cs]^+$ ions.

In the proposed structure for BK2-9 $[M+H]^+$ ions an interaction between the N-terminus/proline side chain, the N-terminal carbonyl oxygen and the C-terminal arginine side chain is occurring (Figure 49A). In the proposed structures for the alkali metal ion adducted species the cations (Na^+, K^+ and Cs^+) are interacting with the N-terminus/proline side chain, the N-terminal carbonyl oxygen and the C-terminal arginine side chain (Figures 49B-D).

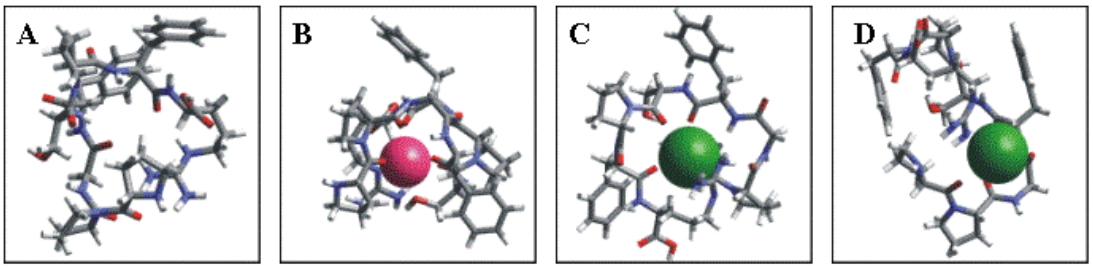

Figure 49. Proposed structures for A) bradykinin fragment 2-9 $[M+H]^+$ ions, B) bradykinin fragment 2-9 $[M+Na]^+$ ions, C) bradykinin fragment 2-9 $[M+K]^+$ ions, and D) bradykinin fragment 2-9 $[M+Cs]^+$ ions.

The proposed structures for BK $[M+H]^+$, $[M+Na]^+$, $[M+K]^+$ and $[M+Cs]^+$ ions are all zwitterions. In the proposed structure for BK $[M+H]^+$ ions, the two positively charged arginine side chains are interacting with the negatively charged C-terminus. Additionally, the charged C-terminal arginine side chain is interacting with backbone carbonyl oxygens (Figure 50A). In the proposed structures for BK $[M+Na]^+$, $[M+K]^+$ and $[M+Cs]^+$ ions, the charged N-terminal arginine side chain is interacting with the negatively charged C-terminus, while the neutral C-terminal arginine side chain is

interacting with the alkali metal ion, which carries a second charge. Additionally, the alkali metal ions are interacting with the backbone carbonyl oxygens (Figures 50B-D).

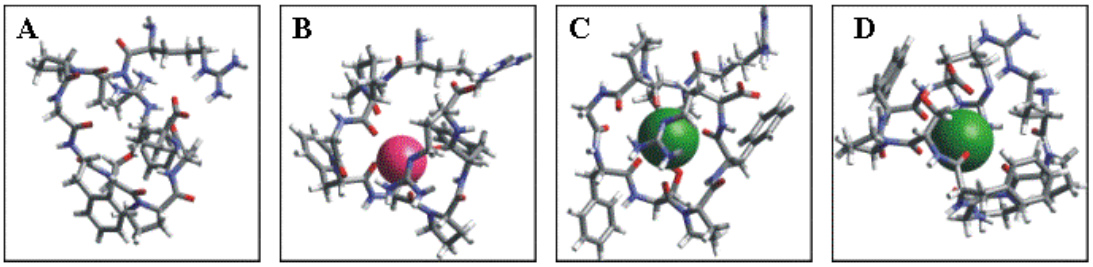

Figure 50. Proposed structures for A) bradykinin $[M+H]^+$ ions, B) bradykinin $[M+Na]^+$ ions, C) bradykinin $[M+K]^+$ ions, and D) bradykinin $[M+Cs]^+$ ions.

Discussion

Bowers and coworkers investigated the structure of gas-phase bradykinin $[M+H]^+$ ions and concluded that bradykinin exists as multiple conformations with similar collision cross-sections.[31] Here the structure of bradykinin gas-phase ions are re-examined, however, the approach is to study specific fragments of bradykinin in an effort to deconvolute the effect of salt (Na^+, K^+, Cs^+) adduction on the gas-phase conformation of bradykinin as compared to the conformations of $[M+H]^+$ ions. The presence of multiple peak features in the ATDs of BK1-5 (Figure 26A) and BK1-6 (Figure 26B) is interpreted to indicate the presence of multiple non-interconverting conformers. Although the ATD of the $[M+H]^+$ ions of BK1-7 (Figure 26C) does not contain distinct multiple peaks, a shoulder is evident and deconvolution of the ATD of BK1-7 $[M+H]^+$ ions is best fit with two gaussian curves (Figure 29A), which I interpret

to indicate the presence of multiple conformers for BK1-7 as well. The observed decrease in the resolution between the peaks as the fragment series progresses from 1-5 to 1-7 suggests that the barrier to interconversion between the conformers is lowered as the fragment length is increased, which would account for the appearance of a single, slightly broadened peak in the ATDs of BK1-8 and BK (Figures 31A and C, respectively).

Additionally, the multiple peak features seen in the ATDs of BK1-5 (Figure 26A) and BK1-6 (Figure 26B) are conserved upon adduction of alkali metal ions (Na^+, K^+, Cs^+). The conservation of multiple peaks is interpreted to indicate the general structure of the protonated species is preserved upon alkali metal ion adduction contrary to the suggestion made by Wyttenbach *et al.*, which stated that sodium ion adduction led to a conformational change in the peptide.[89] Furthermore, the resolution of the multiple peaks observed in the ATDs of protonated and cationized BK1-6 (Figure 26B) and BK1-7 (Figure 26C) increases upon alkali metal ion adduction, which is clearly demonstrated by comparing the ATDs of protonated BK1-7 ions to cesiated BK1-7 ions (Figure 26C). I interpret the increase in resolution to indicate that alkali metal ion adduction leads to differentiation of the fine structure details (*i.e.*, intra-molecular interactions) that are responsible for the presence of the two populations of conformers in the ATDs of the $[M+H]^+$ ions; the barrier to inter-conversion between the two populations of structures is increased upon alkali metal ion adduction.

One peak was observed in the ATDs of BK1-8 (Figure 31A), BK2-7 (Figure 30A), BK5-9 (Figure 30B), and BK2-9 (Figure 31B) as well as BK (Figure 31C),

however, deconvolution of the ATDs indicated that all of these species, with the exception of BK2-7 (Figure 33), contain multiple peak features in their ATDs. In the cases of BK (Figure 31C), BK5-9 (Figure 30B), BK1-8 (Figure 31A) and BK2-9 (Figure 31B), the multiple peak features are represented by a broadened peak in the ATD. For these species, the presence of one peak in the ATD was conserved upon alkali metal ion adduction and deconvolution of the ATDs indicates that the multiple peak features are carried over or enhanced upon alkali metal ion adduction, which is interpreted to suggest the conservation of structure upon cationization. Although deconvolution of the ATDs of BK (Figure 32), BK5-9 (Figure 35), BK1-8 (Figure 34) and BK2-9 (Figure 36) indicate that multiple conformations are present, the peaks shapes can be interpreted to indicate that an interconversion between multiple structures, or an averaging effect, might be occurring.

The difference between the calculated cross-sections of the alkali metal ion adducted species and those of the protonated species are no more than 4% for all bradykinin fragments (Table 5), which results in a deviation of the cationized species from the expected linear trend exhibited by the peptides in an IM-MS experiment (Figure 25). Such behavior is in agreement with previous ion mobility experiments where the calculated cross-sections of the cationized species are only slightly larger than the protonated species[31] and, in some cases, smaller than the protonated species.[91]

In an effort to further characterize the intra-molecular interactions present in the gas-phase conformers of protonated and alkali metal ion adducted bradykinin and its analogues, gas-phase H/D exchange experiments were performed. With the exception of

BK2-7, gas-phase H/D exchange ion molecule reactions occur at a slower rate and to a lesser extent for the alkali metal ion adducted species as compared to the protonated species studied in this chapter. Behavior similar to this has been previously observed and has been explained in terms of either a change in conformation or lack of a mobile proton upon alkali metal ion adduction.[97, 98] As discussed above, conservation of multiple peak features in the ATDs of the cationized BK1-5 and BK1-6 ions are interpreted to suggest that the conformation does not change upon alkali metal ion adduction. Therefore, the change in H/D exchange behavior upon alkali metal ion adduction seems to be more accurately explained in terms of the mobile proton model rather than a change in conformation. Upon alkali metal ion adduction the charge site becomes the cation. This differs significantly from the charge site in protonated species being a peptide functionality (basic side chain or N-terminus). Because H/D exchange is charge directed, replacement of a proton with a cation would significantly affect the exchange, by hindering formation of the proton bridge intermediate that leads to exchange. Additionally, as Reyzer *et al.* suggest, the presence of an alkali ion in place of a proton makes the other labile hydrogens in the molecule less acidic and therefore less labile.[98] While this is a reasonable explanation for the H/D exchange behavior of BK and BK1-5, BK1-6, BK1-7, BK1-8, BK5-9, and BK2-9, H/D exchange for BK2-7 occurred at similar rates and extents for the protonated and cationized species, which, according to the discussion above, can be interpreted to indicate that the acidity of the labile hydrogens does not change upon alkali metal ion adduction or that the lack of a mobile proton results in a reduction of the rate and extent of H/D exchange. The lack of

arginine(s) in BK2-7 might be responsible for the change in the trend of H/D exchange behavior upon alkali metal ion adduction. In the structures proposed for the arginine-containing fragments (see Results), the arginine side chain is either the charge site or is consistently in close proximity to the charge site. It is possible that, due to the lack of a strongly basic site (arginine), H/D exchange might take place at a site different from the charge site and the nature of this site would not change upon alkali metal ion adduction resulting in similar rates and extents of H/D exchange for the protonated and cationized species of BK2-7.

The decay of the signal of the all hydrogen species of the bradykinin fragments during H/D exchange was fit and a bi-exponential decay better describes the degradation of the all hydrogen species of $[BK15+H]^+$, $[BK1-5+Na]^+$, $[BK1-5+Cs]^+$, $[BK1-6+K]^+$, $[BK1-7+K]^+$, $[BK1-7+Cs]^+$ and $[BK1-8+H]^+$ ions than does a single exponential decay. The ATDs of these species all exhibit multiple peak features, with the exception of $[BK1-8+H]^+$ ions, somewhat correlating H/D exchange behavior with IM-MS data. However, a single exponential decay equation better fits the H/D exchange data of the remaining protonated and alkali metal ion adducted species. While species such as $[BK15+K]^+$, $[BK16+H]^+$, $[BK16+Na]^+$ and $[BK16+Cs]^+$ show evidence for multiple conformations in IM-MS, this is not the case for H/D exchange. It is possible that the H/D exchange data does not accurately reflect the population of ions due to the use of ND_3 as the deuterating agent. Campbell *et al.*, observed that ND_3 exchanges multiple hydrogens per collision event 22% of the time.[42] Due to this, use of ND_3 as the deuterating agent may result in the analysis of H/D exchange kinetic data ineffective in

terms of differentiating between different conformational populations. Use of deuterating agents that exchange only one deuterium for hydrogen per collision event (*i.e.*, D_2O, CD_3OD, CD_3CO_2D) was not possible due to the low gas-phase basicities of these reagents relative to the gas-phase basicities of bradykinin and its fragments.

Possible structures for the conformations of protonated and cationized BK1-5 ions are shown in Figure 43. In the structures that are proposed for the more compact conformations of the protonated and cationized structures of BK1-5, the charge site (a proton in the case of the protonated species and a alkali metal ion in the case of the cationized species) is consistently interacting with the N-terminal arginine side chain and the C-terminus while the phenylalanine side chain is not interacting with anything. A similar conservation of interactions is observed for the structures proposed for the more extended conformations of the protonated and cationized structures, where the charge site is consistently interacting with the N-terminal arginine side chain and the phenylalanine side chain while the C-terminus is not interacting with anything. Additionally, the peptide backbone forms a ring and the carbonyl oxygens and amide nitrogens are turned inward to participate in stabilizing interactions (hydrogen bonding in the case of the protonated species and multi-dentate binding in the case of the cationized species) for all BK1-5 species. This is in agreement with the IM-MS data that was interpreted to suggest that the structure is not dramatically changed upon alkali metal ion adduction. Conservation of the charge site interactions as well as the general structure that is observed in the protonated species is also observed in the structures

proposed for the cationized species of BK (Figure 50), BK1-6 (Figure 44), BK1-8 (Figure 46), BK2-7 (Figure 47), BK5-9 (Figure 48) and BK2-9 (Figure 49).

The proposed structure for BK1-7 $[M+H]^+$ ions, pictured in Figure 45A, shows the charge site is interacting with both the phenylalanine side chain and the C-terminus, making the structure very similar to the structures proposed for the two conformations of BK1-5 and BK1-6 $[M+H]^+$ ions. From investigation of the both the IM-MS data, through deconvolution of the ATDs, and the proposed structures it can be suggested that the ATD of BK1-7 $[M+H]^+$ ions is composed of a population of structures very similar to those of BK1-5 and BK1-6 that are now able to readily convert to one another on the time scale of the experiment. The structure proposed for BK1-7 $[M+H]^+$ ions represents an average of the two structures, making it in agreement with IM-MS data. The charge site interactions seen in the compact and extended structures proposed for both BK1-5 and BK1-6 $[M+H]^+$ ions are present in the proposed structure for BK1-7 $[M+H]^+$ ions. The two proposed structures for the BK1-7 $[M+Cs]^+$ ions are very similar to the proposed structures for that species of BK1-5 and BK1-6, in agreement with the IM-MS data where the ATD of BK1-7 $[M+Cs]^+$ ions is now composed of two peak maxima. Apparently, cesium ion adduction raises the barrier of interconversion between the conformer where the charge site interacts with the arginine side chain and the C-terminus and the conformer where the charge site interacts with the arginine side chain and the phenylalanine side chain, enabling IM-MS to resolve their difference in collision cross-sections.

The structures proposed for BK $[M+H]^+$, $[M+Na]^+$, $[M+K]^+$ and $[M+Cs]^+$ ions are all in the zwitterionic form, in agreement with extensive gas-phase experimental studies suggesting that bradykinin exists as a zwitterions in the gas phase.[6, 27] Conservation of the charge site interactions as well as the general structure that is observed in the protonated species is observed for the alkali metal ion adducted species of BK. The protonated species exhibits interactions between the negatively charged C-terminus and the two charged arginines as well as between the charged C-terminal arginine and the backbone carbonyl oxygens. This interaction is somewhat conserved when alkali metal ion adduction occurs, in that the negatively charged C-terminus is still participating in an interaction with the charged N-terminal arginine side chain and the C-terminal side chain is participating in interactions with the charged cation and the backbone carbonyl oxygens.

Conclusions

It was observed by IM-MS experiments that the collision cross-sections of the alkali metal ion adducted (Na^+, K^+ and Cs^+) species of BK and BK1-5, BK1-6, BK1-7, BK1-8, BK2-7, BK5-9 and BK2-9 are very close to those of the protonated species, resulting in a deviation from the expected linear relationship observed in IM-MS experiments. This is consistent with previous ion mobility experiments that indicate that salt adducted species are only slightly larger than the protonated species[31] and, in some cases, smaller than the protonated species.[91] Additionally, multiple peak features observed in the ATDs of protonated BK1-5, BK1-6 and BK1-7 are conserved upon

alkali metal ion adduction, which is interpreted to indicate that the structures do not significantly change.

Data from gas-phase H/D ion-molecule reactions show that alkali adducted species exchange slower and to a lesser extent than protonated species in arginine-containing peptides. Behavior similar to this has been previously observed for peptides and other biomolecules.[97, 98] However, BK2-7 had similar rates and extents of H/D exchange for the protonated and alkali metal ion adducted species. It is possible that, due to the lack of a strongly basic site (arginine), H/D exchange might take place at a site different from the charge site and the nature of this site would not change upon alkali metal ion adduction resulting in similar rates and extents of H/D exchange for the protonated and cationized species of BK2-7.

Molecular modeling were used to further probe the fine structure detail of these molecules in order to understand the cause for deviations from the tend-line in the IM-MS experiments. From analysis of the proposed structures it can be concluded that conformation of the peptides does not significantly change upon alkali metal ion adduction. Furthermore, the charge site interactions are conserved within each species. The lack of change in conformation explains the deviation of cationized species from the expected trend line. The peptide backbone of the proposed structures forms a pocket into which the cations can fit resulting in little or no change to the overall size of the conformation. In some cases, the cation might fit into a pocket that is slightly large which might induce a decrease in the conformation's cross-section due to a reduction of

the size of the pocket to accommodate the cation's affinity for multi-dentate binding[31], as is the case for BK5-9.

CHAPTER VI

OBSERVATION OF SOLUTION-PHASE MEMORY EFFECTS IN GAS-PHASE BRADYKININ FRAGMENT 1-5: EVIDENCE FROM ION-MOBILITY AND H/D EXCHANGE MASS SPECTROMETRY

Introduction

The most basic form of protein structure is the protein's composition, or sequence, which defines what amino acids are physically linked to one another. Consequently, intra-molecular interactions within the protein can bring amino acids that are not directly linked together close to each other; such interactions constitute secondary and tertiary protein structure. Studies of peptide and protein structure play a major role in modern molecular biophysics and drive development of new techniques for probing peptide/protein structure. High-throughput, gas-phase techniques for sequencing peptides and proteins are well established and significant progress has been made in the development of gas-phase techniques for the characterization of secondary and tertiary peptide/protein structure.[23, 31, 107-109] Although gas-phase peptide/protein structure studies may aid understanding the role of intra-molecular interactions in fragmentation mechanisms as well as the development of sequencing algorithms, the relevance of gas-phase to solution-phase structure has not been well defined. Studies of gas-phase structure are important, however, for understanding inta-molecular interactions (*i.e*, hydrogen bonding, van der Waals interactions and hydrophobic forces) as well as how such interactions influence conformation of peptides and proteins both in the gas and solutions phases. Progress is also being made in the development of

techniques that allow selective solvation (in terms of number of solvent molecules) of gas-phase peptide/protein ions[18], and these studies may serve to further our understanding of solvent affects on structure and function.

Studies of intra-molecular interactions on peptide ion structure are important in understanding the balance of interactions that determine the three-dimensional structure of a peptide/protein in solution. Hydrogen bonding, hydrophobic forces and van der Waals interactions all play key roles in determining peptide/protein structure; however, solvent/protein interactions have an overwhelming influence on protein structure *in vivo*. Results from several studies suggest that in some cases gas-phase ions retain some memory of the solution-phase structure, thus different solvent systems can yield different gas-phase structures. For example, Wang *et al*. used gas-phase H/D exchange to look at the effects of solvent conditions on selected charge states of the N-terminal domain of cardiac troponin c.[14] They observed that the deuterium incorporation differed between aqueous and organic starting solution conditions, and concluded that the gas-phase conformations from different solvent conditions were unalike. Gross and coworkers observed that the Arrhenius activation parameters for loss of heme from the 9^+ to 12^+ charge states of myoglobin show a dependence on solvent, *i.e.*, pseudo-native versus denaturing solvent conditions.[15] Additionally, Covey *et al.* observed a solvent dependence on energy loss collision cross-sections of cytochrome c; ions were larger when originating from high organic solvent conditions than from aqueous solvent conditions.[110] Jurchen *et al.*, argued that the gas-phase conformation of the 11^+ charge state of cytochrome c retained memory of its solution-phase structure from native

solvent conditions. For example, the ion dissociated symmetrically (distribution of charges between product ions was nearly equal); however from denaturing solutions the ion dissociated asymmetrically.[16] The authors suggested that gas-phase conformations might yield information about the effect of solvent on peptide/protein structure as well as information about the stabilizing intra-molecular interactions.

Bradykinin is a nine-residue peptide (ArgProProGlyPheSerProPheArg) hormone found in human blood and urine.[99] It has been extensively studied because the presence of arginine at both the N- and C-termini can potentially influence the structure and reactivity of the ion. For example, data from fragmentation studies were interpreted as evidence that intra-molecular hydrogen bonds exist between the N- and C-terminal arginine residues as well as between the serine side chain and the protonated guanidine group.[5] However, collision-induced dissociation experiments suggest that the protonated guanidine group of bradykinin interacts with Pro^3 or Phe^5.[105] Gas-phase H/D exchange of bradykinin and derivatives of bradykinin indicate that the $[M+H]^+$ ion of bradykinin might exists as a zwitterion[27] as do blackbody infrared dissociation (BIRD) studies of bradykinin and its methyl-ester derivative.[6] However, hydroiodic attachment studies suggest that the $[M+H]^+$ ion does not exist as a zwitterion due to its ability to attach two HI molecules.[106]

Bowers and coworkers investigated the structure of gas-phase bradykinin $[M+H]^+$ ions and concluded that bradykinin exists as multiple conformations having collision cross-sections within two percent of each other.[31] In this chapter the structure of bradykinin gas-phase ions are re-examined, however, the approach is to study specific

fragments of bradykinin in an effort to deconvolute the effect of specific amino acid residues on the gas-phase conformation of bradykinin. London *et al.* used a similar approach to evaluate the structure of solution-phase bradykinin by using NMR.[101] In this chapter, results from IM-MS combined with gas-phase H/D exchange ion-molecule reactions, and molecular modeling are used to address the effects of sequence and solvent conditions used to prepared MALDI samples on the conformations of various analogs of bradykinin, with a focus on bradykinin fragment 1-5 (BK1-5) $[M+H]^+$ ions. Data presented in this chapter is used to establish that multiple structural features found in residues 1-5 might be the contributing factor to the broadening of the arrival time distribution of bradykinin observed by Wyttenbach, *et al*. The effect of intra-molecular interactions on peptide structure and how these interactions change as a function of peptide sequence and the percent water content in the solvent systems used to prepare MALDI samples is discussed.

Experimental and Computational Methods

Ion mobility measurements were made using a matrix-assisted laser desorption-ionization (MALDI)-ion mobility-reflectron-time-of-flight (TOF) mass spectrometer described previously (see Chapter II). Briefly, ions formed by MALDI drift through the ion mobility (IM) cell, filled to ≈1 torr of Helium, where they are separated on the basis of collision cross-section. IM field strengths ranging from 20 to 30 volts/cm·torr were used to acquire arrival time distributions (ATDs) of bradykinin and its fragments. Both the laser power and field strength were observed to have an effect on the resolution of the ATDs. High laser powers resulted in a broadening of the ATD for all species and at

high field strengths the resolution between the multiple conformations observed in the ATD of BK1-5 $[M+H]^+$ ions disappeared. We interpret this to signify that at high laser powers and field strengths the ion population sampled by IM-MS is no longer thermal; the ions have internal energy, allowing interconversion between conformers to occur. The collision cross-sections reported herein were obtained using an internal calibration method.[40] Briefly, a peptide with a known cross-section is used as a standard (bradykinin, 245Å^2) and the difference between the drift times of the standard and the ion of interest is measured multiple times and is used to calculate the cross-section of the ion of interest relative to the standard. The ATDs presented in this chapter are acquired by selecting a narrow mass range from the two-dimensional (mass spectrum and mobility spectrum) data and looking at it in one-dimension (mobility spectrum). The ATDs of BK1-5 $[M+H]^+$ ions were deconvoluted using a gaussian curve-fit equation with Origin graphing software (OriginLab Corporation). Both a single and multiple gaussian curves were used in the equations to determine the best fit of the ATDs. Because the fit will continue to improve by increasing the number of gaussian curves used, the best fit would be the number of gaussian curves, N, that most improved the fit over N-1 gaussian curves and resulted in little to no improvement in the fit of N+1 gaussian curves.

Ion mobility-surface-induced dissociation mass spectrometry (IM-SID-MS) experiments were performed on instrumentation described previously (see Chapter II). Briefly, ions are formed by MALDI and are separated on the basis of their collision-cross sections in an ion mobility cell with a Helium gas pressure of 1-2 torr. Time-slices

of ions are selectively collided onto a fluorinated self-assembled monolayer (F-SAM) surface with a collision energy of 40 eV, inducing fragmentation. Following the dissociation, ions are mass analyzed in a linear time-of-flight (TOF) mass spectrometer.

Gas-phase H/D exchange ion-molecule reactions were carried out on a 3 tesla Fourier transform (FT) ion cyclotron resonance (ICR) mass spectrometer described previously (see Chapter II). Ions were formed by MALDI and either trapped in the source region of a two-section cell or transferred to the analyzer region of the cell after a quadrupolar axialization event. To facilitate H/D exchange, ions were trapped in the presence of ND_3 gas for times ranging from 0.005 to 360 seconds. Pseudo-first order kinetics were obtained by operating at ND_3 pressures of $6x10^{-8}$ torr. Temporal plots were generated by plotting ion intensity, corrected for the natural isotope abundance, versus time.

Studies of the charge state distribution of BK1-5 ions as a function of solvent composition were performed on an electrospray triple quadrupole reflectron time-of-flight mass spectrometer (MDS Sciex QSTAR Pulsar).

Circular Dichroism (CD) experiments were performed on an Aviv 62DS model CD spectrophotometer (Aviv Associates, Lakewood, NJ). A 0.1 mm pathlength was used and the spectra were taken at 4°C. The wavelength was scanned from 250 nm to 180 nm in 0.5 nm steps with an average time for each step of 3 seconds.

All molecular dynamics calculations were performed with the Cerius (Accelrys) suite of programs using the consistent forcefield (CFF1.01). Model structures for the peptide ions were generated using a simulated annealing cycle[72, 73] where the structure

was heated from 300 Kelvin (K) to 1000 K in steps of 50 K with relaxation times of 0.1 picoseconds (ps), making the entire simulation time 280 ps for 100 cycles. Semi-empirical calculations using AM1 parameters were used to determine the energy of each structure. The collision cross-sections of each structure were calculated using the projection approximation, the exact hard sphere scattering method and the trajectory method using a program designed by Mesleh, *et al.*[69, 70] Four hundred structures of BK1-5 $[M+H]^+$ ions were generated by simulated annealing. Two hundred low-energy (within 15 kcal/mol of the lowest energy structure) structures were classified into groups based on structure and intra-molecular interactions. The structures proposed herein were chosen based on agreement between the experimental collision cross-section, cluster population (structures in the most populated cluster within the cross-section range were considered most likely) as well as energy level. Additionally, the energies (b3LYP/6-31g(d') level of theory)[111] of the proposed structures in this chapter are within 5.8 kcal/mol of each other.

Peptides were purchased from Sigma Aldrich and SynPep and used without further purification. 2', 5'-Dihydroxybenzoic acid, 2', 4', 6'-trihydroxyacetophenone monohydrate, p-nitroaniline, 3-nitrobenzyl alcohol, glycerol, and D(-)fructose were purchased from Sigma Aldrich and used without further purification. Alpha-cyano-4 hydroxycinnamic acid was purchased from Sigma Aldrich and was recrystalized prior to use. ND_3 gas was purchased from Bachem and used without filtering. HPLC grade methanol and deionized (Milli-Q Water System, Millipore) water were used for all experiments. The solutions for ion mobility-mass spectrometry measurements were

prepared by dried droplet using α-cyano-4 hydroxycinnamic acid as matrix with a matrix-to-analyte molar ratio of 400:1. Liquid MALDI[112] samples for IM-MS were prepared by applying the liquid matrix (3-nitrobenzyl alcohol and/or glycerol) to the probe tip and then depositing into the liquid ≈1 μL of peptide with a concentration of ≈1 mg/mL in either methanol or water. When an additional matrix was used (p-nitroaniline or α-cyano-4 hydroxycinnamic acid), the liquid matrix (glycerol) was deposited on the probe tip and then ≈1 μL peptide/matrix solution with a matrix-to-analyte molar ratio of 400:1 was added to the liquid matrix. Solutions for the H/D exchange reactions were prepared by dried droplet using 2',5'-dihydroxybenzoic acid as well as 2', 4', 6'-trihydroxyacetophenone monohydrate as matrix and D(-)fructose as a matrix additive with a matrix:additive:analyte molar ratio of 1000:500:1. D(-)fructose has been previously been observed to reduce the internal energies of the ions resulting in enhanced ionization and less fragmentation[94] and it was for this reason that D(-)fructose was added to the MALDI sample preparation for the H/D exchange ion-molecule reactions presented in this chapter.

Results

The ATDs of various analogs of bradykinin were studied by IM-MS. The ATDs of bradykinin (Figure 31C) and bradykinin fragments 1-8 (RPPGFSPF) (Figure 31A), 2-9 (PPGFSPFR) (Figure 31B), 2-7 (PPGFSP) (Figure 30A), and 5-9 (FSPFR) (Figure 30B) are dominated by a single peak. However, multiple peak features were observed in the ATD of bradykinin fragments 1-5 (RPPGF), 1-6 (RPPGFS) (Figure 26B), and 1-7 (RPPSFSP) (Figure 26C). A decrease in the resolution between the peaks is observed as

the fragment series progresses from 1-5 to 1-7 (see Figure 26). Three distinct ATDs are observed for the $[M+H]^+$ ions of BK1-5 (Figure 51A).

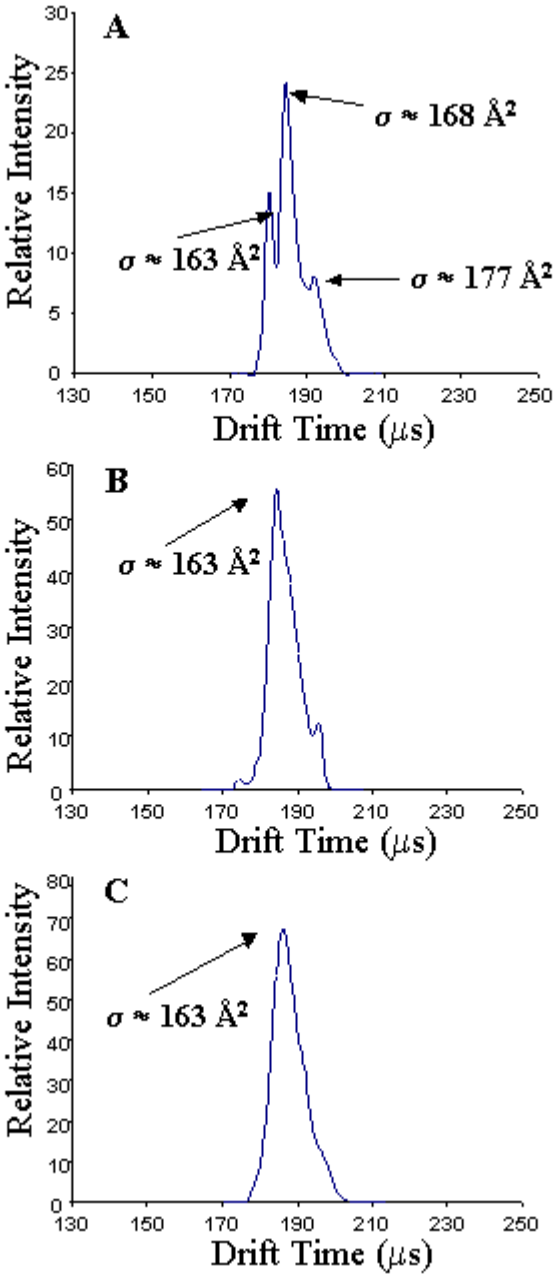

Figure 51. Arrival time distributions of bradykinin fragment 1-5 $[M+H]^+$ ions generated from MALDI samples prepared in solvents consisting of A) ≈90% H_2O and ≈1-% methanol (V/V), B) 25% H_2O and 75% methanol (V/V), and C) 100% methanol.

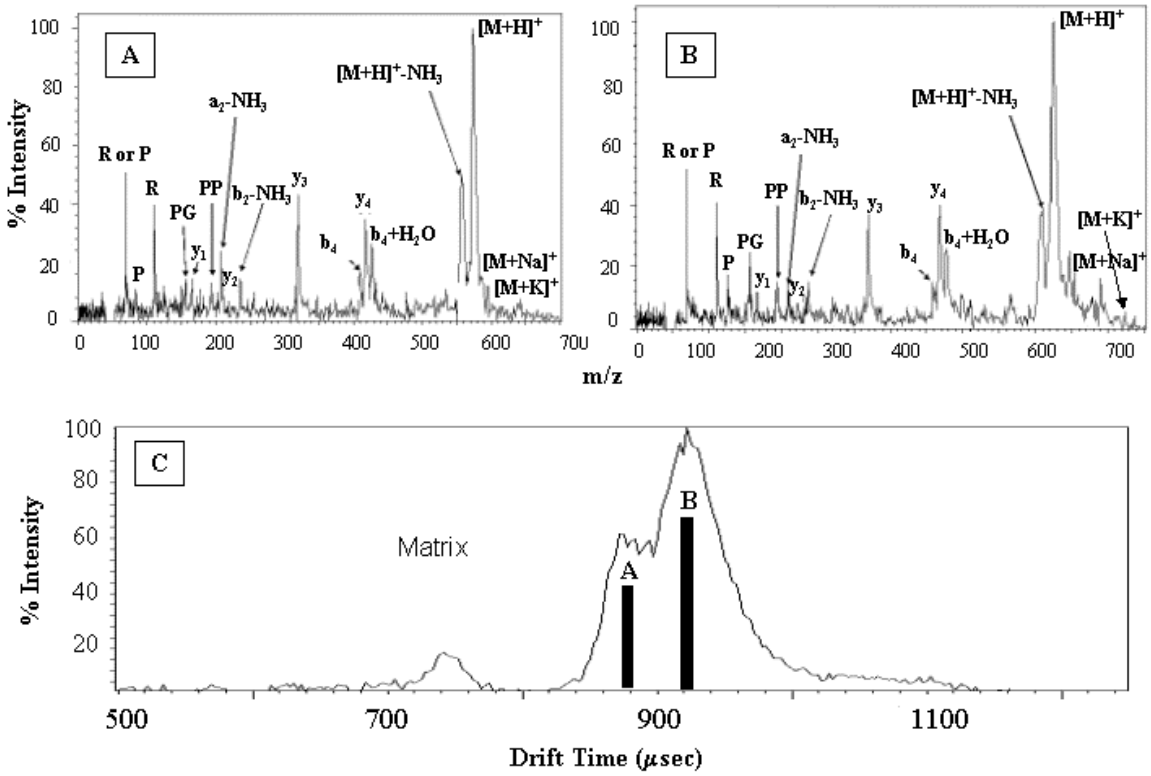

Figure 52. Data from ion mobility-surface induced dissociation of $[M+H]^+$ ions of bradykinin fragment 1-5 A) surface induced dissociation spectrum of ions found in time slice A (see C), B) surface induced dissociation spectrum of ions found in time slice B (see C), and C) arrival time distribution of bradykinin fragment 1-5 as observed in the ion mobility-surface induced dissociation experiment. The time slices of ions that were collided on the surface to produce the spectra (see A and B) are shown with dark lines and labeled A and B.[113]

IM-SID-TOF-MS spectra of BK1-5 $[M+H]^+$ ions are contained in Figure 52.[113] Note that the SID spectra for the two major mobility peaks are identical, consistent with the peaks arising from two different conformers, or populations of conformers, of the $[M+H]^+$ ions. For example, the relative abundance of the signal for fragments ions (b_i and y_j) are very similar in both spectra, and the signals formed by neutral loss (loss of NH_3 and loss of the C-terminal phenylalanine [$b_4 + H_2O$]) are almost identical. The same can be said about the immonium ions and internal cleavage (PP and PG fragment ions) product ions.

We also examined the effect of solvent composition on the ATD of BK1-5 $[M+H]^+$ ions. For example, MALDI sample deposits were prepared from 100% methanol, 75/25% methanol/water (Figure 51B), 50/50% methanol/water, 25/75% methanol/water, and ≈10/90% methanol/water compositions. From 100% methanol, the ATD of BK1-5 shows a single maxima (see Figure 51C) with a cross-section of 163 ± 4 $Å^2$, identical to that of the smaller cross section in the mobility plot shown in Figure 51A. Evidence of multiple conformations (*i.e.*, broad peaks, shoulders or multiple peaks)[109] consistently begin to appear as solvent composition was changed from 100% methanol to 75% methanol, demonstrating that more aqueous conditions favor the larger cross-section conformer (168 ± 5 $Å^2$). The mobility peak profile changes dramatically at ≈10/90% methanol/water, and at 10/90% methanol/water the more abundant conformer has the larger collision cross-section (168 ± 5 $Å^2$). Note also a small shoulder on the ATD, corresponding to a cross-section of 177 ± 3 $Å^2$.

The ATDs of BK1-5 $[M+H]^+$ ions and BK2-7 $[M+H]^+$ ions were deconvoluted using a gaussian curve-fit equation with Origin graphing software (OriginLab Corporation). While a single gaussian curve accurately (R^2 = 0.998, Chi^2 = 5.49) fits the ATD of BK2-7 $[M+H]^+$ ions (Figure 33A), the ATDs of BK1-5 $[M+H]^+$ ions generated from MALDI samples prepared in 100% methanol, 75% methanol and 90% water are best fit with multiple gaussian curves. For example, the ATD of BK1-5 $[M+H]^+$ ions generated from MALDI samples prepared in 100% methanol is best described by 2 gaussian curves (R^2 = 0.997, Chi^2 = 1.89). It was determined that the ATDs of BK1-5 $[M+H]^+$ ions generated from MALDI samples containing both 75% methanol and 90%

water are best fit with three gaussian curves (R^2 = 0.999, Chi^2 = 0.48 and R^2 = 0.997, Chi^2 = 0.24, respectively). The best fits of the ATDs of BK1-5 $[M+H]^+$ ions generated from MALDI samples prepared in 100% methanol, 75% methanol and 90% water are shown in Figures 53C, B, and A, respectively. Furthermore, the collision cross-sections calculated according to the fits of the ATDs correspond, within error, to the calculated collision cross-sections of the three conformers of BK1-5 $[M+H]^+$ ions (163, 168 and 177 $Å^2$). For example, the collision cross-sections, as calculated by the fit peak maxima, are 162 and 166 $Å^2$ for $[M+H]^+$ ions generated from MALDI samples prepared in 100% methanol. For $[M+H]^+$ ions generated from MALDI samples prepared in 75% methanol, the cross-sections of the fitted peaks are calculated as 161, 164, and 171 $Å^2$. The calculated cross-sections for the fitted peaks of the ATD for $[M+H]^+$ ions generated from MALDI samples prepared in 90% water are 163, 168, and 175 $Å^2$.

IM-MS of BK1-5 $[M+H]^+$ ions generated from liquid matrices were also examined in order to probe the effect of desorption from dried droplet versus desorption from liquid on the ATD (*i.e.*, gas-phase ion structure). ATDs of BK1-5 $[M+H]^+$ ions generated from 3-nitrobenzyl alcohol and methanol (Figure 54A) as well as from 3-nitrobenzyl alcohol, glycerol and methanol (Figure 54B) (see Experimental section) contained a single peak with calculated cross-sections (165 and 163 $Å^2$, respectively) similar to that for BK1-5 $[M+H]^+$ ions generated from dried droplet MALDI samples prepared from methanolic solvents (163 $Å^2$). ATDs of BK1-5 $[M+H]^+$ ions generated from glycerol with p-nitroaniline (Figure 54C) or α-cyano-4 hydroxycinnamic acid (Figure 54D) contained multiple peaks similar to that for BK1-5 $[M+H]^+$ ions generated

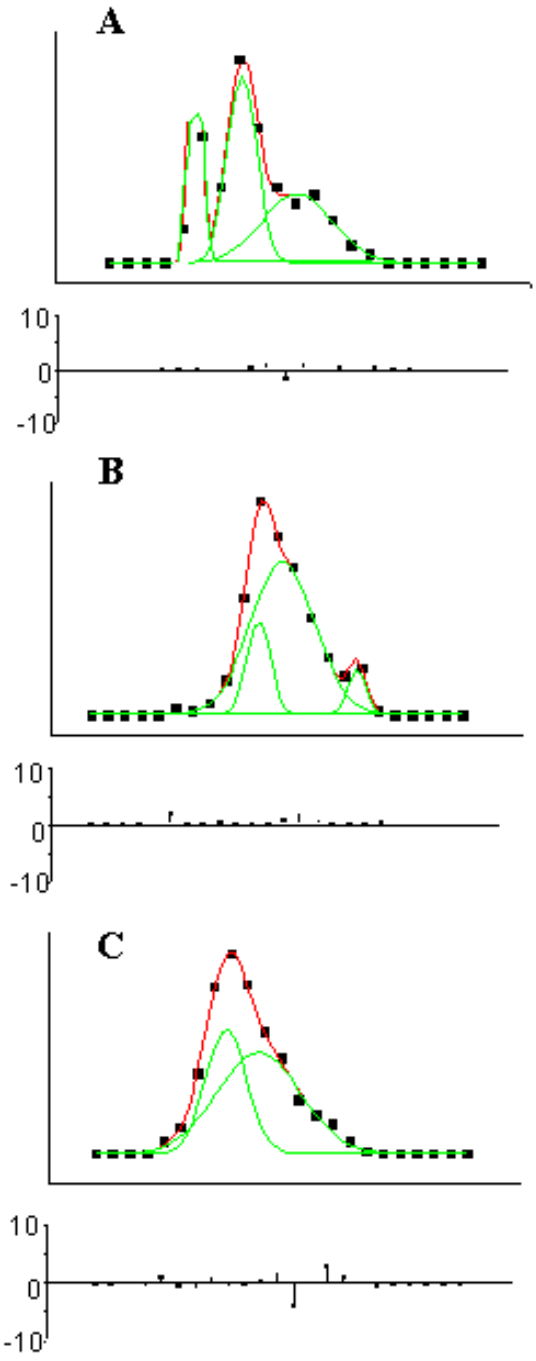

Figure 53. Fits and residuals of the arrival time distributions of bradykinin fragment 1-5 $[M+H]^+$ ions generated from MALDI samples prepared in solvents consisting of A) ≈90% H_2O and ≈10% methanol (V/V), B) 25% H_2O and 75% methanol (V/V), and C) 100% methanol.

from dried droplet MALDI samples prepared from solutions containing ≈90% water. The cross-sections of BK1-5 ions generated from glycerol with p-nitroaniline or α-cyano-4 hydroxycinnamic acid used as an additive (161, 167 and 173 $Å^2$) are very similar to those obtained from dried droplet MALDI samples prepared from solutions containing ≈90% water (163, 168 and 177 $Å^2$).

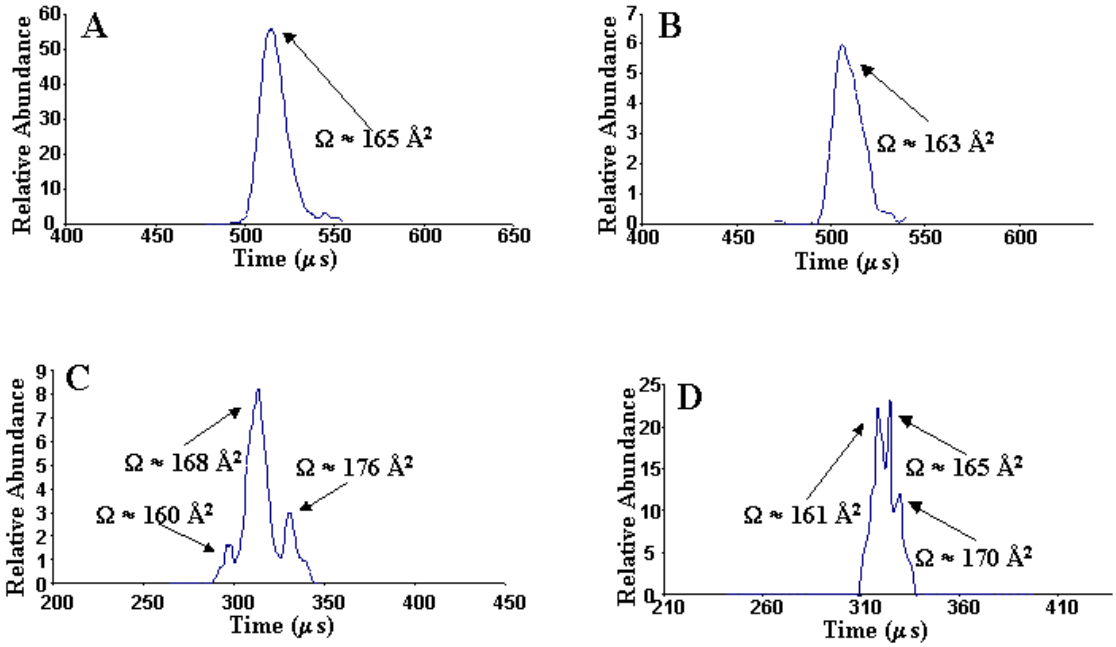

Figure 54. Arrival time distributions of bradykinin fragment 1-5 $[M+H]^+$ ions generated from liquid MALDI samples composed of A) 3-nitrobenzyl alcohol, B) 3-nitrobenzyl alcohol and glycerol, C) glycerol and p-nitroaniline, and D) glycerol and α-cyano-4-hydroxycinnamic acid.

H/D exchange reactions of BK1-5 $[M+H]^+$ ions with ND_3 and deuterated acetic acid (CD_3CO_2D) were also used as structural probes. The gas-phase basicity of ND_3 (204.0 kcal/mol) allows the H/D exchange ion-molecule reaction to occur at a faster rate than with CD_3CO_2D (190.2 kcal/mol), making ND_3 a useful reagent for measuring the

extent of H/D exchange.[44] However, ND_3 can participate in multiple exchanges per collision[44], therefore CD_3CO_2D was used to achieve greater selectivity for the H/D exchange reactions of multiple ion conformer populations. Discussion and interpretation of H/D exchange reaction kinetics is focused on the first exchange for reasons detailed in CHAPTER II. Figure 55A contains a temporal profile for H/D exchange with ND_3 of BK1-5 $[M+H]^+$ ions generated from aqueous containing solvent systems.

Rate constants for the first exchange of BK1-5 $[M+H]^+$ ions with ND_3 and CD_3CO_2D were obtained by plotting the natural log of the ion abundance as a function of reaction time at a constant pressure of H/D exchange reagent. These plots should generate a straight line, the slope of which can be used to calculate the rate of exchange. Curvature in the rate plot is probably due to multiple rates for H/D exchange. Rate measurements are presented for only the first exchange because we suspect that rearrangement reactions of the ion-molecule collision complex lead to a conformational change on the BK1-5 ion.[18] For approximately 90% of the ion population of BK1-5 $[M+H]^+$ ions generated from aqueous solvent systems the natural log plot is linear (see Figure 56A); however, as the ion population is depleted to approximately 10% of the total ion abundance, the slope of the natural log plot changes. Furthermore, a plot of $[M+H]^+$ ion (m/z 573) abundance vs. time using CD_3CO_2D (see Figure 56B) also displays curvature in which approximately 70% of the total ion abundance is composed of a fast-exchanging conformer, and the remaining 30% is composed of a slow-exchanging conformer. The decay of m/z 573 was fit using both a bi-exponential and a

single exponential decay equation (see Figures 57A and B, respectively). A bi-exponential decay (R = 0.998) better describes the rate of decay of m/z 573 than does a single exponential decay (R = 0.947), which we interpret to indicate that two rates of exchange.

H/D exchange reactions of BK1-5 $[M+H]^+$ ions from aqueous solvents were also performed in the analyzer cell of the ICR instrument. In order to obtain sufficient amounts of ions in the analyzer cell, a quadrupolar axialization event was performed prior to transfer from the source cell to the analyzer cell. Complete exchange of the $[M+H]^+$ ion of BK1-5 was achieved within 7 seconds when exchanged with deuterated acetic acid (see the rate plot in Figure 58). This time is markedly faster than the time observed in the source cell where exchange of the $[M+H]^+$ ion is not complete at 240 seconds (see the rate plots in Figure 56A and B). Additionally, the slope of the rate plot of BK1-5 [M+H]+ ions that have undergone quadrupolar axialization shows some curvature at short reaction times (Figure 58).

Gas-phase H/D exchange reactions were also performed on BK1-5 $[M+H]^+$ ions prepared from solvent systems composed mainly of methanol. Figure 55B contains a temporal profile for H/D exchange with ND_3 of BK1-5 $[M+H]^+$ ions generated from methanolic solvent systems. The natural log plot of BK1-5 $[M+H]^+$ ions generated from MALDI sample solutions composed of mainly methanol yield a straight line (see Figure 56C). The disappearance of m/z 573 was fit using both a bi-exponential and single exponential decay (Figures 59A and B, respectively) and both fit the trend equally well (R = 0.994), therefore a single exponential fit was accepted. Additionally, the slope of

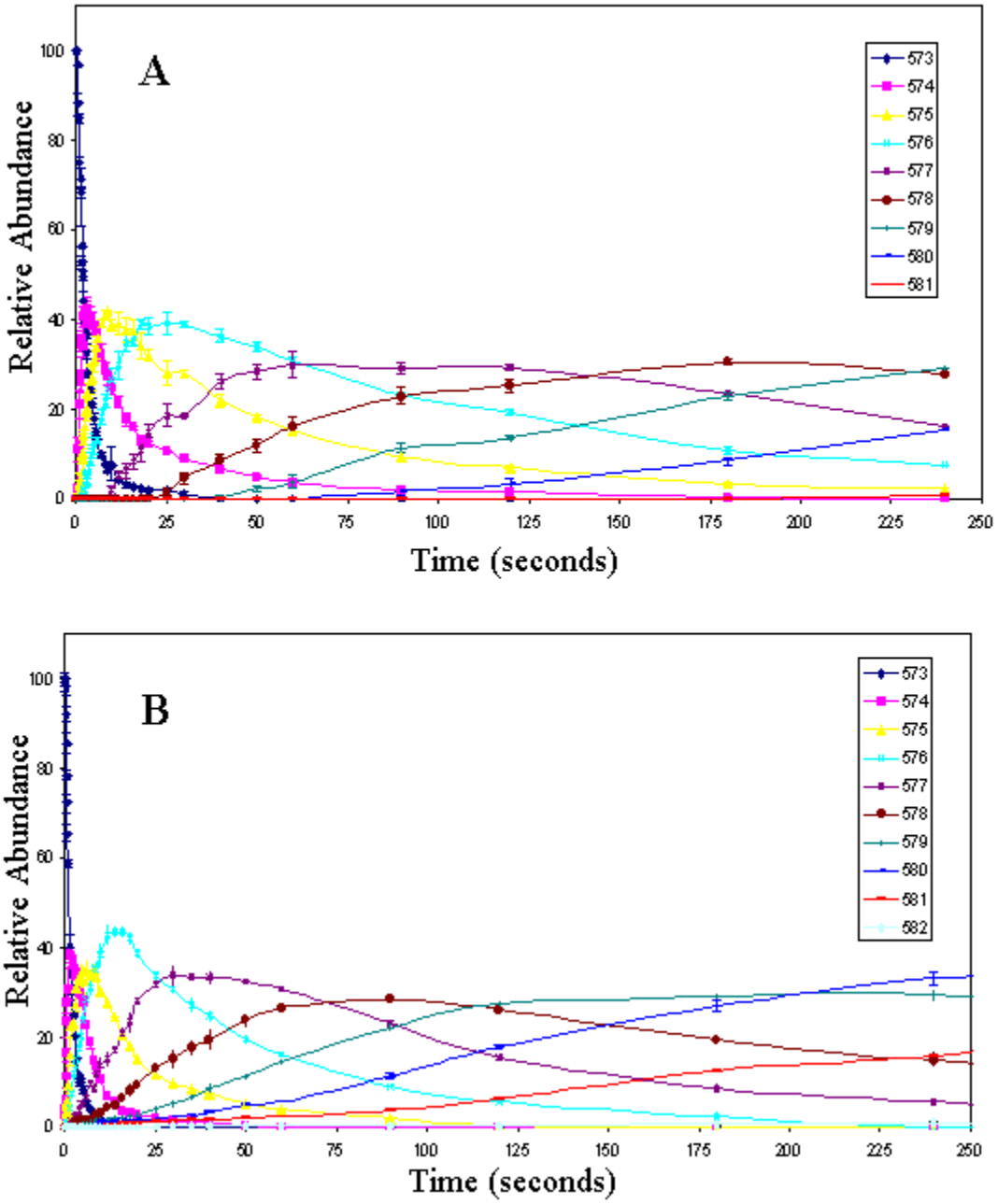

Figure 55. Temporal plot of the H/D exchange ion-molecule reactions of ND_3 with bradykinin fragment 1-5 $[M+H]^+$ ions A) generated from MALDI samples prepared in ≈80% H_2O and 20% methanol (V/V), and B) generated from MALDI samples prepared in 100% methanol.

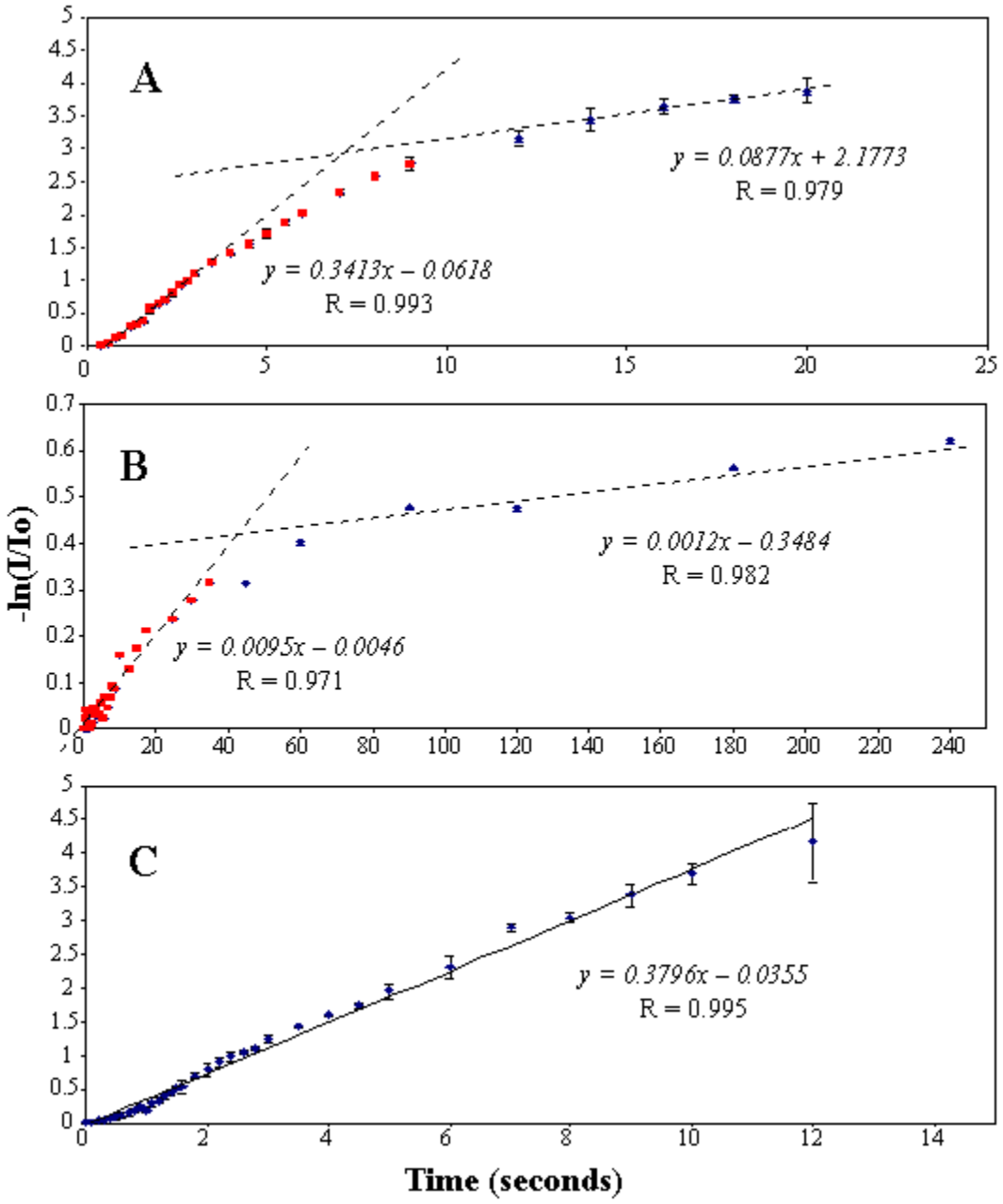

Figure 56. Rate plots for the first exchange in the H/D exchange ion-molecule reaction A) bradykinin fragment 1-5 $[M+H]^+$ ions generated from MALDI samples prepared in ≈80% H_2O and 20% methanol (V/V) with ND_3, B) bradykinin fragment 1-5 $[M+H]^+$ ions generated from MALDI samples prepared in ≈80% H_2O and 20% methanol (V/V) with CD_3CO_2D, and C) bradykinin fragment 1-5 $[M+H]^+$ ions generated from MALDI samples prepared in 100% methanol with ND_3.

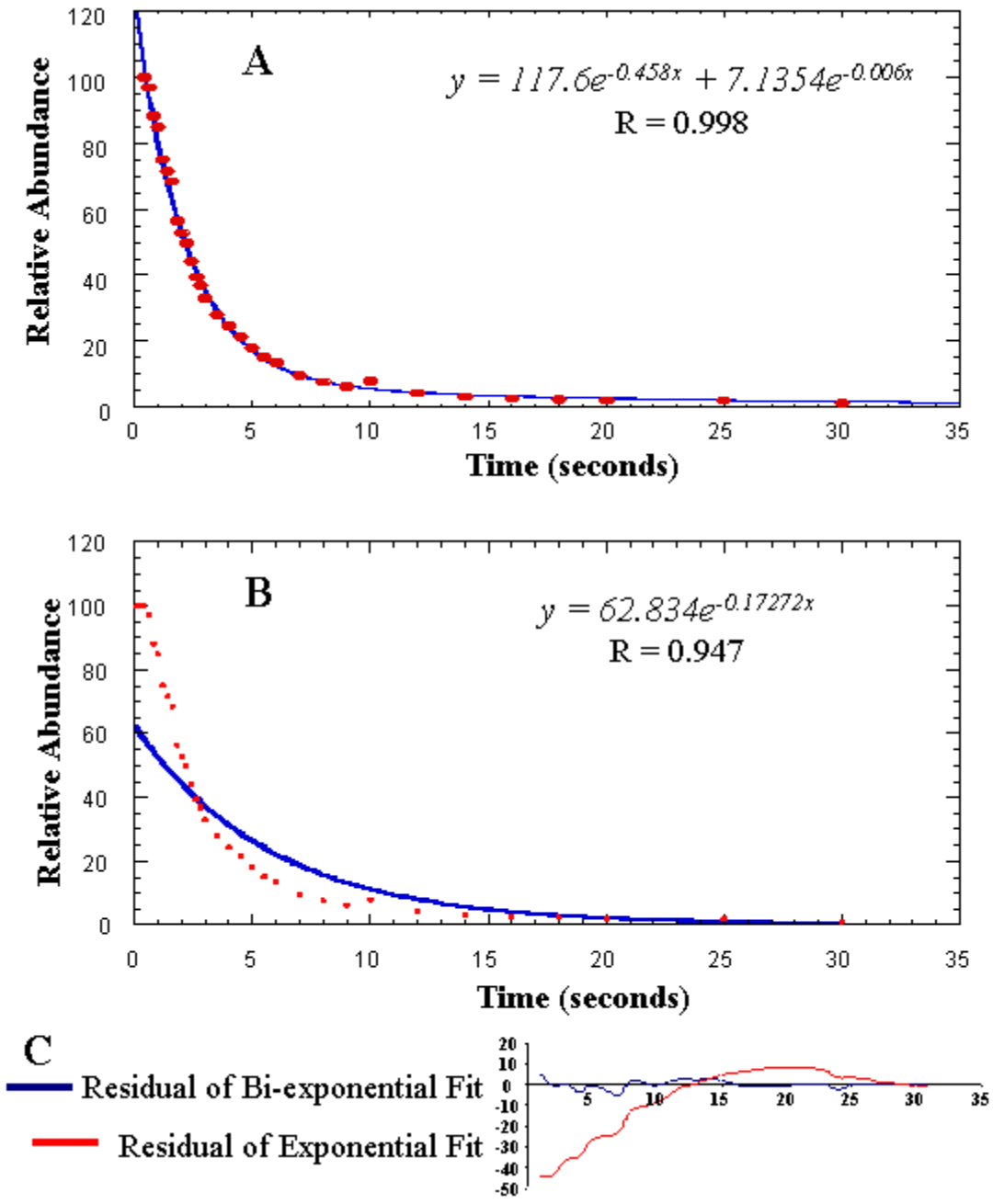

Figure 57. Fits and residuals of the decay of the first exchange of bradykinin fragment 1-5 $[M+H]^+$ ions generated from MALDI samples prepared in ≈80% H_2O and 20% methanol (V/V) with ND_3 A) bi-exponential fit, B) single exponential fit, and C) the residuals of the fits.

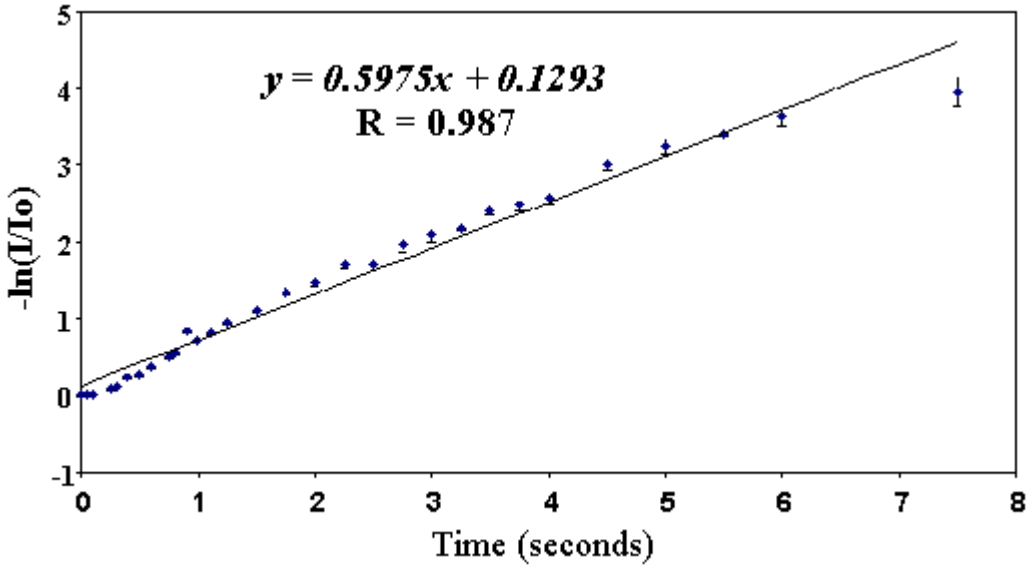

Figure 58. Rate plot for the first exchange in the H/D exchange ion-molecule reaction of bradykinin fragment 1-5 $[M+H]^+$ ions generated from MALDI samples prepared in ≈80% H_2O and 20% methanol (V/V) with ND_3 after a quadrupolar axialization event.

the natural log plot of BK 1-5 $[M+H]^+$ ions generated from methanolic MALDI solvents (Figure 56C) is very similar to the slope of the natural log plot of 90% of the ion population of BK1-5 from aqueous solvents (Figure 56A).

Bradykinin fragment 2-7 was also investigated with H/D exchange. The temporal plot of bradykinin fragment 2-7 (see Figure 60A) is very different from the two of BK1-5 from aqueous and methanolic solvent systems. The natural log plot of bradykinin fragment 2-7 yields a reasonably straight line (R = 0.951) (Figure 60B). A fit of the disappearance of m/z 601 of bradykinin fragment 2-7 was performed using Kaliedagraph®. As seen in Figure 61, both a bi-exponential and a single exponential decay fit the data relatively well (R = 0.976 for both), therefore a single exponential fit was accepted.

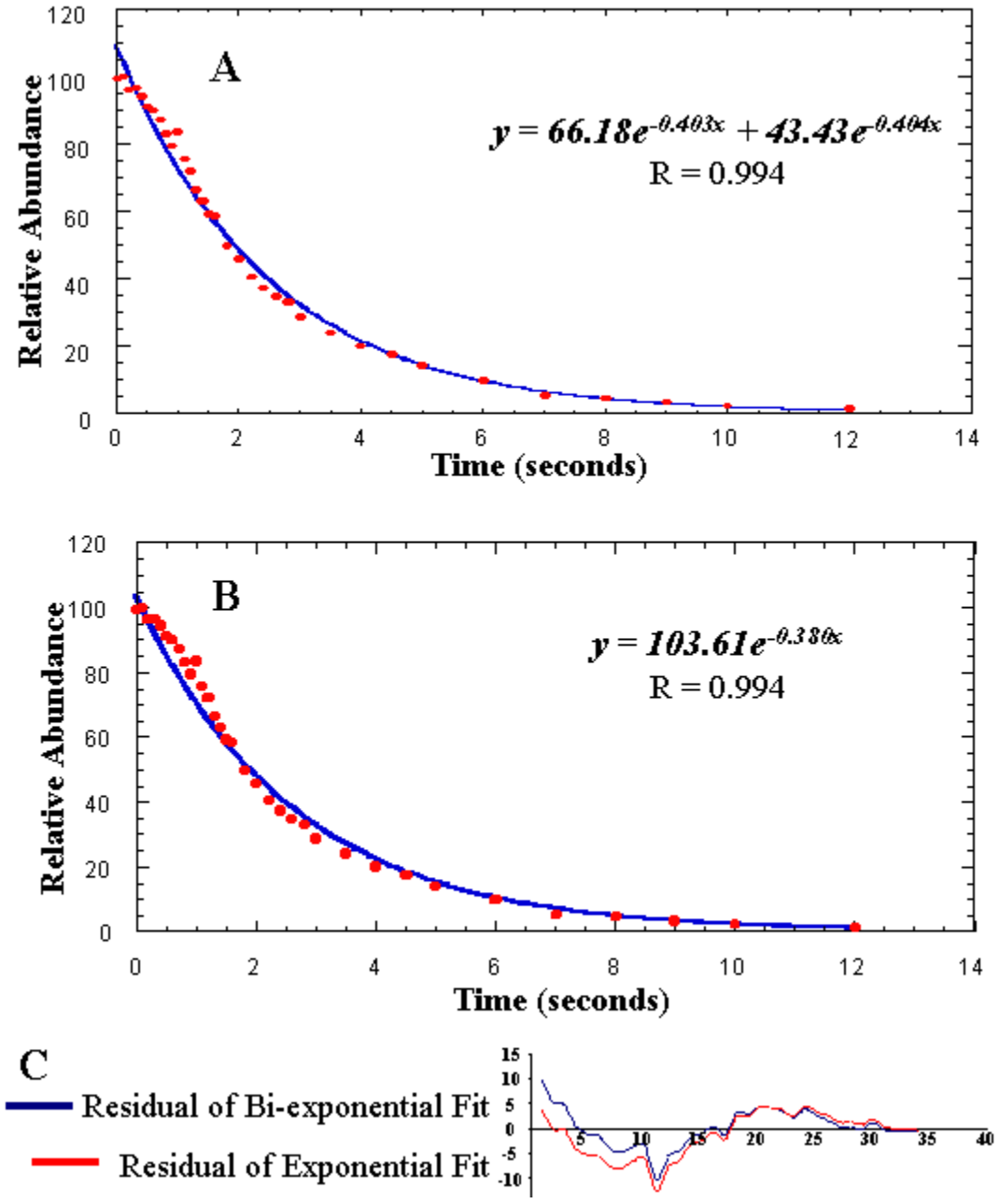

Figure 59. Fits and residuals of the decay of the first exchange of bradykinin fragment 1-5 $[M+H]^+$ ions generated from MALDI samples prepared in 100% methanol with ND_3 A) bi-exponential fit, B) single exponential fit, and C) residuals of the fits.

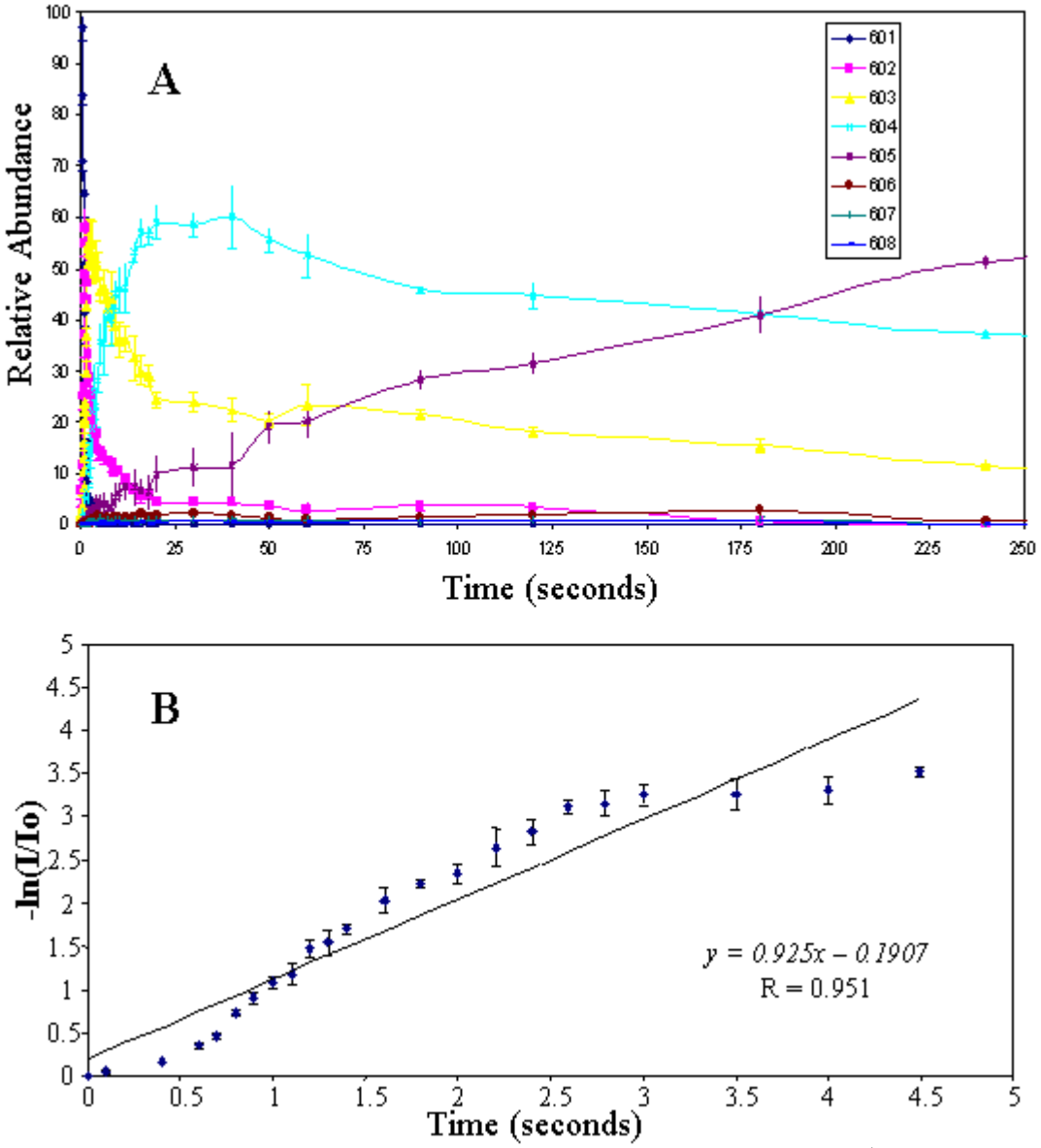

Figure 60. A) Temporal plot of the H/D exchange ion-molecule reaction of bradykinin fragment 2-7 $[M+H]^+$ ions with ND_3, and B) rate plot of the first exchange of bradykinin fragment 2-7 $[M+H]^+$ ions with ND_3.

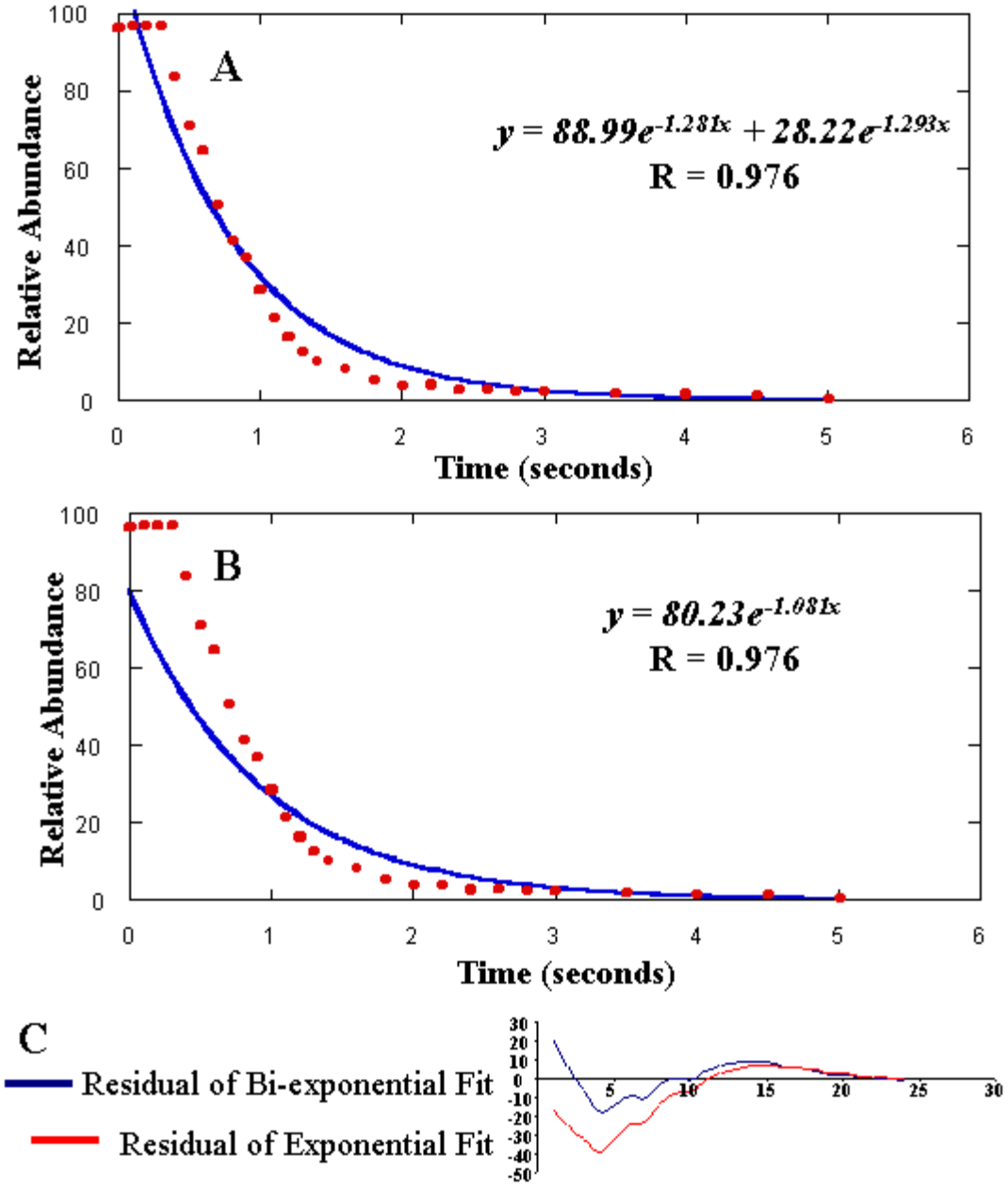

Figure 61. Fits and residuals of the decay of the first exchange of bradykinin 2-7 $[M+H]^+$ ions A) bi-exponential fit, B) single exponential fit, and C) residuals of the fits.

The dependence of the charge state distribution of BK1-5 as a function of solvent composition was investigated in order to further probe the changes in structure with changes in solvent. Singly charged BK1-5 ions are the most abundant species when the solvent system is composed of 100% methanol (see Figure 62E). However as water is stepwise added to the solvent system the doubly charged species is the most prevalent form (see Figures 62D-A). The ratio of $[M+H]^+$ ions to $[M+H]^{2+}$ ions rises as the percent of methanol in the solvent systems is increased (0.06, 0.17, 0.25, 0.37 and 1.3 for 0%, 25%, 50%, 75% and 100% methanol, respectively).

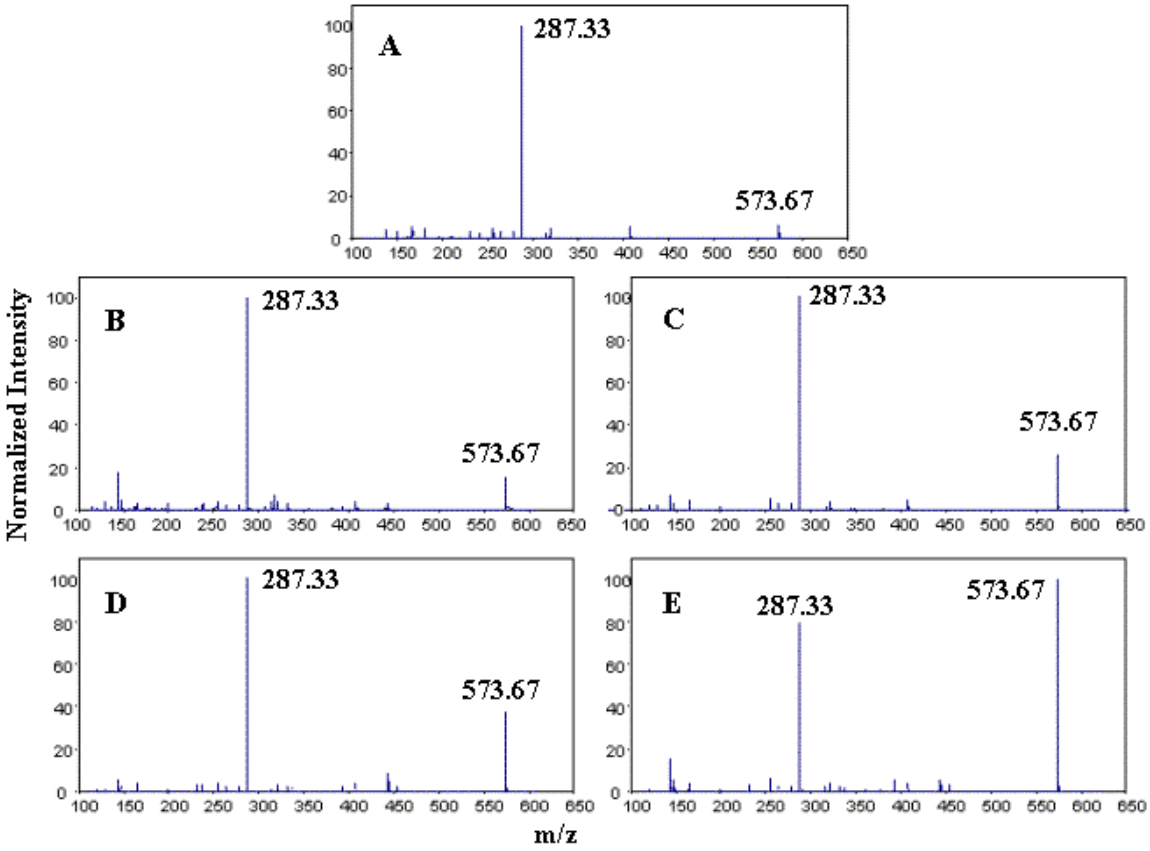

Figure 62. Electrospray ionization mass spectra of bradykinin fragment ions generated from A) 100% H_2O, B) 75% H_2O and 25% methanol (V/V), C) 50% H_2O and 50% methanol (V/V), D) 25% H_2O and 75% methanol (V/V), and E) 100% methanol.

CD experiments were performed in an effort to more specifically probe the secondary structure of BK1-5 in aqueous and methanolic solvent systems. The CD spectra were similar to one of a peptide that has a random coil structure and showed no change as water was stepwise added to the solvent system (Figure 63).

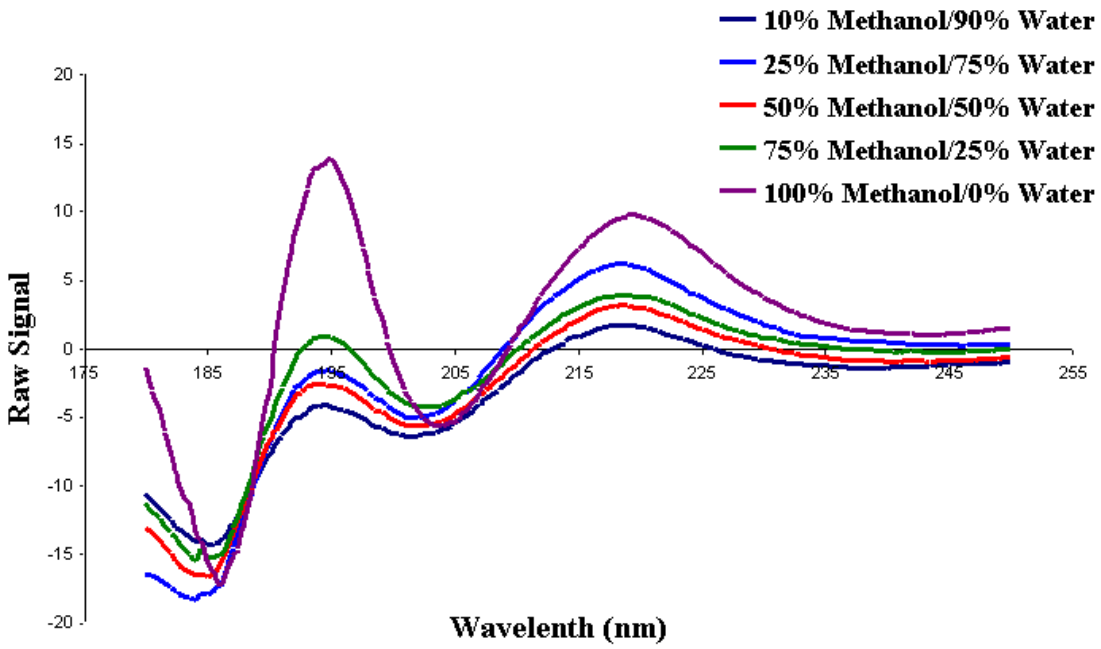

Figure 63. Circular dichroism spectra of bradykinin fragment 1-5 in solvent systems composed of 10% methanol and 90% H_2O (V/V) (dark blue), 25% methanol and 75% H_2O (V/V) (light blue), 50% methanol and 50% H_2O (V/V) (red), 75% methanol and 25% H_2O (V/V) (green), and 100% methanol (purple).

Molecular modeling, AM1 and density functional theory (DFT) energy calculations and filtering techniques were used to generate and select possible conformations for BK1-5 $[M+H]^+$ ions. Shown in Figure 64 are the cluster plots for BK1-5. Each group in the figures represents a structural group with different intra-

molecular interactions. Figure 64A clearly illustrates that both group 1 and group 2 are the most populated groups in the cross-section range of interest for the BK1-5 conformer with a cross-section of 163 $Å^2$ (represented by the first mobility peak in aqueous solvents). By comparing structures from these groups with IM-MS and H/D exchange data, a representative structure from group 1 was chosen. For the second peak in aqueous solutions (168 $Å^2$) group 2 was the most populated group in the cross-section range of interest while group 3 was the most populated group in the cross-section range for ions comprising the third mobility peak.

The lowest energy conformer of the most populated cluster that matches the 163 ± 5 $Å^2$ collision cross-section for BK1-5 is shown in Figure 65. In this conformation, the protonated guanidine group of arginine interacts with the C-terminus, the carbonyl oxygens along the peptide backbone are also interacting with the protonated arginine side chain, and the proline residues at positions 2 and 3 are in *cis* form, which allows the first carbonyl oxygen and the third amide bond to participate in a hydrogen bonding interaction, resulting in a β-turn. This conformation forms a tight ring, having a calculated (trajectory method) cross-section of 163 $Å^2$.

The proposed conformation for ions eluting under the second peak is one having fewer as well as different intra-molecular interactions. For example, the structure shown in Figure 66 is protonated on the guanidine group of the N-terminal arginine and the charge site interacts with the side chain of phenylalanine, and carbonyl oxygens. The proline residues found in the second and third positions of the peptide are in *trans* form,

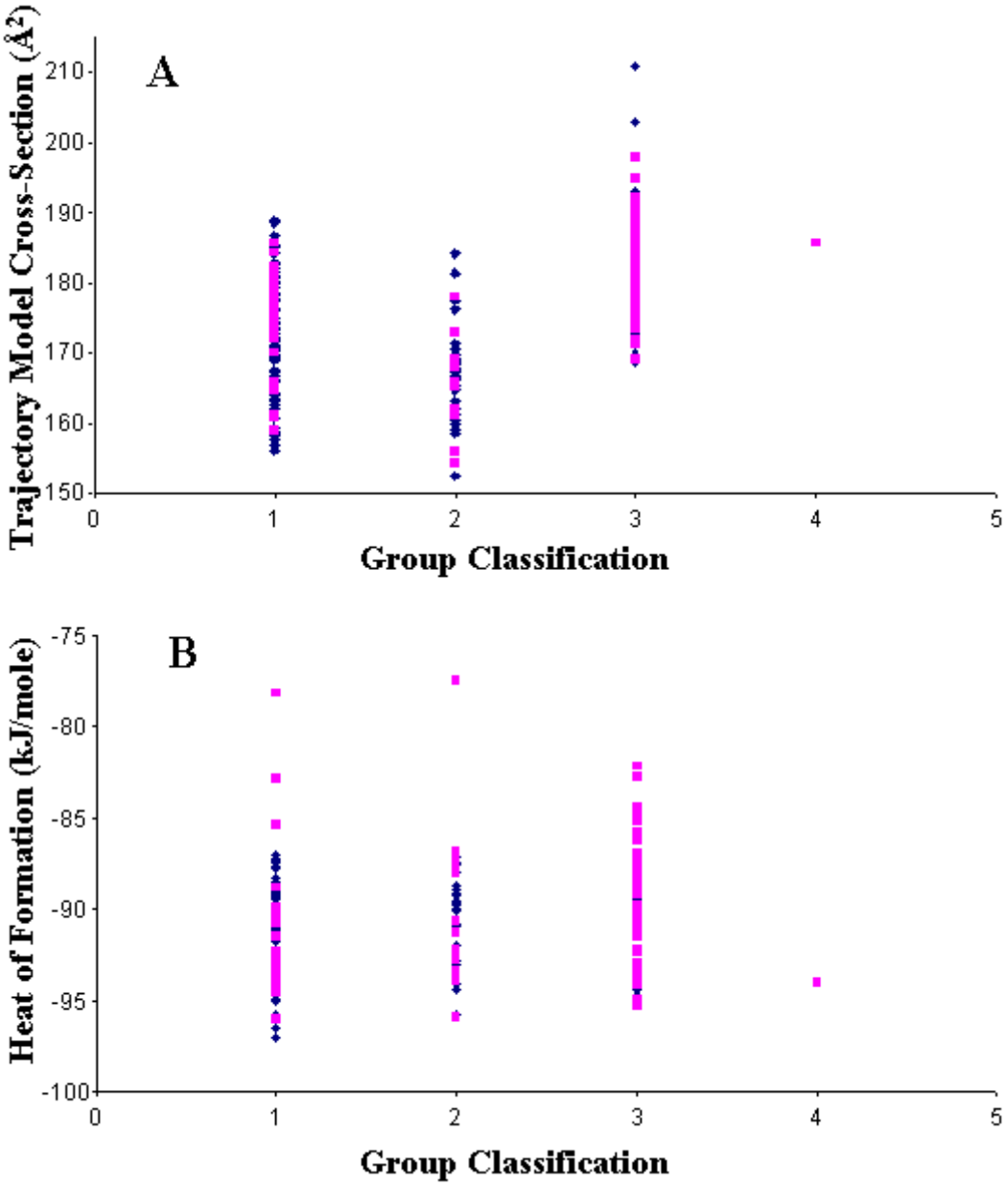

Figure 64. Cluster plots of structures of bradykinin fragment 1-5 $[M+H]^+$ ions A) cluster plot of the group classification and cross-section parameters, and B) cluster plot of the group classification and energy parameters.

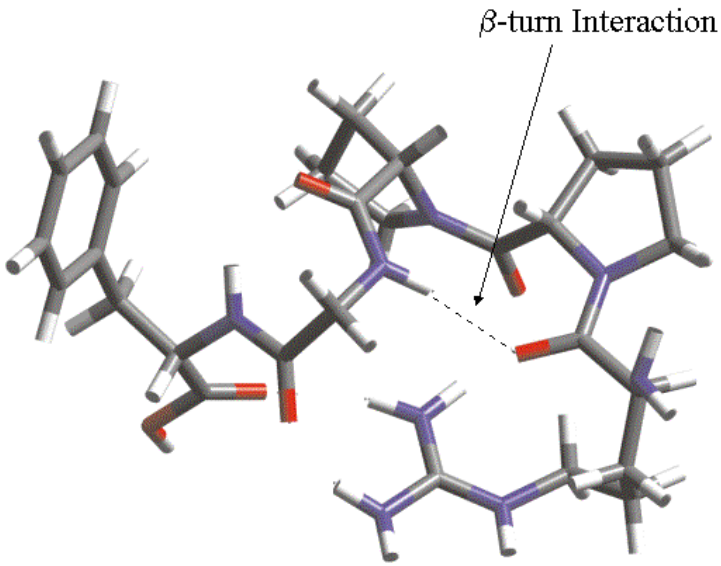

Figure 65. Proposed structure for the most compact conformation of bradykinin fragment 1-5 $[M+H]^+$ ions having a calculated cross-section of 163Å^2.

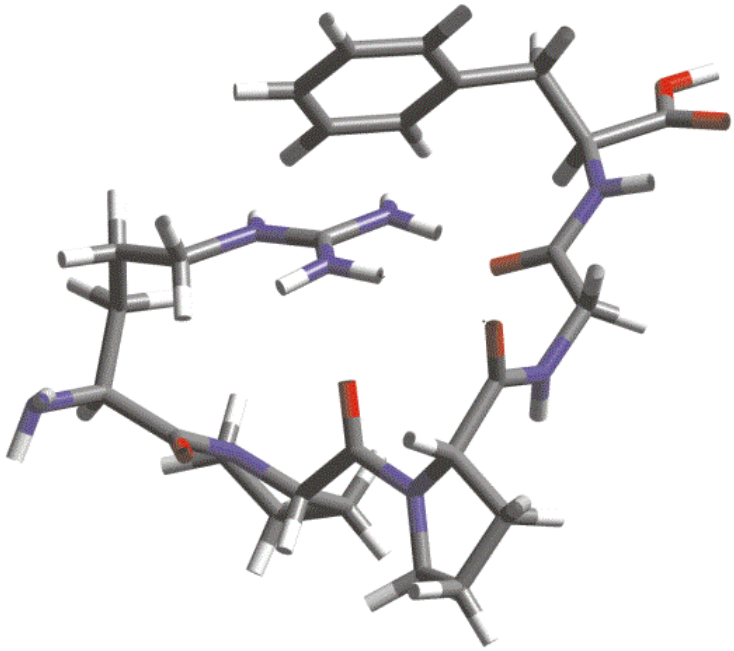

Figure 66. Proposed structure for the conformation of bradykinin fragment 1-5 $[M+H]^+$ ions having a calculated cross-section of 168Å^2.

and no β-turn is present. This structure has a calculated (trajectory method) cross-section of 168 $Å^2$.

A structure was also found that matched the cross-section for the ATD shoulder of the second peak of the BK1-5 mobility profile seen in the ≈10/90% methanol/water conditions, and is shown in Figure 67. This structure is more extended and the protonated side chain of arginine interacts with the first, second and third carbonyl oxygens along the peptide backbone, with little or no interactions observed in the rest of the molecule.

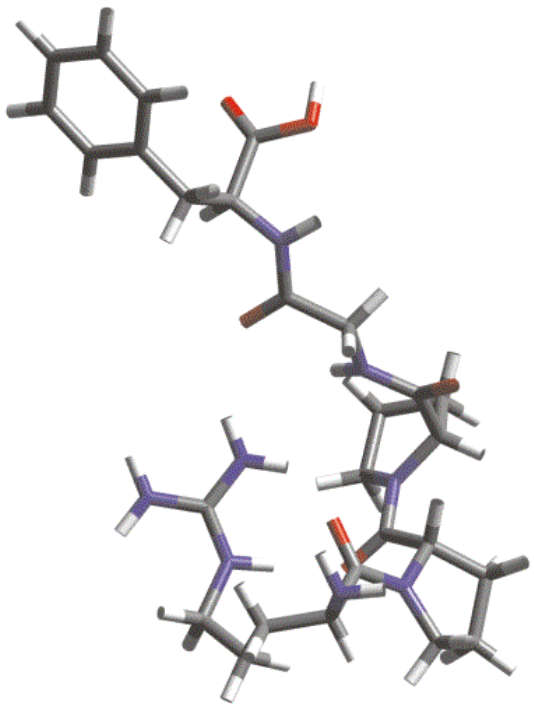

Figure 67. Proposed structure for the most extended conformation of bradykinin fragment 1-5 $[M+H]^+$ ions having a calculated cross-section of 177$Å^2$.

As with the proposed model for the second peak, the proline residues found in the second and third positions of the peptide are in *trans* form, and no β-turn is present. The calculated (trajectory method) cross-section of this conformation is 177 $Å^2$.

Discussion

The presence of multiple ATDs for bradykinin fragments 1-5, 1-6, and 1-7 are interpreted to indicate the presence of multiple non-interconverting conformers. This is consistent with a previous IM-MS study by Counterman *et al.*, in which observation of multiple peak features in the arrival time distribution of 42% of proline containing tryptic peptides of 10 or fewer residues was attributed to the presence of both the *cis* and *trans* isomer forms of proline resulting in structures having different collision cross-sections.[109] Additionally the observed decrease in the resolution between the peaks as the fragment series progresses from 1-5 to 1-7 is interpreted to suggest that the barrier to interconversion between the conformers is lowered as the fragment length is increased, accounting for the appearance of a broad unresolved peak for $[M+H]^+$ ions of bradykinin fragment 1-8 and bradykinin. These results are consistent with data from previous ion mobility experiments that suggest that bradykinin exists as multiple conformations with similar collision cross-sections.[31]

IM-MS experiments of BK1-5 $[M+H]^+$ ions desorbed from MALDI samples with different concentrations of methanol are interpreted to indicate the presence of a compact conformer when MALDI samples are prepared from organic (methanolic) solvent systems. However, when the MALDI samples are prepared from high amounts of water (90%) emergence of more extended conformations is observed, which I believe

suggests that the gas-phase conformation of BK1-5 $[M+H]^+$ ions retains some memory of the solution-phase structure. These results are consistent with a previous study in which Russell and Figueroa examined the solution-phase H/D exchange of bradykinin as a function of its solvent system.[4] They observed that the isotopic peak distribution of bradykinin shifts to higher masses as D_2O is added to organic solvent systems and suggested that bradykinin $[M+H]^+$ ions have a more compact conformation in organic solvents than in aqueous solvents, making the peptide less accessible to the deuterated solvent, which reduces the efficiency of H/D exchange. As water is added the conformation becomes more extended allowing the deuterated solvent access to the peptide, resulting in greater amounts of H/D exchange.

The ATDs of BK1-5 $[M+H]^+$ ions generated from MALDI samples prepared in 100% methanol, 75% methanol and 90% water are best fit with multiple gaussian curves. It seems, therefore, that multiple conformers are present under all MALDI sample conditions, resulting in a broadening of the ATD relative to that of a single conformer (BK2-7 $[M+H]^+$ ions). However, the multiple conformers are only resolved from one another when MALDI samples are prepared in 90% H_2O. I interpret this to indicate that the barrier of interconversion between the different BK1-5 conformers is higher in aqueous solvents, allowing the conformers to be separated by IM-MS when MALDI samples are prepared under such conditions. Considering that BK1-5 $[M+H]^+$ ions contain 2 proline residues, this is consistent with previous data that show that the rate of interconversion between the *cis* and *trans* forms of proline is solvent dependent.[114, 115]

Although multiple peaks in the ATD of BK1-5 $[M + H]^+$ ions is attributed to the presence of multiple conformers of the $[M + H]^+$ ions, several other possibilities were also evaluated. For example, dissociation of higher-mass species (*i.e.*, matrix clusters of BK1-5 $[M + H]^+$ ions or multimers of BK1-5[116]) to the *m/z* 573 signal could lead to an appearance of multiple peaks in the ATD of BK1-5 $[M + H]^+$ ions.[116] However, the SID data are inconsistent with this explanation due to the similarity in the spectra (relative abundance and observed fragment ions) for both IM resolved species (Figure 52). If the ATD were composed of dissociation products of higher mass species, we would expect the relative fragment ion abundance to be different, because the relative energies required to fragment a multimer vs. a monomer are different.[113] Reactions with background gases, *i.e.*, residual H_2O, in the drift tube could potentially lead to the appearance of multiple peaks in the ATD of BK1-5 $[M + H]^+$ ions. However, the ATD of BK2-7 $[M + H]^+$ ions (which has 4 residues in common with BK1-5 $[M + H]^+$ ions) is a single narrow gaussian curve (Figures 30A and 33A). Owing to the sequence homology between BK2-7 and BK1-5, it seems unlikely that the reaction chemistry of these two ions would differ significantly from that of BK2-7 $[M + H]^+$ ions. Furthermore, the ATD of BK1-5 $[M + H]^+$ ions is composed of multiple peaks only when MALDI samples are prepared with aqueous solvents, which should not affect drift tube reaction chemistry or the fragment ion spectra.

Results of H/D exchange ion-molecule reactions of BK1-5 $[M+H]^+$ ions formed from MALDI sample solutions composed of mostly water demonstrate that exchange occurs by bi-exponential decay. The observation of two distinct decay rates of the H/D

exchange is interpreted as evidence of multiple (probably two) reactive structures of BK1-5 $[M+H]^+$ ions, which is consistent with IM-MS data. Additionally, curvature in the rate plots demonstrate a similar relative population of the two conformers to that observed in the IM-MS experiments. Results of H/D exchange ion-molecule reactions of BK1-5 $[M+H]^+$ ions formed from MALDI sample solutions composed of mostly methanol demonstrate that exchange occurs by a single exponential decay which we interpret to indicate the presence of only one reactive structure of BK1-5, which is, again, consistent with IM-MS data. Additionally, complete exchange is observed for BK1-5 $[M+H]^+$ ions formed from both mostly aqueous and methanolic MALDI sample conditions, which, according to the suggested mechanism for gas-phase H/D exchange, implies that all exchangeable sites interact with the charge site(s).[44]

The observed increase in H/D exchange reactivity of BK1-5 $[M+H]^+$ ions and the curvature in the rate plots at short reaction times when H/D exchange occurs in the analyzer cell is concluded to be due to the quadrupolar axialization event prior to transfer. Campbell *et al.* suggest that curvature in the slope at short delays indicates a vibrationally and translationally hot population[42], which can occur from heating that is reported to occur upon quadrupolar axialization by Marshall and McLafferty.[52, 53] Additionally the authors report that heating from quadrupolar axialization can lead to destruction of the intra-molecular interactions that contribute to the structure of the ion, which could account for the increase in H/D exchange reactivity.[52, 53]

The change in the charge state distribution of BK1-5 as a function of solvent composition was investigated in an effort to further validate a change in conformation

upon addition of water. It has been previously observed that dissimilar conformations of a protein/peptide may yield different charge state distributions in an ESI-MS spectrum due to a difference in the availability of ionizable basic sites between the conformations.[55, 56 62] Larger conformations may have a higher number of ionizable basics sites on the surface of the protein/peptide and therefore might yield a higher charge state distribution than would a smaller conformation in which the basic sites may be buried. In solvent systems composed of 100% methanol, singly charged BK1-5 ions are the most abundant species in the ESI mass spectrum, which I interpret to suggest that a more compact conformation is the prevalent form. However as water is stepwise added to the solvent system the doubly charged species is the most prevalent form; a more extended conformation is populated. The change in the charge state distribution of BK1-5 $[M+H]^+$ ions as a function of solvent demonstrates the same solution composition dependence of gas-phase conformation observed in the ion mobility and gas-phase H/D exchange experiments discussed earlier.

The proposed structure for the compact conformation found in organic solvents has a theoretical cross-section of 163 $Å^2$, making it consistent with the IM-MS results. As can be seen in Figure 65, the charge site is in close proximity to several less basic sties—which allows stabilization of the onium ion during the H/D exchange ion-molecule reaction allowing exchange to take place. The guanidine group is solvated by carbonyl oxygens, however it is still accessible to ND_3, allowing facile H/D exchange, making this conformer consistent with the results of the H/D exchange ion-molecule reactions.

This conformation is consistent with expectations for conformations generated from organic solutions because the hydrophilic sites are turned inward to interact with each other while the hydrophobic sites are exposed to interact with the organic solvent. Previous experiments have suggested that organic solvents promote increased amounts of intra-molecular interactions.[99, 100,] The prolyl-proline bond in the proposed structure for the compact conformer is in the *cis* form, allowing for a β-turn interaction to occur, which agrees with solution-phase data that suggests the *cis* form of the prolyl-proline bond is favored in organic solvents.[99, 115] Additionally, the presence of a β-turn interaction in bradykinin fragments 1-4 and 1-5 in organic solvent systems has been previously observed by CD and NMR[99, 102], with which the proposed structure is consistent. Furthermore, the charged guanidine group in the proposed structure for the compact conformation of BK1-5 ions (Figure 65) is participating in hydrogen bonds with the C-terminus. This agrees with CD data for BK1-5 that suggests that the N-terminal and C-terminal portion of the molecule are in close proximity.[102]

In the conformation proposed for the second mobility peak observed in aqueous solvent conditions (Figure 66), less hydrophilic groups are interacting with each other than in the structure proposed for the compact conformation. More hydrophilic groups are exposed on the surface of the molecule, while the hydrophobic sites are turned to the inside of the molecule, which is consistent with NMR experiments on bradykinin. This suggests that the major hydrogen bonding interactions present in aqueous solutions are those between the peptide and the solvent.[101] Additionally, the charged guanidine group in the proposed structure is interacting with the phenylalanine side chain while the

carboxy terminus does not appear to interact with that portion of the molecule, which corresponds with NMR data of bradykinin in aqueous solution where the authors suggested that the arginine side chain is in the strongly asymmetric environment of the phenylalanine aromatic ring.[103] Gas-phase collision-induced decomposition (CID) data are also interpreted to suggest that $Arg^{1}Pro^{2}$ are interacting with $Pro^{3}Gly^{4}Phe^{5}$ in such a way that it is believed that the interaction is occurring between Arg^{1} and Phe^{5} or Pro^{3} in both bradykinin and BK1-5.[105]

The prolyl-proline bond in this proposed structure is in the *trans* form, in agreement with solution-phase studies, which are interpreted to indicate that this is the predominant form in aqueous solvents.[101, 115] The charge site in this more extended conformation is in close proximity the phenylalanine side chain as well as carbonyl oxygens, resulting in strong solvation of the basic site. According to the gas-phase H/D exchange mechanism, this would slow down the rate and decrease the extent of H/D exchange. This proposed structure is in agreement with the gas-phase IM-MS and H/D exchange data presented in this paper as well as with extensive solution-phase CD and NMR data on bradykinin.

Very little interactions are occurring in the structure proposed for the most extended conformation found in aqueous solutions, detected as a shoulder in the mobility profile from ≈10/90% methanol/water solvent conditions. As shown in Figure 67, the prolyl-proline bond is in the *trans* form, again, in agreement with solution-phase studies.[101, 115] The protonated arginine side chain is interacting with the first, second and fourth carbonyl oxygens while the majority of the molecule does not participate in

any hydrogen bonding interactions. The lack of extensive intra-molecular interactions in this structure corresponds to solution-phase CD data of bradykinin, from which it was concluded that no significant intra-molecular hydrogen bonding exists in the *trans* form of the peptide.[117] Along with the other proposed structures, the proposed structure corresponding to the most extended conformer is in agreement with the gas-phase experimental data presented in this paper as well as with CD and NMR data on bradykinin.

Conclusions

IM-MS, gas-phase H/D exchange and MM were successfully used to probe the intra-molecular interactions present as well as the effects of peptide/solvent interactions on gas-phase structure of bradykinin and its analogues. It was observed by IM-MS experiments that bradykinin and bradykinin fragments 1-8, 2-7, and 2-9 show a single peak in their ATDs while bradykinin fragments 1-5, 1-6 and 1-7 had multiple features in their ATDs. However, the resolution between the peaks seen in the drift-time profiles decreased as the fragment series progressed from 1-5 to 1-7 while the FWHM remained the same, from which it was concluded that as the length of the fragment is increased the degree of interconversion between the different conformers also increases. This is consistent with previous ion mobility experiments in which the ATD of bradykinin shows a single peak that is broader than that expected for a single conformer.[31] It is possible that the intra-molecular interactions seen in the multiple conformations of BK1-5 might be conserved as the fragment is increased to bradykinin, resulting in broadening

of its ATD. These data demonstrate that the structure of a species can be studied by investigating the structure of its fragments.

IM-MS experiments on BK1-5 $[M+H]^+$ ions were interpreted to indicate that the number and cross-sections of conformers present was highly dependent on the amount of methanol present in the solutions used to prepared MALDI samples. It was observed by both IM and gas-phase H/D exchange that a more compact conformer was present in organic solution conditions while at least one, and perhaps two, extended conformers were present in aqueous conditions. Proposed structures generated from molecular modeling illustrate that the hydrophilic groups of the more compact conformer were turned inward to interact with each other while the more hydrophobic sites of the molecule were on the outside, able to interact with methanol when in solution. The prolyl-proline bond of the proposed structure for the more compact conformer was in the *cis* form, allowing a β-turn interaction to occur. These results agree with solution-phase CD and NMR data taken from organic solvent systems. Proposed structures for the more extended conformers, generated from MALDI samples prepared in aqueous solutions, participated in less intra-molecular interactions than the more compact conformer and more hydrophilic groups were on the surface, allowing for possible interaction with the solvent when in solution. The prolyl-proline bond in these conformations was in the *trans* form, again in agreement with CD and NMR data. Correlation between the solution-phase CD and NMR data of bradykinin and it analogs, the gas-phase IM-MS and H/D exchange data and the MM data presented in this chapter is interpreted to indicate that the gas-phase conformation of BK1-5 $[M+H]^+$ ions is

dependent on the solvent composition of the MALDI sample and that the gas-phase conformations may reflect those found in the solution-phase.

Gas-phase and solution-phase data demonstrate that the peptidyl-proline and prolyl-proline bonds in bradykinin and its fragments are both important in determining secondary structure as well as dependent on the solvent conditions. This is also the case for other systems, such as RNase A. In native RNase A, Pro^{93} is the *cis* form and participates in a β-turn, however, upon isomerization to the *trans* form, the β-turn interaction is disrupted.[114] With further study, it is possible that *cis-trans* isomerization could be used to probe secondary structure. As ion-mobility seems particularly sensitive to *cis-trans* proline interactions, it might be possible to monitor changes in local structure with this technique that might be undetectable with other solution-phase techniques, such as CD or NMR.

CHAPTER VII

CONCLUSIONS

It is evident from the preceding chapters that ion mobility-mass spectrometry (IM-MS), gas-phase hydrogen/deuterium (H/D) exchange ion molecule reactions and molecular modeling provide complimentary information for the characterization of peptide ion structure, including fine structure detail (*i.e.*, cation-π interactions, β-turns, and charge solvation interactions). Experimental and computational results presented in this dissertation are discussed in terms of peptide ion structure, specifically the intra-molecular interactions present and how those interactions change upon alkali salt adduction (*i.e.*, Na^+, K^+ and Cs^+), as well as with the sequence of the peptide. Additionally, the effect of solvent on gas-phase peptide ion structure, *i.e.*, solution-phase memory effects, is discussed and gas-phase structures are compared to know solution-phase structures.

Effect of Sequence on Gas-Phase Peptide Ion Structure

It was observed by IM-MS that the conformation of a model tripeptide is highly dependent on the position of the tyrosine moiety (C-terminal or N-terminal). Proposed structures that correlate to experimental data were interpreted to suggest that structures that have extensive cation-π interactions are more compact than structures where the alkali ion is coordinated to oxygen-containing functionalities. Data was also interpreted to indicate that the position of the π-system (tyrosine moiety) significantly affects the presence of cation-π interactions and consequently, the structure of the peptide ion. Considering, these results it seems that the presence of the tyrosine moiety on the N-

terminus prohibits cation-π interactions in the protonated as well as cationized forms whereas the presence of the tyrosine on the C-terminus promotes cation-π interactions between an amide nitrogen in the protonated species as well as between the cations in the sodiated, potassiated and cesiated forms.

Additionally, gas-phase H/D ion-molecule reaction experiments were explained in terms of the presence of a cation as the charge site resulting in a lowering of the acidity of the other labile hydrogens in the molecule thereby lowering the rate and extent of H/D exchange. Therefore, exchange might not be indicative of conformational changes but more indicative of a change in the nature of the charge site.

Overall, results presented in Chapter IV were interpreted to indicate that the cation-π interaction can be a dominant non-covalent force that highly contributes to gas-phase peptide ion conformation, and is a force that can be competitive with traditional intramolecular interactions (*i.e.*, hydrogen bonding, van der Waals interactions and hydrophobic forces). The presence of cation-π interactions also seems to be highly dependent on the primary structure of the peptides, particularly on the position of the π-system.

Effect of Alkali Salt Adduction on Gas-Phase Peptide Ion Structure

It was observed by IM-MS experiments that the collision cross-sections of the alkali metal ion adducted (Na^+, K^+ and Cs^+) species of bradykinin and bradykinin fragments 1-5, 1-6, 1-7, 1-8, 2-7, 5-9 and 2-9 are very close to those of the protonated species, resulting in a deviation from the expected linear relationship. Additionally, multiple peak features observed in the ATDs of protonated bradykinin fragments 1-5, 1-

6 and 1-7 are conserved upon alkali metal ion adduction, which is interpreted to indicate that the structures do not significantly change.

Data from gas-phase hydrogen/deuterium (H/D) ion-molecule reactions show that alkali adducted species exchange slower and to a lesser extent than protonated species in arginine-containing peptides. Behavior similar to this has been previously observed for peptides and other biomolecules[97, 98] and was explained in terms of alkali adduction resulting in lack of a mobile proton as well as making the remaining hydrogens less acidic and therefore, less labile. Accordingly, the H/D exchange behavior of the bradykinin fragments and their alkali adducts might reflect only a change in the nature of the charge site and not changes in conformation. However, bradykinin fragment 2-7 had similar rates and extents of H/D exchange for the protonated and alkali metal ion adducted species. It is possible that, due to the lack of a strongly basic site (arginine), H/D exchange might take place at a site different from the charge site and the nature of this site would not change upon alkali metal ion adduction resulting in similar rates and extents of H/D exchange for the protonated and cationized species of bradykinin fragment 2-7.

Molecular modeling were used to further probe the fine structure detail of these molecules in order to understand the cause for deviations from the tend-line in the IM-MS experiments. From proposed structures it was concluded that the structure does not significantly change upon alkali metal ion adduction, in agreement with IM-MS data. Alkali metal ions bind in pockets in the peptide structure, resulting in little to no increase in the collision cross-section, or in some cases, a reduction in the collision cross-section

due to increased binding within the pocket, reducing its size. Furthermore, the charge site interactions are conserved within each species. Conservation of intramolecular interactions and general conformation accounts for deviations from the expected trend-line in IM-MS upon alkali metal ion adduction.

Effect of Solvent on Gas-Phase Peptide Ion Structure

The effects of solvent conditions used to prepare MALDI samples on the gas-phase conformations of bradykinin fragment 1-5 (**BK1-5**) $[M+H]^+$ ions was investigated using IM-MS, gas-phase H/D exchange ion-molecule reactions, molecular modeling as well as additional experimental techniques (*i.e.,* circular dichroism and charge state distribution analysis). IM-MS experiments were interpreted to indicate that the number and cross-sections of conformers present was highly dependent on the amount of methanol present in the original MALDI solution conditions from which the ions were generated. It was observed by both IM-MS and gas-phase H/D exchange that a more compact conformer was generated from MALDI samples prepared in organic solution conditions while two extended conformers were generated from MALDI samples prepared in aqueous conditions. Proposed structures from molecular modeling show that the hydrophilic groups of the more compact conformer were turned inward to interact with each other while the more hydrophobic sites of the molecule were on the outside, able to interact with methanol when in solution. The prolyl-proline bond of the proposed structure for the more compact conformer was in the *cis* form, allowing a β-turn interaction to occur. These results agree with solution-phase CD and NMR data taken from organic solvent systems. Possible structures for the more extended conformers,

found in aqueous solution conditions, participated in less intra-molecular interactions than the more compact conformer and more hydrophilic groups were on the surface, allowing for possible interaction with the solvent when in solution. The prolyl-proline bond in these conformations was in the *trans* form, again in agreement with CD and NMR data. These results were interpreted indicate that some memory of the solution-phase structure is retained in the gas-phase.

Future Directions

IM-MS was been successfully used to probe the dependence of the presence of multiple ion conformers of a single species on MALDI sample preparation solvent conditions (see Chapter VI). However, the dependence on the abundance of the conformers upon temperature was not measured. It has previously been shown that ion mobility experiments run at low temperatures are able to separate out conformers of a species that previously appeared as a single peak in the ATD.[118] The FWHM of the ATD of bradykinin fragment 1-5 $[M+H]^+$ ions generated from MALDI samples prepared with 100% methanol suggests that the two most abundant conformers might be present but that the barrier to interconversion between the two is low when generated from 100% methanol. By lowering the temperature of the experiment, the barrier to interconversion would effectively be raised, possibly allowing separation of the two most abundant conformers to occur even when samples are prepared with high amounts of methanol. Therefore, IM measurements of the $[M+H]^+$ ions of bradykinin fragment 1-5 as a function of both MALDI solvent systems and temperature is a prospective

experiment that could potentially lead to further insight on the link between solution-phase and gas-phase structure.

Gas-phase H/D exchange ion molecule reactions have been extensively used as a probe for protein and peptide ion structure. Quadrupolar axialization is a technique that is often used in conjunction with H/D exchange experiments to increase ion signal, mass resolution, and ease of transfer to a second region of an ICR cell.[49, 50] However, Marshall and McLafferty report that quadrupolar axialization can lead to heating of the ions which may result in destruction of the intramolecular interactions that contribute to the structure of the ion.[52-54] While experiments have been performed that demonstrate the heating that might occur during a quadrupolar axialization event for benzene[119] and $W(CO)_6^+$[54], such experiments have not been performed for biomolecules. Therefore, experiments that determined the amount of energy, if any, that is deposited in biomolecules during a quadrupolar axialization event would be of considerable interest due to the high use of quadrupolar axialization events in conjunction with H/D exchange ion-molecule reactions used as structural probes.

REFERENCES

(1) Hood, B. L.; Veenstra, T. D.; Conrads, T. P. *Int. Cong. Ser.* **2004,** *1266*, 375-380.

(2) Norin, M.; Sunstrom, M. *TRENDS Biotechnol.* **2002,** *20*, 79-84.

(3) Wilm, M.; Shevchenko, A.; Houthaeve, T.; Breit, S.; Schweigerer, L.; Fotsis, T.; Mann, M. *Nature* **1996,** *379*, 466-469.

(4) Figueroa, I. D.; Russell, D. H. *J. Am. Soc. Mass Spectrom.* **1999,** *10*, 719-731.

(5) Gimon-Kinsel, M. E.; Barbacci, D. C.; Russell, D. H. *J. Mass Spectrom.* **1999,** *34*, 124-136.

(6) Schnier, P. D.; Price, W. D.; Jockusch, R. A.; Williams, E. R. *J. Am. Chem. Soc.* **1996,** *118*, 7178-7189.

(7) Tsaprailis, G.; Nair, H.; Somogyi, A.; Wysocki, V. H.; Shong, W.; Futrell, J. H.; Summerfield, S. G.; Gaskell, S. J. *J. Am. Chem. Soc.* **1999,** *121*, 5142-5154.

(8) Russell, D. H.; McGlohon, E. S.; Mallis, L. M. *Anal. Chem.* **1988,** *60*, 1818-1824.

(9) Shields, S. J.; Bluhm, B. K.; Russell, D. H. *J. Am. Soc. Mass Spectrom.* **2000,** *11*, 626-638.

(10) Ruotolo, B. T.; Verbeck, G. F. IV; Thomson, L. M.; Woods, A. S.; Gillig, K. J.; Russell, D. H. *J. Proteom. Res.* **2002,** *1*, 303-306.

(11) Annan, R. S.; Carr, S. A. *J. Protein Chem.* **1997,** *16*, 391-402.

(12) Champion, M. M.; Campbell, C. S.; Siegele, D. A.; Russell, D. H.; Hu, J. C. *Mol. Microbiol.* **2003,** *47*, 383-396.

(13) Heck, A. J. R.; van den Heuvel, R. H. H. *Mass Spectrom. Rev.* **2004,** *23,* 368-389.

(14) Wang, F.; Freitas, M. A.; Marshall, A. G.; Sykes, B. D. *Int. J. Mass Spectrom.* **1999,** *192,* 319-325.

(15) Gross, D. S.; Zhao, Y.; Williams, E. R. *J. Am. Soc. Mass Spectrom.* **1997,** *8,* 519-524.

(16) Jurchen, J. C.; Williams, E. R. *J. Am. Chem. Soc.* **2003,** *125,* 2817-2826.

(17) Jockusch, R. A.; Lemoff, A. S.; Williams, E. R. *J. Am. Chem. Soc.* **2001,** *123,* 12255-12265.

(18) Jockusch, R. A.; Lemoff, A. S.; Williams, E. R. *J. Phys. Chem. A* **2001,** *105,* 10929-10942.

(19) Kohtani, M.; Jarrold, M. F. *J. Am. Chem. Soc.* **2002,** *124,* 11148-11158.

(20) Crowe, M. C.; Brodbelt, J. S. *J. Am. Soc. Mass Spectrom.* **2003,** *14,* 1148-1157.

(21) Ewing, N. P.; Pallante, G. A.; Zhang, X.; Cassady, C. J. *J. Mass Spectrom.* **2001,** *26,* 875-881.

(22) Ewing, N. P.; Zhan, X.; Cassady, C. J. *J. Mass Spectrom.* **1996,** *31,* 1345-1350.

(23) Hudgins, R. R.; Woenckhaus, J.; Jarrold, M. F. *Int. J. Mass Spectrom Ion Processes* **1997,** *165/166,* 497-507.

(24) Gill, A. C.; Jennings, K. R.; Wyttenbach, T.; Bowers, M. T. *Int. J. Mass Spectrom.* **2000,** *195/196,* 685-697.

(25) Counterman, A. E.; Valentine, S. J.; Srebalus, C. A.; Henderson, S. C.; Hoaglund, C. S.; Clemmer, D. E. *J. Am. Soc. Mass Spectrom.* **1998,** *9,* 743-759.

(26) Freitas, M. A.; Hendrickson, C. L.; Emmett, M. R.; Marshall, A. G. *Int. J. Mass Spectrom.* **1999,** *185-187*, 565-575.

(27) Freitas, M. A.; Marshall, A. G. *Int. J. Mass Spectrom.* **1999,** *182-183*, 22-231.

(28) Green, M. K.; Penn, S. G.; Lebrilla, C. B. *J. Am. Soc. Mass Spectrom.* **1995,** *6*, 1247-1251.

(29) Winger, B. E.; Light-Wahl, K. J.; Rockwood, A. L.; Smith, R. D. *J. Am. Chem. Soc.* **1992,** *114*, 5897-5898.

(30) Heck, A. J. R.; Jorgensen, T. J. D.; O'Sullivan, M.; von Raumer, M.; Derrick, P. J. *J. Am. Soc. Mass Spectrom.* **1998,** *9*, 1255-1266.

(31) Wyttenbach, T.; von Helden, G.; Bowers, M. T. *J. Am. Chem. Soc.* **1996,** *118*, 8355-8364.

(32) Hudgins, R. R.; Mao, Y.; Ratner, M. A.; Jarrold, M. F. *Biophys. J.* **1999,** *76*, 1591-1597.

(33) Kaleta, D. T.; Jarrold, M. F. *J. Phys. Chem. B* **2001,** *105*, 4436-4440.

(34) Wu, C.; Siems, W. F.; Klasmeier, J.; Hill, H. H. *Anal. Chem.* **2000,** *72*.

(35) Mason, E. A.; McDaniel, E. W. *Transport Properties of Ions in Gases*; John Wiley & Sons: New York, 1988.

(36) Liu, Y.; Valentine, S. J.; Counterman, A. E.; Hoaglund, C. S.; Clemmer, D. E. *Anal. Chem.* **1997,** *69*, 728A-735A.

(37) Ruotolo, B. T.; Gillig, K. J.; Stone, E. G.; Russell, D. H.; Fuhrer, K.; Gonin, M.; Schultz, J. A. *J. Mass Spectrom.* **2002,** *219*, 253-267.

(38) Gillig, K. J.; Ruotolo, B.; Stone, E. G.; Russell, D. H.; Fuhrer, K.; Gonin, M.; Schultz, A. J. *Anal. Chem.* **2000,** *72*, 3965-3971.

(39) Dunning, F. B.; Hulet, R. G. *Atom, Molecular, and Optical Physics: Charged Particles*; Academic Press: San Diego, 1995.

(40) Ruotolo, B. T.; Tate, C. C.; Russell, D. H. *J. Am. Soc. Mass Spectrom.* **2004,** *15*, 870-878.

(41) Stone, E. G.; Gillig, K. J.; Ruotolo, B. T.; Russell, D. H. *Int. J. Mass Spectrom.* **2001,** *212*, 519-533.

(42) Campbell, S.; Rodgers, M. T.; Marzluff, E. M.; Beauchamp, J. L. *J. Am. Chem. Soc.* **1995,** *117*, 12840-12854.

(43) Solouki, T.; Freitas, M. A.; Alomary, A. *Anal. Chem.* **1999,** *71*, 4719-4726.

(44) Campbell, S.; Rodgers, M. T.; Marzluff, E. M.; Beauchamp, J. L. *J. Am. Chem. Soc.* **1994,** *116*, 9765-9766.

(45) Wyttenbach, T.; Bowers, M. T. *J. Am. Soc. Mass Spectrom.* **1999,** *10*, 9-14.

(46) Cox, H. A.; Julian, R. R.; Lee, S.; Beauchamp, J. L. *J. Am. Chem. Soc.* **2004,** *126*, 6485-6490.

(47) Wyttenbach, T.; Paizs, B.; Barran, P.; Breci, L.; Liu, D.; Suhai, S.; Wysocki, V. H.; Bowers, M. T. *J. Am. Chem. Soc.* **2003,** *125*, 13768-13775.

(48) Marini, J. T., *Development and Implementation of a FT-ICR Mass Spectrometer for the Investigation of Ion Conformations of Peptide Sequence Isomers Containing Basic Amino Acid Residues by Gas-Phase Hydrogen/Deuterium Exchange*, Dissertation, Texas A&M University, College Station, 2003.

(49) Amster, I. J. *J. Mass Spectrom.* **1996,** *31*, 1325-1337.

(50) Guan, S.; Kim, H. S.; Marshall, A. G. *Chem. Rev.* **1994,** *94*, 2161-2182.

(51) Marshall, A. G.; Hendrickson, C. L.; Jackson, G. S. *Mass Spectrom. Rev.* **1998,** *17*, 1-35.

(52) Freitas, M. A.; Hendrickson, C. L.; Emmett, M. R.; Marshall, A. G. *J. Am. Soc. Mass Spectrom.* **1998,** *9*, 1012-1019.

(53) O'Connor, P. B.; Speir, J. P.; Wood, T. D.; Chorush, R. A.; Guan, Z.; McLafferty, F. W. *J. Mass Spectrom.* **1996,** *31*, 555-559.

(54) Guan, S.; Reinhold, B. B.; Xin, T.; Marshall, A. G. Orlando, FL, August 25-29 1996.

(55) Chowdhury, S. K.; Katta, V.; Chait, B. T. *J. Am. Chem. Soc.* **1990,** *112*, 9012-9013.

(56) Konermann, L.; Rosell, F. I.; Mauk, A. G.; Douglas, D. J. *Biochemistry* **1997,** *36*, 6448-6454.

(57) Iavarone, A. T.; Jurchen, J. C.; Williams, E. R. *J. Am. Soc. Mass Spectrom.* **2000,** *11*, 976-985.

(58) Le Blanc, J. C. Y.; Beuchemin, D.; Siu, K. W. M.; Guevremont, R.; Berman, S. S. *Org. Mass Spectrom.* **1991,** *26*, 831-839.

(59) Li, Y.; Cole, R. B. *Anal. Chem.* **2003,** *75*, 5739-5746.

(60) Konermann, L.; Douglas, D. J. *J. Am. Soc. Mass Spectrom.* **1998,** *9*, 1248-1254.

(61) Grandori, R. *J. Mass Spectrom.* **2003,** *38*, 11-15.

(62) Katta, V.; Chait, B. T. *J. Am. Chem. Soc.* **1991,** *113*, 8534-8535.

(63) Konermann, L.; Douglas, D. J. *Biochemistry* **1997,** *36*, 12296-12302.

(64) Babu, K. R.; Moradian, A.; Douglas, D. J. *J. Am. Soc. Mass Spectrom.* **2001,** *12*, 317-328.

(65) Babu, K. R.; Douglas, D. J. *Biochemistry* **2000,** *39*, 14702-14710.

(66) Konermann, L.; Rosell, F. I.; Mauk, A. G.; Douglas, D. J. *Biochemistry* **1997,** *36*, 6448-6454.

(67) Berova, N.; Nakanishi, K.; Woody, R. W. *Circular Dichroism: Principles and Applications*, 2 ed.; John Wiley & Sons, Inc.: New York, 2000.

(68) Gotts, N. G.; von Helden, G.; Bowers, M. T. *Int. J. Mass Spectrom. Ion Processes* **1995,** *149/150*, 217-229.

(69) Mesleh, M. F.; Hunter, J. M.; Shvartsburg, A. A.; Schatz, G. C.; Jarrold, M. F. *J. Phys. Chem.* **1996,** *100*, 16082-16086.

(70) Shvartsburg, A. A.; Jarrold, M. F. *Chem. Phys. Lett.* **1996,** *261*, 86-91.

(71) Taraszka, J. A.; Countermann, A. E.; Clemmer, D. E. *Int. J. Mass Spectrom.* **2001,** *204*, 87-100.

(72) Kirkpatrick, S.; Gelatt, C. D.; Vechhi, M. P. *Science* **1983,** *220*, 671-680.

(73) Wilson, S. R.; Cui, W. *Biopolymers* **1990,** *29*, 225-235.

(74) Accelrys, http://www.hhmi.swmed.edu/Manuals/insight2K/insight2K/ffbs/2_Forcefields.html (date accessed: September 17, 2004).

(75) Leach, A. R. *Molecular Modelling: Principles and Applications*, 2 ed.; Prentice Hall, 2001.

(76) Shotle, D.; Simons, K. T.; Baker, D. *Proc. Natl. Acad. Sci. USA* **1998,** *95*, 11158-11162.

(77) Troyer, J. M.; Cohen, F. E. *Proteins: Struct., Func., Genet.* **1995,** *23*, 97-110.

(78) Petersson, G. A.; Al-Laham, M. A. *J. Chem. Phys.* **1991,** *94*, 6081-6090.

(79) Petersson, G. A.; Bennett, A.; Tensfeldt, T. G.; Al-Laham, M. A.; Shirley, W. A.; Mantzaris, J. *J. Chem. Phys.* **1988,** *89*, 2193-2218.

(80) von Helden, G.; Hsu, M. T.; Gotts, N.; Bowers, M. T. *J. Phys. Chem.* **1993,** *97*, 8182-92.

(81) Burley, S. K.; Petsko, G. A. *FEBS Lett.* **1986,** *203*, 139-143.

(82) Dougherty, D. A. *Science* **1996,** *271*, 163-168.

(83) Mallis, L. M.; Russell, D. H. *Anal. Chem.* **1986,** *58*, 1076-1080.

(84) Grese, R. P. Cerny, R. L.; Gross, M. L. *J. Am. Chem. Soc.* **1989,** *111*, 2835-2842.

(85) Teesch, L. M.; Adams, J. *J. Am. Chem. Soc.* **1991,** *113*, 812-820.

(86) Teesch, L. M.; Adams, J. *J. Am. Chem. Soc.* **1990,** *112*, 4110-4120.

(87) Cerda, B. A.; Cornett, L.; Wesdemiotis, C. *Int. J. Mass Spectrom.* **1999,** *193*, 205-226.

(88) Ma, J. C.; Dougherty, D. A. *Chem. Rev.* **1997,** *97*, 1303-1324.

(89) Wyttenbach, T.; Witt, M.; Bowers, M. T. *J. Am. Chem. Soc.* **2000,** *122*, 3458-3464.

(90) Lee, S.; Wyttenbach, T.; Bowers, M. T. *Int. J. Mass Spectrom. Ion Processes* **1997,** *167/168*, 605-614.

(91) Matz, L. M.; Hill Jr., H. H. *Anal. Chem.* **2001,** *73*, 1664-1669.

(92) Wyttenbach, T.; von Helden, G.; Bowers, M. T. *Int. J. Mass Spectrom. Ion Processes* **1997,** *165/166*, 377-390.

(93) Heginbotham, L.; MacKinnon, R. *Neuron* **1992,** *8*, 483-491.

(94) Koster, C.; Castoro, J. A.; Wilkins, C. L. *J. Am. Chem. Soc.* **1992,** *114*, 7572-7574.

(95) Vollmer, D. L. G., Michael L. *J. Mass Spectrom.* **1995,** *30*, 113-118.

(96) Ustyuzhanin, P.; Kogan, A.; Reuben, B. G.; Lifshitz, C. *Int. J. Chem. Kinet.* **2001,** *33*, 707-714.

(97) Solouki, T.; Fort Jr., R.C.; Alomary, A.; Fattahi, A. *J. Am. Soc. Mass Spectrom.* **2001,** *12*, 1272-1285.

(98) Reyzer, M. L.; Brodbelt, J. S. *J. Am. Soc. Mass Spectrom.* **2000,** *11*, 711-721.

(99) Cann, J. R.; Liu, X; Stewart, J. M.; Gera, L.; Kotovych, G. *Biopolymers* **1994**, *34*, 869-878.

(100) Cann, J. R.; Stewart, J. M.; Matsueda, G. R. *Biochemistry* **1973**, *12*, 3780-3788.

(101) London, R. E.; Stewart, J. M; Cann, J. R.; Matwiyoff, N. A. *Biochemistry* **1978**, *17*, 2270-2277.

(102) Lintner, K.; Fermandjian, S.; Regoli, D. *Biochimie* **1979**, *61*, 87-92.

(103) Denys, L.; Bothner-By, A. A.; Fisher, G. H.; Ryan, J. W. *Biochemistry* **1982,** *21*, 6531-6536.

(104) Lee, S. C.; Russell, A. F.; Laidig, W. D. *Int. J. Pept. Protein Res.* **1990,** *35*, 367-377.

(105) Neumann, G. M.; Derrick, P. J. *Aust. J. Chem.* **1984,** *37*, 2261-77.

(106) Schaaf, T. G.; Stephenson, J. L.; McLuckey, S. A. *J. Am. Chem. Soc.* **1999,** *121*, 8907-8919.

(107) Ruotolo, B. T.; Verbeck, Guido F.; Thomson, L. M.; Gillig, K. J.; Russell, D. H. *J. Am. Chem. Soc.* **2002,** *124*, 4214-4215.

(108) Wang, J.; Cassady, C. J. *Int. J. Mass Spectrom.* **1999,** *182/183*, 233-41.

(109) Counterman, A. E.; Clemmer, D. E. *Anal. Chem.* **2002,** *74*, 1946-1951.

(110) Covey, T.; Douglas, D. J. *J. Am. Soc. Mass Spectrom.* **1993,** *4*, 616-623.

(111) Foresman, J. B.; Frisch, A. *Exploring Chemistry with Electronic Structure Methods: A Guide to Using Gaussian*, 2 ed.; Gaussian, Inc.: Pittsburg, PA, 1996.

(112) Williams, T. L.; Fenselau, C. *Eur. Mass Spectrom.* **1998,** *4*, 379-383.

(113 Stone, E. G., *Development of a MALDI-Ion Mobility-Surface-Induced Dissociation-Time-of-Flight Mass Spectrometer for the Analysis of Peptides and Proteins*, Dissertation, Texas A&M University, College Station, 2003.

(114) Wedemeyer, W. J.; Welker, E.; Scheraga, H. *Biochemistry* **2002,** *41*, 14637-14644.

(115) London, R. E. M., Nicholas A.; Stewart, J. M.; Cann, John R. *Biochemistry* **1978,** *17*, 2277-2283.

(116) Counterman, A. E.; Valentine, S. J.; Srebalus, C. A.; Henderson, H. C.; Hoaglund, C. S.; Clemmer, D. E. *J. Am. Soc. Mass Spectrom.* **1998**, 9, 643-759.

(117) Cann, J. R.; Stewart, J. M.; London, R. E.; Matwiyoff, N. *Biochemistry* **1976,** *15*, 498-504.

(118) Giddens, J.; Bowers, M. T. *J. Am. Soc. Mass Spectrom.* **2003,** *14*, 161-170.

(119) Gillig, K., *The Development of a Fourier Transform Ion Cyclotron Resonance Ion Mobility Spectrometer and Studies of Ion Motion in a Wire Ion Guide Cell*, Dissertation, Texas A&M University, College Station, 1997.

VITA

Holly Ann Sawyer was born in Houston, Texas and raised in Fairfield, California. Upon high school graduation, she attended Harding University in Searcy, Arkansas where she obtained a Baccalaureate in Science degree (Major subject: Biochemistry) Magna Cum Laude in May of 1999. In 1999 she began her graduate work in the Department of Chemistry at Texas A&M University under the guidance of Dr. David H. Russell. She earned her Ph.D. degree in December of 2004. Holly is an active member of the American Society of Mass Spectrometry and Phi Lambda Upsilon. Some selected presentations to date are:

52nd ASMS Conference on Mass Spectrometry, May 2004, Nashville, TN. "A Detailed Analysis of Gas-Phase Peptide Ions Containing N-terminal Arginine: Bradykinin Fragments 1-5, 1-6 and 1-7"

Industry University Cooperative Chemistry Program Symposium on General and Pharmaceutical Research in Chemistry, October 2003, College Station, TX. "Observation of Solution-Phase Memory Effects in Bradykinin Fragment 1-5: Evidence from Ion Mobility and H/D Exchange Mass Spectrometry"

50th ASMS Conference on Mass Spectrometry, June 2002, Orlando, FA. "Effect of Intra-Molecular Interactions on the Gas-Phase Conformation of Bradykinin as Probed by Ion Mobility-Mass Spectrometry"

7th International Symposium of the ABRF, March 2002, Austin, TX. "Cesium-Ion Adduction and Cooperative Binding Effects on Peptide Conformation as Probed by Ion Mobility-Mass Spectrometry"

Her permanent address is: 2950 Vista Grande, Fairfield, CA 94534.